Structural and Magnetic Properties of the Oxides AB_2O_6
(A^{2+} = Mn, Fe, Co, Ni, Cu; and B^{5+} = As or Sb)

By

Abdussalam Mohammed Nakua, B.Sc.

A Thesis
Submitted to the School of Graduate Studies
in Partial Fulfillment of the Requirements
for the degree
Doctor of Philosophy

McMaster University
1994

Structural and Magnetic Properties of the Oxides AB_2O_6
(A^{2+} = Mn, Fe, Co, Ni, Cu; and B^{5+} = As or Sb)

Doctor of Philosophy	(1994) McMaster University
(Chemistry)	Hamilton Ontario

Title: Structural and Magnetic Properties of the Oxides AB_2O_6 (A^{2+} = Mn, Fe, Co, Ni, Cu; and B^{5+} = As or Sb)
Author: Abdussalam Mohammed Nakua, B.Sc. (Laurentian University)
Supervisor: Professor J. Greedan
Number of Pages: xv, 181.

---

to

my parents and my wife

Abstract

The structural and magnetic properties of a number of transition metal oxides of the general formula AB_2O_6, where A is Mn, Fe, Co, Ni, and Cu, and B is Sb^{5+} or As^{5+}, have been investigated.

$CuSb_2O_6$ crystallizes in a monoclinically distorted trirutile structure in the space group *$P2_1/n$*. Magnetic susceptibility is characterized by a broad maximum at 60 K indicative of the presence of significant short range correlations in this system, and an abrupt decrease in the susceptibility suggesting the presence of a magnetically ordered state. Further analysis of the susceptibility provided that the magnetic correlations in this system are dominant along the chains; this is the first trirutile compound that gives the clearest evidence for 1-d magnetic correlations. Long range magnetic order was further studied by low temperature neutron diffraction. This reflection was indexed with a propagation vector $\boldsymbol{k} = (½, 0, ½)$ in accordance with some of the trirutile phases such as $CoSb_2O_6$ and $FeTa_2O_6$. The magnetic moment of Cu^{2+} was estimated at about 0.5 μ_B. The presence of long range order was further supported by the registration of the spin flop transition on a single crystal of $CuSb_2O_6$.

$CoAs_2O_6$, $NiAs_2O_6$, and $MnAs_2O_6$ are isostructural and adopt the lead antimonate structure and crystallize in the space group *P-31m*. Magnetic susceptibility data were characterized by the absence of short range correlations. The long range order in these materials was studied in detail using low temperature neutron diffraction.

For $NiAs_2O_6$ and $CoAs_2O_6$, a number of superlattice reflections appears in their respective low temperature neutron diffraction profiles which were indexed with the propagation vector $\boldsymbol{k} = (0, 0, ½)$. The profiles of both materials were refined using the Rietveld method in the space group *P-31m*. The refinement was handled by the Rietan program in which the refined magnetic moment of Ni^{2+} was found to be 2.11(1) μ_B, and for Co^{2+} was 2.66(30).

The low temperature neutron diffraction profile of $MnAs_2O_6$ was much more complicated than those of $NiAs_2O_6$ and $CoAs_2O_6$. An exhaustive list of propagation vectors were used in order to fit the pattern without much success.

Lastly, in preparing the iron member of this series, $Fe_2As_4O_{12}$ was obtained instead of the isostructural member of the lead antimonate structure which has a markedly different crystal structure. Although the crystal structure contains Fe_2O_9 dimers, the magnetic susceptibility did not fit the predictions of the S = 5/2 - 5/2 dimer model. This peculiarity is attributed to the details of the crystal structure. As for the magnetically ordered state, the superlattice reflections were indexed with the wavevector $\boldsymbol{k} = (0,0,0)$ and the Rietveld refinement was carried out in the space group *P3*.

Acknowledgement

I would like to thank my supervisor Dr. J. E. Greedan for his guidance, help, encouragement, and patience.

I am grateful to my supervisory committee, Dr. J. Barbier and Dr. B. Gaulin, for their insightful comments and useful suggestions. The assistance from the technical staff, J. Garret, B. Collier, F. Gibbs, K. Teeter, and H. and A. Dabkowski is greatly appreciated. Special thanks to A. Dabkowski for his help with the various furnaces and for giving me liberal access to his own.

I want to thank Dr. J. Reimers and Dr. S. Xue for their help early on when I got started. I would also like to thank Dr. G. Luo, Dr. R. Nandyala, Dr. H. Yun for their assistance. Many thanks to my friends in room ABB-443, E. Fok, R. Hammond, M. MacEachern, and G. Amow for their help and support, and for many useful and enlightening discussions about many diverse topics.

Many thanks to my parents and my wife for their continuous support and encouragement. The assistance of Mrs. Carol Dada at the department office in the time of need is greatly appreciated.

Table of Contents

List of Figures

List of Tables

Chapter 1

Introduction

Magnetochemistry, as it is practiced today, is a formidable research tool that provides chemical and physical information on systems being studied in many branches of science. It reveals information that promotes the understanding and control of the physical properties of materials. It will be clear from this introduction that chemistry plays a central role in this process. It offers us a great flexibility in the design of a magnetic lattice. For instance, we have the freedom to vary the dimensionality of the magnetic lattice, the type, and the range of the magnetic interactions, and the spin value of the magnetic moment.

Over the past 30 years, there have been many advances in the understanding of magnetic phenomena. Many research efforts are currently directed toward the understanding of the relationship between the observed magnetic properties of a material and its chemical and structural characteristics, *i.e.* the nature of its chemical constituents and the way in which these are bound together to form the crystal lattice. For example, numerous materials with strong magnetic correlations only along chains or in planes existing in particular crystal lattices have been synthesized and studied.

A large volume of published work on low dimensional magnetic materials does exist, some of this literature is reviewed in references (J74) (C86) (J92) (O93). Reference (J74) gives a comprehensive account of the work published on these magnetic systems prior to 1974. Reference (J92) is mainly concerned with the magnetic properties of the layered transition metal compounds. Reference (O93) introduces the interested reader to the currently active areas of the research in the field of magnetochemistry.

In the course of this work, we have investigated the structural and magnetic properties of oxides with the general formula AB_2O_6 where A is a divalent transition metal and B is either Sb^{5+} or As^{5+}. Among the transition metal antimonates, $CuSb_2O_6$ has been studied, while a series of transition metal arsenates has been investigated. The crystal structures of these transition metal arsenates have not been determined with reasonable accuracy to date, indeed research on these materials has been scanty. In this thesis we will study in detail the crystal and magnetic structures of copper antimonate and the arsenates of Ni, Co, Mn, and Fe.

This thesis is composed of seven chapters. In this chapter, the basic theory of magnetism in materials containing transition metal ions will be reviewed briefly while greater emphasis is given to systems exhibiting strong spin-spin exchange interactions. The different model systems of magnetic materials will be introduced along with a few illustrative examples. The theory of nuclear and magnetic neutron diffraction will be reviewed in chapter two, the principle of the Rietveld refinement method, which is responsible for much of the interest the powder diffraction technique has received in the past 25 years, will be discussed in some detail. The experimental procedures which were used in this study will be described in chapter three. The results of this work will be discussed in chapters four, five, and six, and in chapter seven, the conclusion of this investigation will be summarized.

I- Basic Theory of Magnetism:

The magnetic properties of transition metal ions arise from the ground state of the metal ion as well as those thermally populated states (C77.1). Thus, the contribution of a particular level to the magnetic properties may be altered by varying the temperature. Given the properties of an individual ion, we can calculate the properties of a mole of ions by a straight forward procedure, using the Boltzmann distribution (C77.1). The distribution of the magnetic ions among the various states is given by,

$$\frac{N_i}{N_j} \propto e^{-\Delta E_n/kT} \tag{1.1}$$

where ΔE_n is the energy level separation between levels *i* and *j*.

Now, the mean magnetic moment of an ion in the level *n* is given as $\mu_n = \partial E_n/\partial H$; the average magnetic moment, $<\mu>$, is therefore obtained as the sum over magnetic moments weighted according to the Boltzmann factor

$$\langle \mu \rangle = \frac{\sum_n \mu_n e^{-E_n/kT}}{\sum_n e^{-E_n/kT}} \tag{1.2}$$

and the bulk magnetization for a sample with N identical magnetic atoms per mole is

$$M = N_o \langle \mu \rangle \tag{1.3}$$

In order to investigate the interaction of the magnetic ions with the magnetic field, it is useful to expand the energy in powers of the field as in equation(1.4)

$$E_n = E_n^{(o)} + E_n^{(1)} H + E_n^{(2)} H^2 + ... \tag{1.4}$$

Hence, the mean magnetic moment of an ion in the level *n* is given as

$$\mu_n = -\frac{\partial E}{\partial H} = -E_n^{(1)} - 2E_n^{(2)} H \tag{1.5}$$

Substituting this result in equation (1.2), and assuming the first order splitting is $\gg kT$, and after some algebraic manipulations, the following result can be obtained (M73):

$$\langle \mu \rangle = \frac{\sum_m H_m \sum_n \left(\frac{E_n^{(1)^2}}{kT} - 2E_n^{(2)} \right) e^{-E_n^{o}/kT}}{\sum_n e^{-E_n^{o}/kT}} \tag{1.6}$$

where *m* represents the field directions. Since the effect of a magnetic field on the energy levels of an atom is usually small, E_n's can be calculated by the use of the perturbation theory. The first order terms, $E_n^{(1)}$, known as the Zeeman terms, indicate how the states change energy in the presence of the field, and are given by

$$E_n^{(1)} = \langle \psi_i | \mu_n | \psi_i \rangle \qquad (1.7)$$

The second order terms are given by

$$E_n^{(2)} = \frac{\sum_{i \neq j} |\langle \psi_i | \mu_n | \psi_j \rangle|^2}{E_j^o - E_i^o} \qquad (1.8)$$

The susceptibility of a material in the presence of a magnetic field is the scalar ratio of the magnetization and the magnetic field (O82)

$$\chi = \frac{M}{H} \qquad (1.9)$$

and then the susceptibility is given by

$$\chi = \frac{\langle \mu \rangle}{H} = \frac{\sum_n \left(\frac{E_n^{(1)^2}}{kT} - 2E_n^{(2)} \right) e^{-E_n^\circ / kT}}{\sum_n e^{-E_n^\circ / kT}} \qquad (1.10)$$

This equation is known as the Van Vleck equation, it was derived so that when solved for a particular interaction Hamiltonian and eigenvector basis set it gives a closed form equation for the magnetic susceptibility (O82). So, the requirements for using this equation are a knowledge of energy eigenvalues and eigenvectors.

It is possible to simplify the Van Vleck equation in various circumstances. This is done to allow us to understand the origin of the various generalizations about magnetic behavior in transition metal compounds, in particular the dependence of the magnetic moment on the temperature and its relation to structure. There are four general limiting cases in which this equation can be considered:

1- There are only energy levels $\ll kT$ above the ground level. In this case the only wavefunctions to be taken into account are those of a set which is degenerate in the absence of a magnetic field. The first order Zeeman effect alone contributes to the susceptibility of the ground levels and the susceptibility is then reduced to the famous Curie Law (F66)

$$\chi = \frac{C}{T} \qquad (1.11)$$

where C is the Curie constant and is given by

$$C = \frac{N g^2 \mu_B^2 S(S+1)}{3k} \qquad (1.12)$$

Which is often written as

$$C = \frac{N (\mu_{eff})^2}{3k} \qquad (1.13)$$

where μ_{eff} is the effective moment.

2- There are only energy levels $\gg kT$ above the ground level, which have no first order Zeeman effect. The only contribution to the susceptibility comes from the second order Zeeman effect between the ground level and the higher levels. The second order Zeeman effect contribution to the susceptibility of the ground levels is commonly put in the form

$$\chi = N \alpha \qquad (1.14)$$

where

$$\alpha = -\frac{2}{n} \sum_n E_n^{(2)} \qquad (1.15)$$

the summation is taking place over the *n* wavefunctions of the *n*-fold degenerate ground levels. This term is known as temperature independent or Van Vleck paramagnetism. A few points to be noted on this second order Zeeman effect susceptibility.

i- the susceptibility is temperature independent.

ii- it is small unless the temperature is very low, this is because the separation $(E_i^o - E_j^o)$ is large compared to kT.

iii- it is positive.

3-There are energy levels both $\gg$ and $\ll kT$ relative to the ground state. This situation arises when there is a ground state which is degenerate and all the excited states are $\gg kT$ above this (M73). For $\Delta E^o \ll kT$, the contribution to the susceptibility is given by the Curie law, while for $\Delta E^o \gg kT$, the contribution is given as in case 2. The total contribution is therefore given by

$$\chi = \frac{C}{T} + N\alpha \qquad (1.16)$$

This formula is often referred to as the Langevin-Debye equation.

This behavior is observed in any complex of octahedral or tetrahedral symmetry for which the ground term is of *A* or *E* symmetry, where *A* and *E* denote a singlet and doublet terms respectively.

4- There are energy levels $\approx kT$ relative to the ground level. In this case the first order Zeeman effects contribute to the total susceptibility according to the weight of the thermal distribution among them. In addition there is a contribution from the second order Zeeman effects between adjacent states. As a result the magnetic susceptibility is a complicated function of temperature, and each system must be treated individually. This behavior may be expected for transition metal compounds which have *T* symmetry, or triply degenerate, ground term. These terms are split by spin-orbit coupling interactions, and the resulting states are separated by a few hundred wave-numbers and thus will be thermally populated.

II- Spin-spin interactions:

Probably the most interesting phenomena in magnetism are those due to the spin-spin interactions. These interactions are referred to as magnetic exchange. The Hamiltonian used to describe the magnetic exchange interaction, known as the Heisenberg Hamiltonian, is of the simple form

$$H = -2J \sum_{ij} S_i . S_j \tag{1.17}$$

where J is the magnitude of the coupling between spins S_i and S_j, and is given by

$$J = \iint \phi_a(1)\, \phi_b(2)\, \frac{e^2}{|r_1 - r_2|}\, \phi_a(2)\, \phi_b(1)\, d\tau_1 d\tau_2 + \frac{b^2}{U} \tag{1.18}$$

where $\Phi_i(k)$ are the usual one-electron wave functions when electron k is in an orbital i. The first term is the Coulombic energy of a two electron charge distribution and the second is the antiferromagnetic contribution where b is the transfer integral of the electron between the two magnetic atoms and U is the energy of this transfer.

The above Hamiltonian in equation (1.17) provides a good description of the metal-metal interactions. However, it offers no information concerning the mechanism by which the spins couple. Metal-metal interactions in transition metal compounds frequently occur in spite of the fact that the separation between the paramagnetic centers is very large (≥4 Å). Because of the large distances involved this type of interaction is known as "*superexchange*" interaction (M68). The idea of the superexchange was introduced first by Kramers (K34). He pointed out that the ions could cause spin-dependent perturbations in the wavefunctions of the intervening ions, thereby transmitting the exchange effect over large distances; but no specific mechanisms were discussed. Anderson (A50) used Kramers' results as a starting point for his continued development of the theory of superexchange. Anderson (A63) concludes that three spin-dependent mechanisms are of much quantitative significance, these are:

1- Superexchange or (kinetic exchange) the kinetic energy promotes electron transfer between magnetic ions provided their d-orbitals overlap. Since the spins must be aligned antiparallel by the Pauli principle, the effect is always antiferromagnetic.

2- Direct exchange which is always positive and represents the repulsive interelectronic potential energy. This term is generally small compared with superexchange term when the latter is present.

3- Spin polarization. Anderson estimated that this term will be very small and can be ignored in the qualitative discussions.

The great merit of Anderson's theory is that it puts a firm theoretical basis for the exchange interactions, but the main drawback of the theory has been the quantitative use which remain to be practically impossible.

The important contribution of Anderson's work is his recognition that the superexchange mechanism has a directionality property. Anderson showed, for the manganese oxide, MnO, that the 180° superexchange through the bridging oxide ion was more powerful than that occurring through 90° pathways. This appears to be the first correlation of the structural and magnetic properties. Anderson discussed the role of the orthogonality relationships between the d-orbitals of the cation and the occupied orbitals of the intervening anions in determining whether the transfer of an electron between the metal and the anion can occur. Goodenough (G55) (G58) and Kanamori (K59) proposed some rules based on the orthogonality relationships that are helpful in determining the sign of the exchange integral between them. They can be expressed as follows (B90):

1- When the two ions have lobes of magnetic orbitals pointing toward each other in such a way that the orbitals would have a reasonably large overlap integral, the exchange is antiferromagnetic;

2- When the orbitals are arranged in such a way that they are in contact but have no net overlap integral, the interaction is ferromagnetic;

3- If a magnetic orbital overlaps an empty orbital, the interaction between the two ions is ferromagnetic.

In this regard, two extreme cases can be distinguished, the 180°- and the 90°-superexchange pathways.

1- the 180° superexchange case: this arrangement could be found in structures that have corner shared octahedra. The important symmetry relationships are those illustrated in Fig(1.1a). The p_σ and the t_{2g} are orthogonal so that no net overlap results and the electron transfer from $p_\sigma \rightarrow t_{2g}$ can not occur. On the other hand, the metal e_g and anion p_σ orbitals are not orthogonal and a $p_\sigma \rightarrow e_g$ pathway is available for electron transfer.

2- The 90° superexchange: the relation between the symmetries of the relevant orbitals of the interacting cations and anions at an angle of 90° is shown in Fig(1.1b). Both the $p_{\sigma x}$ and the $p_{\sigma y}$ orbitals are simultaneously involved in the superexchange mechanism.

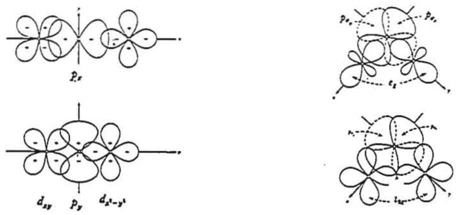

Fig(1.1) Symmetry relations between (a) t_{2g}, e_g and p_σ; and t_{2g}, e_g and p_Π orbitals oriented at 180°; (b) e_g and p_σ; and t_{2g} and p_σ orientated at 90° (Ref M68).

No attempt is made here to itemize every possible interaction but to stress the relevant symmetry relationships between anion and cation orbitals, and their importance to determine the sign and magnitude of the possible interactions.

III- Long Range Order:

A long range order occurs when these spin interactions take place cooperatively over the entire three dimensional lattice. Transitions to long range order are characterized by a susceptibility behavior,Fig(1.2), that is quite different from what has been described above. In other words, the transition from the paramagnetic state to a magnetically ordered state with long range correlations between the magnetic moments is in fact a phase transition (C86). This spontaneous ordering of spins persists below a certain critical temperature, usually called T_c [1]. In real systems, spin correlations among moments begin to accumulate even above the T_c, and these spin correlations are called short range order. The earliest and certainly the simplest theory that was formulated to explain the existence of the long range order in magnetic systems was the Mean Field Theory, MFT. Although it was very simplistic, it was very useful in describing the magnetically ordered state. The theory is briefly described in the following section.

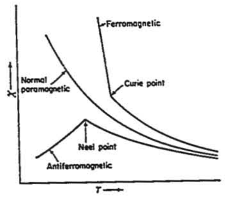

Fig(1.2) A comparison of the characteristics variation of susceptibility with temperature for paramagnetic, antiferromagnetic, and ferromagnetic materials.

---

[1] We adopt the convention of de Jongh and Miedema (J74) and use the T_c as the abbreviation for a critical temperature, whether the transition is ferromagnetic or antiferromagnetic order.

III.1- Mean Field Theory:

The Mean Field Theory, MFT, was first introduced by Weiss (W07). The task of the theory at that time was to explain the existence of spontaneous magnetization below the ordering temperature, and the passage from negligible total magnetization to saturation magnetization upon the application of a small external field H_0.

Weiss assumed that the exchange interactions between the magnetic ions give rise to an effective field, H_m, acting on the spins, in addition to the external field, H_0. This internal field H_m is proportional to the magnetization,

$$H_m = \lambda M \tag{1.19}$$

where λ is called the Weiss field constant, and is related to the number of nearest neighbors, *z*, and the exchange constant, *J*, by

$$\lambda = \frac{2zJ}{g^2 \mu_B^2} \tag{1.20}$$

The total field is therefore

$$H_T = H_{ext} + H_m \tag{1.21}$$

so

$$\frac{M}{H_T} = \frac{M}{(H_{ext} + \lambda M)} \tag{1.22}$$

Rearranging equation (1.22) to obtain the susceptibility yields the Curie-Weiss law

$$\chi = \frac{C}{T - \theta} \tag{1.23}$$

where θ is the Weiss constant,

$$\theta = \frac{N g \mu_B H_m S(S+1)}{3k} \tag{1.24}$$

When $H_{ext} = 0$, M is not zero at T_c. The spontaneous magnetization in the long range order is (C86),

$$M = N g \mu_B S B_S(\eta) \tag{1.25}$$

where $B_s(\eta)$ is Brillouin function (M73):

$$B_S(\eta) = \frac{S+1}{S} \coth\left(\frac{S+1}{S}\eta\right) - \frac{1}{S}\coth\left(\frac{\eta}{S}\right) \tag{1.26}$$

with

$$\eta = \frac{g \mu_B H_T}{kT} = \frac{g \mu_B (H_{ext} + \lambda M)}{kT} \tag{1.27}$$

Let us examine the spontaneous behavior by setting $H_{ext}=0$.

As T → 0, $\eta \rightarrow \infty$, and

$$B_S(\eta \rightarrow \infty) = 1 \tag{1.28}$$

so that equation(1.25) becomes:

$$M(T \rightarrow 0) = N g \mu_B S \tag{1.29}$$

Spontaneous magnetization is usually expressed as a reduced magnetization function, and one can define two independent relationships for the reduced magnetization M(T)/M(0):

$$\frac{M(T)}{M(0)} = B_s(\eta) \tag{1.30}$$

and

$$\frac{M(T)}{M(0)} = \frac{(\eta k T)}{(N g^2 \mu_B^2 S \lambda)} \tag{1.31}$$

These two equations can be examined graphically as in Fig(1.3).

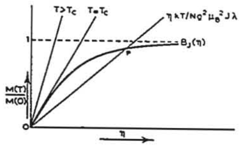

Fig(1.3) Graphical method for the determination of the spontaneous magnetization at a temperature T (Ref C86).

For T>T_c there is no intersection with the Brillouin function. Therefore, there is no solution for M(T)/M(0) above T=0 K. For T<T_c there is a non-zero solution for every temperature at the point where the Brillouin function is intersected. As T approaches T_c, the reduced magnetization is best represented by the relationship (1.32),

$$\frac{M(T)}{M(0)} = K\left(\frac{T_c - T}{T_c}\right)^{\beta} \tag{1.32}$$

the exponent β is referred to as the critical exponent which, according to the MFT, has a value ½.

To account for the magnetic behavior of salts with complicated lattice structures, Néel (N32) introduced a modification of the Weiss model of the ferromagnetism. He assumed that the ordered magnetic arrangement can be described in terms of sublattices, each is ferromagnetic but the spins of one sublattice are antiparallel to the spins on another sublattice. These two sublattices are coupled by a negative λ_{ab}. In this case at high temperatures the magnetization is given as in equation (1.33) (K66),

$$M = M_a + M_b = \frac{C}{T}\left(H_o + \frac{1}{2}(\lambda_{aa} + \lambda_{ab})M\right) \tag{1.33}$$

giving

$$\chi = \frac{C}{T + \Theta} \tag{1.34}$$

with $C = C_a + C_b$, and $\Theta = ½C(|\lambda_{ab}| - \lambda_{aa})$

Below the ordering temperature, the antiparallel ordering opposes the aligning tendency of the applied field, H_0, and the susceptibility drops with decreasing temperature. Thus

antiferromagnets are usually characterized by a sharp kink in the χ versus T curve. Below T_c, for a single crystal sample, the susceptibility is strongly dependent on the direction between H_0 and the preferred axis of magnetization. For H_0 along this direction, $\chi_{\parallel}$ drops to zero at 0 K. With H_0 perpendicular to this axis, the spins have a tendency to line up with the field. In a powder on average 2/3 of the crystallites will be perpendicular to H_0 and 1/3 will be parallel. Hence the susceptibility at 0 K will be $2/3\chi_{\perp}$.

Surprisingly enough, MFT offers a remarkably good approximation to many of the properties of the ordered substances. It is successful in predicting spontaneous magnetic long range order. Near the ordering temperature, T_c, it predicts that the spontaneous magnetization and susceptibility obey a power law behavior in the reduced temperature ***t***,

$$M \,\alpha\, (-t)^{\beta} \tag{1.35}$$

$$\chi \,\alpha\, (t)^{-\gamma} \tag{1.36}$$

with $\beta = ½$ and $\gamma = 1$. It is now well established that in the majority of cases the critical behavior of a thermodynamic function *f(t)* is described by a power law in the reduced temperature, t, near T_c where $t = (T - T_c)/T$ (J92). The investigation in the magnetic critical phenomena is an area of extensive research among both physicists and chemists.

The major error in the MFT model is that it neglects short range spin correlations. So, in the MFT the magnetic interaction of a given spin with its *z* neighbors

is replaced by an average interaction with all the other spins in the lattice (J92). This makes MFT insensitive to the dimensionality of the magnetic lattice. MFT can not accurately describe the critical behavior, by which is meant the singularities occurring in the thermodynamic functions at T_c.

It can be concluded that the MFT is a rough approximation to describe the long range order, LRO, in a magnetic system, and fails for systems with lower dimensionality where the short range order, SRO, dominates.

III.2- Ising, XY, and Heisenberg Models:

As the dimensionality of the system is reduced from three to two or one, *i.e.* the spin interactions become dominant in the planes or along the chains, respectively, MFT is expected to become a worse approximation of the system (C86). It was observed that the behavior of various thermodynamic quantities changes more between the different lattice dimensionalities than they do between different structures, *e.g.* simple cubic to body centered cubic, of the same dimensionality. This led to the introduction of other models that are capable of representing the observed data. In order to choose a model for a certain magnetic system, it is necessary to define its lattice dimensionality, ***d***. The discussion of the concept of the lattice dimensionality will be delayed until the next section.

The other important quantity which has to be defined is the spin dimensionality of the system. Spin dimensionality is related to the anisotropy in the exchange

interactions. There are three limiting cases which have been studied extensively, namely the Ising, XY, and Heisenberg models.

The Hamiltonian of the spin interactions in equation (1.17) can be modified to be capable of explaining both the coupling and anisotropy in the magnetic exchange in the following way:

$$H = -2\sum_{ij}(J_x S_{ix} S_{jx} + J_y S_{iy} S_{jy} + J_z S_{iz} S_{jz}) \tag{1.37}$$

Depending on the number of the components (*x,y,z*) of the spins that are considered, *n*, one has a 1, 2 or 3 component spin system, where *n* denotes the spin dimensionality. The Heisenberg model is obtained if the interactions are isotropic, *i.e* $J_x = J_y = J_z$, $n=3$; and the XY model is obtained when the interactions are dominant in the plane, $J_x = J_y$ *and* $J_z = 0$, $n=2$. When the interactions in the plane are $J_x = J_y = 0$ *and* $J_z = 1$, $n=1$ and the Ising model obtains. Both the XY and Ising models are obtained by assuming an anisotropy in the exchange interaction.

In practice, anisotropic properties often arise not as much from the exchange interaction but rather from other sources such as the crystal field that couple the moments in certain direction in the crystal, the spin-orbit coupling, and the single ion effects (J85).

The anisotropy in the magnetic susceptibility arises, in general, from the non-cubic nature of the ligand field acting on the metal ion. Since the spin contribution to the susceptibility is spatially isotropic, the anisotropy in the susceptibility arises from the orbital contribution (M78).

If the ground state of an ion is an orbital singlet, it has no orbital contribution in the ground state, hence no anisotropy is expected and the exchange interactions are isotropic. This system is expected to behave as a Heisenberg system. On the other hand, when the ground state is triply degenerate, the behavior of the susceptibility is expected to be highly anisotropic and the Ising model obtains.

Consider the case of the Co^{2+} ion. In a cubic octahedral environment the orbital ground state of a Co^{2+} ion is the triplet $^4T_1$. Axial distortions from cubic symmetry, combined with spin-orbit coupling, split this manifold state into six doublets, known as Kramers doublets. One doublet remains lowest in energy, irrespective of the sign or magnitude of the axial distortion, the next doublet being about 200 K higher in energy. It follows that at temperatures below 50 K only the lowest doublet will be appreciably populated, so that the magnetic properties can be described within the effective spin $S'=½$ formalism. It can be readily shown that in the ground-state doublet the true spin $S=3/2$ may be replaced by an effective spin $S'=½$ with (J85):

$$\begin{aligned} S_x &= ½ g'_{s\perp} S'_x \\ S_y &= ½ g'_{s\perp} S'_y \\ S_z &= ½ g'_{s\parallel} S'_z \end{aligned} \tag{1.38}$$

where the splitting factors $g'_{s\perp}$ and $g'_{s\parallel}$ are the contributions of the spin angular momentum to the effective g values of the lowest doublet. For sufficiently large

distortions, $g'_{\parallel}$ and $g'_{\perp}$ will differ considerably so that the effective exchange interactions will be quite anisotropic, and the effective exchange interactions will be introduced as

$$\begin{aligned} J'_{\parallel} &= (g'_{s\parallel}/2)^2 J \\ J'_{\perp} &= (g'_{s\perp}/2)^2 J \end{aligned} \tag{1.39}$$

Similar considerations can be applied to certain Fe^{2+} compounds.

Systems with high anisotropy could adopt either of the two anisotropic models, namely the Ising or XY model. Considerable anisotropy in the g-values with $g_{\perp} \gg g_{\parallel}$ is a prerequisite for the applicability of the XY model.

On the other hand, it follows that the Heisenberg case will be approached with magnetic ions for which crystal field effects are small, as in the case of Mn^{2+} where the orbital momentum is quenched completely ($L=0$) (J85).

For metal ions with an orbital singlet ground state and $S>½$, the spin-orbit interaction partially lifts the spin degeneracy of the ground state and leaves a set of spin states. This is called zero-field splitting (ZFS), the interested reader is referred to ref (C85) for a detailed and complete discussion of this phenomenon. As an example, consider Ni^{2+} ion for which the ground state in the cubic field is a spin triplet, $^3A_{2g}$. The trigonal or tetragonal distortions of the cubic environment will split the ground triplet into a singlet and a doublet. It may be convenient to add the crystal-field term to a Heisenberg-type of interaction, i.e. to consider the Hamiltonian

$$H = -2J \sum_{ij} S_i . S_j - D \sum_i S_{iz}^2 \tag{1.40}$$

Depending on the sign of the distortion either the singlet or the doublet is lowest in energy, corresponding with $D<0$ and $D>0$, respectively. It follows from this Hamiltonian that the crystal field then establishes a preference for the moments to align perpendicular or parallel to the *z*-axis, corresponding to a planar (XY-type) or axial (Ising-type) type of anisotropy. In the case that $|D| \ll |J|$, the isotropic Heisenberg model will be approached (J85).

Based on this discussion, certain generalizations are useful: Mn^{2+} is often a Heisenberg ion while Cu^{2+} is likely to be; Co^{2+} is likely to be Ising or XY ion, depending on the geometry of the ion and the sign and the magnitude of the zero-field splitting.

IV- Short Range Order:

For operational purposes, the term will be restricted to describe magnetic ions which interact predominantly with neighbors that are arranged in clusters, in chains, or in planes. There are a number of reasons which may cause the lack of an appreciable magnetic interaction between neighbors along one or more spatial directions in a crystal. Since the magnetic and the crystallographic lattice need not be identical, this property may be utilized by choosing a lattice in which the distance between the magnetic ions

along a given direction is much longer than along the other directions. The magnetic ions may, for example, be largely separated along certain axes by putting non-magnetic atoms in between them. In addition a lower dimensionality may be realized by the fact that both signs of the superexchange interaction do occur, depending on the path lengths and bond angles. This offers the possibility of an accidental cancellation of the interaction in a given direction, if there exist different bonds in that direction.

It is instructive to give a brief summary of the properties of the magnetic lattices of low dimensionality with some examples illustrating the subtle relationship between the magnetic and structural dimensionalities.

IV.1- Chain structures:

There are a number of theories available to describe the thermodynamic properties of the one dimensional magnetic systems and extensive experimental data on magnetic chains (J74)(C86). The obvious feature of the thermodynamic behavior of the 1-d systems is the absence of long-range order at any non-zero temperature. As a consequence of this, the entropy has to be removed via short range processes. This is reflected in the specific heat and magnetic susceptibility behaviors, both of which display broad maxima, occurring at temperatures of the order of the exchange interaction along the chain (J74). Plots in Fig(1.4) show the specific heat of the magnetic chains of the three model systems. The magnitude of the susceptibility maximum can provide a handy set of criteria for the determination of the model system appropriate to the compound at hand. The fit of the data to other calculated quantities within each model is very useful in determining the model that will be most representative to the data. For an elaborate discussion on these quantities the interested reader is referred to ref (J74).

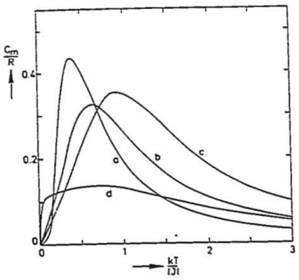

Fig(1.4) Theoretical heat capacities of a number of magnetic chains with S = ½. (a) and (b) correspond to the Ising and the XY model, respectively (ferro- and antiferromagnetic). Curves (c) and (d) are for the antiferromagnetic and ferromagnetic Heisenberg chain, resp. (Ref J74).

It should be realized that assigning the correct model to represent the experimental data may become nontrivial. Crystallographic structures are usually necessary in order to aid in the choice of the models to apply. But some inferences may not be unambiguous.

Regarding the Ising model system, the zero-field susceptibilities have been derived by Fisher (F63) for the $S=½$ chain. They are

$$\chi_{\parallel} = \frac{N g_{\parallel}^2 \mu_B^2}{2J} \left(\frac{J}{2kT} \right) e^{J/kT} \tag{1.41}$$

$$\chi_{\perp} = \frac{N g_{\perp}^2 \mu_B^2}{4J} \left[\tanh\left(\frac{J}{2kT}\right) + \left(\frac{J}{2kT}\right) sech^2\left(\frac{J}{2kT}\right) \right] \tag{1.42}$$

where the symbols "parallel" and "perpendicular" refer to the external magnetic field direction with respect to the direction of the spin alignment within the chains.

Several compounds containing Ising chains have been studied. $AMCl_3.2H_2O$ where A = Rb and Cs and M = Co and Fe, has been extensively studied and found that the intrachain coupling is antiferromagnetic. While the spins in the system $[(CH_3)_3NH]CoCl_3.2H_2O$ are ferromagnetically aligned (C86).

With respect to the Heisenberg chains, there are no exact solutions available to date. However, numerical calculations are available which characterize the behavior of the chains to a high degree of accuracy. The classical work on the antiferromagnetically exchange-coupled chain was done by Bonner and Fisher (B64), and much of the subsequent work has been carried out in the spirit of this work. The expression in equation (1.43) was later derived which was used to calculate the magnetic susceptibility of some magnetic chains.

$$\chi = \frac{N g^2 \mu_B^2 S(S+1)}{3kT} \cdot \frac{1-u}{1+u} \tag{1.43}$$

where $u=(T/T_o) - coth(T_o/T)$ with $T_o=2JS(S+1)/k$

It is worth to note that the short range order effects for this model system are extended over a much larger region in temperature than for the Ising model.

One of the best Heisenberg chains is $[N(CH_3)_4]MnCl_3$ (H74), the structure of which consists of chains of S=5/2 Mn^{2+} ions bridged by three Cl ions. The intrachain exchange constant is -6.7 K. Both the magnetic susceptibility and the specific heat were measured and broad maxima were observed in both measurements. The ratio J'/J was determined to be in the order of 10^{-4}, where J' represents interchain exchange. This ratio is a crude measure of the idealization of the chain model. Another measure of this idealization is the critical entropy, a mere 1% of the total for this compound (C86).

A large number of chain structures are formed by Cu^{2+}. This is largely a result of the ability of Cu^{2+} to adopt to a number of coordination geometries. Excellent reviews of 1-d copper magnetic systems are published by Hatfield *et al* (H93) (H85). Of those chain compounds, the compound $Cu(py)_2Cl_2$ has received much attention since well-defined, large single crystals may be obtained. It was concluded that the spins couple antiferromagnetically in the Heisenberg chain with J/k= -9.15 K.

Another interesting compound that illustrates the magneto-structural correlations is the compound $K_2Pb[Cu(NO_2)_6]$ (B79). This compound has a centered cubic structure at room temperature, implying three- dimensional magnetism, but it undergoes several structural phase transitions as it is cooled and acts as an antiferromagnetic linear chain as well. This has been explained in terms of Jahn-Teller distortions which are propagated cooperatively throughout the crystal lattice.

Another example that illustrates this point further is $KCuF_3$ (J92), the structure of which is a distorted perovskite. The environment of the CuF_6 is tetragonally distorted octahedron. This distortion leads to a lack of overlap in the basal plane, leaving only the overlap along the c-axis,Fig(1.5). The resulting Cu-F-Cu-F-Cu superexchange along the c-axis yields a strong antiferromagnetic interaction along the chains.

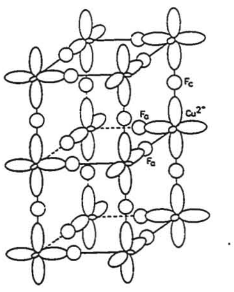

Fig(1.5) The alignments of the d orbitals of the Cu^{2+} ion in $KCuF_3$. The positions of the F atoms are also shown. The 1-d behavior arises because there is hardly any overlap of the wavefunctions along the a-axes (Ref J74).

With respect to the XY model, considerable anisotropy in the g-values, with $g_\perp > g_\parallel$, is the prerequisite for its applicability. There are only few compounds which adopt this model system. One such material that meets such a criterion is $(N_2H_5)_2Co(SO_4)_2$, with $g_\perp=4.9$, and $g_\parallel=2.20$ (W74).

One of the recent advances in the research in the magnetic properties of low dimensionality is the synthesis and study of one dimensional ferrimagnets. This new class of low dimensional systems has been discovered in 1980 in compounds showing structurally ordered bimetallic chains. This class of materials shows very interesting magnetic behavior. These ferrimagnets were a subject of a review article published recently by Coronado *et al* (C93).

IV.2- Layered structures:

In going from the 1-d to the 2-d magnetic lattices there arises a profound difference between the Ising model on one hand and the Heisenberg and XY models on the other. The dimension of two is sufficient for the Ising model to undergo a long range order at a finite temperature but this is not the case for either the XY or the Heisenberg model systems.

The important calculation for the 2-d systems within the Ising limit is that of Onsager (O44) for an $S=\frac{1}{2}$ system. He showed that the quadratic lattice undergoes a phase transition and exhibits a λ-type anomaly in the specific heat.

Turning to the isotropic models, the first point of interest is that the 2-d Heisenberg system does not undergo a transition to a long range order. The specific heat of the planar Heisenberg system consists of a broad maximum. The shape of this curve differs from the 1-d model, but has no λ-type anomaly. Similarly, the susceptibility shows a broad maximum due to the short range order effects at the higher temperatures. Fig(1.6) illustrates the theoretical predictions of specific heats of the $S = \frac{1}{2}$ Ising model as well as Heisenberg model for a 1, 2, and 3-d lattice, the molecular field prediction is also included.

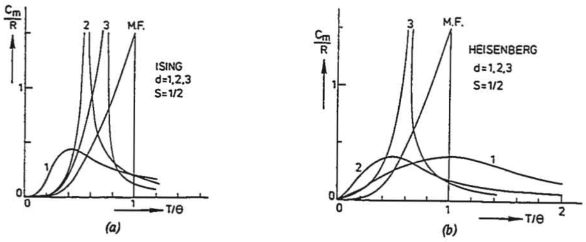

***Fig(1.6)** The theoretical magnetic specific heats of the $S=\frac{1}{2}$ (a) Ising model for 1, 2 and 3-d lattice. (b) Heisenberg models for a 1, 2, 3-d lattice. MFT prediction included for comparison. R is the gas constant and θ is the Curie-Weiss temperature (Ref J74).*

One of the most extensively studied series of the two-dimensional systems is based on the K_2NiF_4 structure. The tetragonal K_2NiF_4 structure can be viewed as being derived from the perovskite lattice, $KNiF_3$, by the addition of an extra layer of KF between NiF_2 sheets as in Fig(1.7). This will transform the 3-d lattice of the $KNiF_3$ into a magnetic layer structure, K_2NiF_4. It is important that the interaction within the layer is antiferromagnetic, since this causes a cancellation of the interaction between neighboring layers in the ordered state. A series of compounds of the general formula K_2MF_4, where M is Mn, Fe, Co, Ni, and Cu, (J74) has been synthesized and studied. Their crystal structures are all similar and their magnetic properties could be explained within the limit of 2-d magnet.

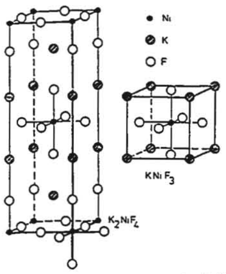

***Fig(1.7)** The crystal structures of K_2NiF_4 and $KNiF_3$ (Ref J74).*

The first clue to the 2-d properties was predicted by Legrand *et al.* (L62) who investigated K_2NiF_4 by neutron diffraction. It was argued that in the antiferromagnetic state the exchange and the dipolar interaction between neighboring Ni^{2+} sheets will cancel. Subsequent susceptibility measurements on K_2NiF_4 showed the familiar 2-d feature. Short range order was found to persist up to $T = 2T_c$. Values for the intralayer exchange constant are obtained from different measurements, given $J/k=-50K$ while the next-nearest interaction within the plane to be $J'/k = -0.5$ K ($J'/J = 10^{-2}$). From $T(\chi_{max})=230$ K, it follows that $J/k = 52$ K.

Another member of the series which was studied extensively is K_2MnF_4. It was found to exhibit similar characteristics in its magnetic susceptibility to those of K_2NiF_4. From the fit of the susceptibility data to a high temperature expansion, it was found that $J/k=-4.2$ K. Both of these compounds were fit to a quadratic Heisenberg model.

In the compound K_2CoF_4, the resultant lowest doublet from the spin-orbit coupling is well approximated by the effective spin of $S=\frac{1}{2}$ with $g_\parallel=6.3$ and $g_\perp=3.1$ (H92.1) This would indicate a strong Ising 2-d behavior. The parallel susceptibility data could nicely be fitted to the 2-d Ising predictions over a wide range of temperatures. It was shown that spontaneous magnetization which was obtained from a neutron diffraction study is in full agreement with Onsager's exact solution (O44) which is given in equation(1.44)

$$\frac{M(T)}{M(0)} = \left(1 - \sinh^{-4}\frac{J_I}{kT}\right)^{1/8} \qquad (1.44)$$

K_2CuF_4 was also subject to intensive investigations by a number of researchers (B80). It is an excellent realization of the 2-d ferromagnet with S=½. K_2CuF_4 has a relatively large J'/J ratio (2×10^{-4} compared to 10^{-5}-10^{-6} for other members). In the compounds with an antiferromagnetic order in the layers the interlayer coupling between next nearest planes is canceled by symmetry, but this cancellation will not occur in the case of ferromagnetically ordered layers, leading to a much stronger interlayer coupling but too weak to alter the 2-d character of this compound.

The correlation between crystallographic structure and magnetic exchange which the chemist would like to observe is in fact rather remarkably displayed by this series of compounds.

Another system which shows subtle magneto-structural correlations is the La_2CuO_4. Contrary to the case of $KCuF_3$ where the elongation occurred in the plane, in this material the elongation axes of the octahedra align parallel to the c-axis. A (001) projection of the La_2CuO_4 structure is shown in Fig(1.8). This, in turn, will lead to very little overlap along the c-axis, but a strong overlap in the basal plane. It is this mechanism which is responsible for the strong antiferromagnetic exchange found in La_2CuO_4, making it an excellent example of a 2-d antiferromagnet (J92).

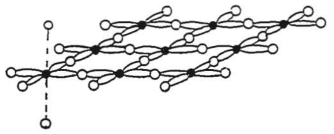

Fig(1.8) The basal plane of La_2CuO_4 showing the orbital ordering (Ref J92).

Another interesting series of layered complexes of the formula $M(NCS)_2(triazole)_2$ has been studied extensively by Engelfriet *et. al.* (E80). In these complexes, the M^{2+} ions are on a face-centered orthorhombic lattice. The M^{2+} ions in adjacent layers are far apart (≈9Å) and the interlayer exchange path involves an (NCS) unit besides the triazole ring. For these reasons, the magnetic behavior is expected to show pronounced 2-d characteristics, with ratios of inter- to intralayer interaction of the order $|J'/J| \approx 10^{-2}$-10^{-3}.

Starting with $Fe(NCS)_2(triazole)_2$, the Fe^{2+} ion has a low-lying doublet with a high uniaxial Ising anisotropy of the g-tensor. Consequently, both the magnetic susceptibility and the specific heat could be fitted to the prediction for the (quadratic) 2-d Ising model, with J/k = -7.24K.

The magnetic properties of $Mn(NCS)_2(triazole)_2$ are similarly well described by theoretical predictions for the S=5/2, quadratic layer Heisenberg antiferromagnet with J/k = -.25K.

The specific heat of $Cu(NCS)_2(triazole)_2$ is fitted to the quadratic layer S=½ Heisenberg ferromagnet. It is interesting to observe that the intralayer interaction changes from being antiferromagnetic into being ferromagnetic as soon as the Jahn-Teller ion is taken into consideration (J83).

Regarding the 2-d XY-model, only very few experimental examples have been studied as yet. This is because of the lack of compounds that exhibit the required anisotropy for the XY model. Just recently Regnault *et al* (R92.1) described the magnetic properties of the compounds $BaM_2(XO_4)_2$, where M is Ni or Co and X is P or As. All of these compounds are isostructural and crystallize in a trigonal space group R-3.

The structure can be described as a layered structure of magnetic ions that are located on a honeycomb lattice. The distance separating these layers is ≈ 7.8 Å and separated by XO_4-Ba-XO_4. From the large interlayer distance, a pronounced 2-d magnetic character is expected. The planar nature of the anisotropy was clear in the magnetic susceptibilities $\chi_\perp$ and $\chi_\parallel$.

For $BaCo_2(AsO_4)_2$ the perpendicular and parallel susceptibilities appear to differ by more than an order of magnitude in the low temperature range. Analysis of these data gives $J_\perp/k = 20$ K, $J_\parallel/J_\perp \approx 0.4$, $g_\perp = 5.0$ and $g_\parallel = 2.5$. These parameters do indeed satisfy the requirements of the XY-model.

Based on this brief summary of the thermodynamic properties of the various magnetic models, it is apparent that it is a difficult task to assign a certain model which fits the observed data. To make such an assignment even more difficult, isolated dimers and clusters offer specific heat and susceptibility curves that are not unlike those of the 1-d and 2-d systems (C86). Accordingly, powder measurements of the susceptibility are sometimes unreliable as indicators of magnetic behavior on their own and crystallographic structures are usually necessary in order to aid in the choice of models to apply. Qualitative comparison of the shape of the theoretical and experimental data are inadequate in order to characterize the magnetic behavior of a substance. A quantitative analysis of the data and quantitative fit to a model are imperative (C86).

In summary, in order to completely define a magnetic system, it is necessary to determine:

1- Its lattice dimensionality, d.

2- Its spin dimensionality, n.

3- The sign of the exchange interaction, whether it is ferromagnetic or antiferromagnetic.

4- The magnitude of the exchange interaction, which can be determined by fitting the experimental data to a proper theoretical model.

V- Research Outline:

The transition metal oxides of the general formula AB_2O_6, where A is a divalent transition metal ion and B is a pentavalent diamagnetic ion, *e.g* Ta^{5+}, Sb^{5+}, or As^{5+}, have been subject of an extensive study in our labs.

These oxides adopt different crystal structures depending on the relative sizes of ions A^{2+} and B^{5+} (W84). Most of the transition metal antimonates and tantalates, with the exception of $MnSb_2O_6$ and $CuTa_2O_6$, adopt the trirutile structure (E84)(W84). The trirutile structure is a superlattice of the normal rutile unit cell formed by tripling the *c*-axis. On the other hand, the transition metal arsenates crystallize in a hexagonal structure, known as $PbSb_2O_6$ structure, in which the A^{2+} and As^{5+} ions are segregated in layers (W84). In the present investigation, our attention was directed at studying the structural and magnetic properties of $ASb(As)_2O_6$, where A is Cu, Mn, Fe, Co, and Ni and B is Sb or As.

The trirutile structure imposes restrictions on the distances and bond angles which connect magnetic ions thus dictating the potential exchange pathways which can give rise to magnetic correlations. The sublattice of the magnetic ions in the structure has *I4/mmm* symmetry, the same as that found in the K_2NiF_4 and other layered tetragonal compounds. The magnetic ions in layer $z=0$ are separated from those in the layer at $z=½$ by about 5.7Å and the superexchange would involve tortuous A-O-B-O-A linkages. Furthermore, if the moments in each plane exhibit short range antiferromagnetic order there will be a symmetry cancellation effect as each moment at $z=½$ sees eight neighbors in the two

adjacent planes, four with spin-up and four with spin-down. Both of these effects will most definitely lead to large short range ordering in these compounds.

Concerning the magnetic properties of trirutile phases, $ASb_2(Ta_2)O_6$ where A is Fe, Co, and Ni, the magnetic susceptibility in the range 100 - 300 K follows the Curie-Weiss law (E84)(R89.1). Below 100 K substantial deviations from this relationship were observed. Evidence for 2-dimensional correlations has been obtained from magnetic susceptibility as well as from heat capacity measurements (K88.1)(K88.2)(R89.1). The possibility of predominantly 1-d interactions in $FeTa_2O_6$ was suggested by the published magnetic structure for this compound (E86); however, a fit to a 1-d model was not successful.

As an extension to this study, $CuSb_2O_6$ will be investigated. This phase was reported to crystallize in a monoclinically distorted trirutile structure in space group *$P2_1/n$* or *$P2_1/c$*, but its structure was not refined. We will study the crystal structure using the neutron powder diffraction.

The magnetic susceptibility will be measured in the range 4 - 300 K. We expect to observe substantial short range order. Both possibilities of a 2-dimensional and 1-dimensional model systems do exist. Both the short range and long range orders will be thoroughly investigated. The findings of this study will be contrasted with those obtained from the other members of the series $ASb(Ta)_2O_6$.

As for AAs_2O_6, these compounds have received very little attention in the past. $CoAs_2O_6$ was synthesized by Magneli (M41). Later Taylor *et al* (T58) prepared and

analyzed with the use of X-ray powder diffraction both $NiAs_2O_6$ and $CoAs_2O_6$. It was reported that these arsenates have the lead antimonate structure but no effort to refine their structures has been attempted.

In general, published work on these oxides is very scarce. There has been no work reported concerning their magnetic properties.

The preparation and the refinement of the crystal structure of these arsenates will be discussed. The crystal structures will be studied using neutron powder diffraction. In addition, we will attempt to synthesize other members of this series that have not been reported in the literature. Based on the ionic radii of Mn^{2+} (0.83 Å) and Fe^{2+} (0.78), it is most likely that their corresponding compounds will adopt the lead antimonate structure as well.

The magnetic susceptibility of these oxides will be measured. The high temperature region of the susceptibility will be fitted to a Curie Weiss law. Based on the crystal structure, there appears no clear indication of any dominant exchange pathway that will lead to a low dimensional magnetism. Whether any appreciable short range order will be present depends on the relative strengths of inter- and intra-layer exchange interactions.

A thorough investigation of the long range order regime in these oxides will be attempted by the use of low temperature neutron diffraction. We will try to determine the magnetic unit cells of these phases. The determination of the magnetic structures of these compounds will be attempted by using the Rietveld refinement method.

Chapter 2

Neutron diffraction Theory

Thermal neutron scattering is one of the most powerful techniques for studying the structure and dynamics of condensed matter. This is because thermal neutrons have a wavelength which is comparable to the spacing between the atoms in a crystal. In addition, the energy of these neutrons is comparable to the vibrational frequencies of the atoms in the sample. These two properties allow us to use neutron diffraction as a probe to investigate both the structure and dynamics of the condensed state.

The second feature unique to neutrons is that they have a magnetic moment which can interact with unpaired electrons in the atoms of the matter. This makes it possible to study a wide range of magnetic properties and obtain information about magnetic systems which can not be obtained with other techniques.

In this chapter, the theory of the nuclear and magnetic scattering will be briefly reviewed. A section in this chapter will be devoted to the Rietveld method, a technique used in refining the chemical and magnetic structures using the powder patterns obtained from the scattering experiments.

I- Nuclear Scattering Theory:

The use of neutrons in diffraction experiments dates back to the 1950's, at which time a large number of crystal structures had been determined by X-ray diffraction. The main attention was drawn to the different scattering power of X-rays and neutrons which results from fundamental differences in the two scattering processes. Whereas X-rays, as electromagnetic radiation, interact with the electronic charge distribution in the irradiated material, neutrons are scattered to a large extent by interaction with the atomic nuclei through nuclear forces (C78). As a result, the two techniques allow the measurement of almost, but not quite the same quantity.

I.1- Nuclear scattering cross-section:

The incident neutron beam is characterized by its momentum, $\hbar k$, where k denotes the wave vector, $2\pi/\lambda$. The scattered neutrons likewise are characterized by their momentum, $\hbar k'$, so that the scattering can be discussed in terms of the momentum transfer, $\hbar Q$, where $Q=k-k'$. Very generally we can distinguish between two scattering processes: elastic scattering in which there is momentum transfer but no energy transfer in the scattering process and the other is an inelastic scattering which involves an energy transfer as well.

The results of a scattering experiment can be conveniently expressed in terms of a quantity known as a cross-section, σ. Concerning the elastic scattering process, one can distinguish two quantities: the total scattering, σ_s, which is defined by:

σ_{tot} =(total number of neutrons scattered per second)/Φ, where Φ is the flux of the incident neutrons. In this context, 'total number' means the number of neutrons scattered in all directions. The second quantity is the differential cross-section in the solid angle dΩ, and

dσ/dΩ = (number of neutrons scattered per second into dΩ/ ΦdΩ. These two cross sections are related by the following identity (S78).

$$\sigma_s = \int_{4\pi} \frac{d\sigma}{d\Omega}\, d\Omega \tag{2.1}$$

To derive an expression for the cross section, we shall first consider the simplest case - nuclear scattering by a single nucleus at a fixed position. Then, we derive the cross section of the scattering from a crystal lattice.

The interaction between a neutron and one single rigid nucleus can be roughly described by an attractive potential of about $r_o=10^{-13}$ cm range and some MeV depth, the details of which are not well known (S72). The incident neutrons are represented by the wavefunction

$$\psi_o = e^{ikr} \tag{2.2}$$

The wavefunction of the scattered neutrons at the point r can be written in the form

$$\psi_{sc} = -\frac{b}{r} e^{ikr} \tag{2.3}$$

where b is a constant, known as the scattering length, and r is the distance from the point of measurement to the origin at which the nucleus is considered to be rigidly fixed. The minus sign in the equation is arbitrary and corresponds to a positive value of b for a repulsive potential.

The cross section, as defined above, is just the flux passing through a sphere of radius r around the nucleus divided by the incoming flux

$$\sigma_s = \frac{|\psi_s|^2 . \nu . 4\pi r^2}{|\psi_o|^2 . \nu} \tag{2.4}$$

where ν is the neutron velocity. This gives

$$\sigma_s = 4\pi b^2 \tag{2.5}$$

The cross section can be defined in terms of the potential of the interaction between the neutron and the nucleus, V, as

$$\frac{d\sigma}{d\Omega} = \left(\frac{m}{2\pi\hbar^2}\right)^2 |\langle e^{ik'r} | V(r) | e^{ikr} \rangle|^2 \tag{2.6}$$

which can be rewritten simply as,

$$\frac{d\sigma}{d\Omega} = \left(\frac{m}{2\pi\hbar^2}\right)^2 |\int V(r)\, e^{iQ.r}\, dr\, |^2 \tag{2.7}$$

where $Q= k-k'$

The interaction potential between the nucleus and the neutron is of very short range, falling to zero outside a distance on the order of nuclear dimensions (~ 10^{-12} cm). For diffraction the neutrons must have a wavelength on the order of interatomic distances (~ 10^{-8} cm). Consequently, the nucleus acts as a point scatterer to neutrons. Therefore the scattering is isotropic, *i.e.* the scattering amplitude is constant and independent of Q.

The pseudopotential V(r) in equation (2.6) is constructed as (S78),

$$V(r) = a . \delta(r) \tag{2.8}$$

where δ(r) is a 3-dimensional Dirac delta function $\int \delta(r)\, dr=1$.

then

$$\int V(r)\, dr = a \int \delta(r)\, dr = a \tag{2.9}$$

therefore

$$\frac{d\sigma}{d\Omega} = \left(\frac{m}{2\pi\hbar^2}\right)^2 a^2 \tag{2.10}$$

where

$$a = \frac{2\pi\hbar^2}{m} . b \tag{2.11}$$

hence the potential is given by

$$V(r) = \frac{2\pi\hbar^2}{m} . b . \delta(r) \tag{2.12}$$

For many nuclei at R_j, equation (2.12) can be written as

$$V(r) = \frac{2\pi\hbar^2}{m}\sum_j b_j\,\delta(r - R_j) \qquad \textbf{(2.13)}$$

where b_j is the scattering length of the nucleus at position R_j. V(r) is known as the Fermi pseudopotential.

In a system with different nuclei, *e.g* a mixture of isotopes, each nucleus has, of course, a specific scattering length. Because we can not know which isotope is sitting on a given place R_i, b_i in equation (2.13) should be replaced by a proper average. The differential cross section for a neutron beam by an assembly of nuclei can then be rewritten as the sum of two parts:

$$\frac{d\sigma}{d\Omega} = \left(\frac{d\sigma}{d\Omega}\right)_{coh} + \left(\frac{d\sigma}{d\Omega}\right)_{incoh} \qquad \textbf{(2.14)}$$

Accordingly, one can distinguish between different definitions for the scattering cross section such as:

total scattering $\sigma_s = 4\pi<b^2>$

coherent scattering $\sigma_{coh} = 4\pi<b>^2$

incoherent scattering $\sigma_{incoh} = 4\pi(<b^2>-<b>^2)$

The coherent scattering is the scattering the same system would give if all the scattering lengths were equal to b. The incoherent term must be added to obtain the

scattering due to the actual system. Physically, the incoherent scattering arises from the random distribution of the deviations of the scattering lengths from their mean value.

To date we are unable to either calculate or predict the values of the scattering length, b. As a result, we have to treat the scattering lengths as parameters to be determined experimentally. Nevertheless, it is found that the scattering length, in general, depends on two factors. Firstly, there is a contribution to the scattering length proportional to $A^{1/3}$, where A is the mass number of the nucleus. Secondly, there may be "resonance scattering" depending on the nuclear energy levels of the compound nucleus composed of the initial nucleus and the neutron. The energies of such levels will depend on the details of the nuclear structure so that this resonance effect will vary widely from element to element, and indeed from isotope to isotope (B66). The result is that the overall scattering varies considerably through the periodic table. Fig(2.1) summarizes some of these variations, the linear variation of the scattering amplitudes for X-rays is also indicated (B75).

It should be noticed that although the random variations from element to element are substantial for neutrons, nevertheless the magnitude of the overall variation is comparatively small. The average taken over all the elements and isotopes which have been measured is about 0.6 barn (B66). This proves to be of great advantage as chemists often need to distinguish between elements with consecutive atomic numbers, such as between Al and Si in zeolites or close-neighbor transition metals in alloys. This also allows the detection of light elements in the presence of very heavy elements, for

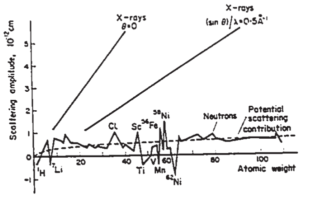

Fig(2.1) The variation of the neutron and X-ray scattering powers across the periodic table (Ref B66).

instance, oxygen (b=0.58 barn) can be detected in the presence of very heavy elements such as tungsten (b=.48 barn) and lead (b=.94 barn). This would not be easily done by using X-rays.

I.2- Bragg Scattering from a Crystal Lattice:

A perfect crystal may be constructed by repeating a unit cell periodically in space. The unit cell is defined in terms of three basis vectors a_1, a_2, a_3 and has a volume

$$V_0 = a_1 \cdot (a_2 \times a_3) \qquad \textbf{(2.15)}$$

the crystal is therefore described by lattice vectors t

$$t = l_1 \cdot a_1 + l_2 \cdot a_2 + l_3 \cdot a_3 \qquad \textbf{(2.16)}$$

where l_1, l_2, and l_3 are integers.

The content of the unit cell is composed of atoms which are at the end of the vectors ρ leading from the origin of the unit cell to the atom

$$\rho = \rho_1 a_1 + \rho_2 a_2 + \rho_3 a_3 \qquad \textbf{(2.17)}$$

The vector ρ defines the atomic coordinates in a unit cell. Its components are measured in fractions of the unit cell constants a_i's : $0 \le \rho \le 1$.

An atom in a crystal is therefore completely described by

$$R_{t,\rho} = t + \rho \qquad \textbf{(2.18)}$$

For the interpretation of diffraction experiments it is useful to construct a so called reciprocal lattice spanned by reciprocal lattice vectors g where

$$\begin{aligned} g_1 &= \frac{2\pi}{V_o}[a_2 \times a_3] \\ g_2 &= \frac{2\pi}{V_o}[a_3 \times a_1] \\ g_3 &= \frac{2\pi}{V_o}[a_1 \times a_2] \end{aligned} \qquad \textbf{(2.19)}$$

The volume of the unit cell in the reciprocal lattice is

$$g_1 \cdot [g_2 \times g_3] = \frac{(2\pi)^3}{V_o} \qquad (2.20)$$

The reciprocal space vectors are related to those of the real space by the relation

$a_i . g_j = 2\pi\, \delta_{ij}$ where δ_{ij} is the Kronecker delta

We now consider the scattering from a crystal in which the atoms lie in a regular three dimensional array. The atomic position vector is given in equation (2.18). The scattering amplitude, *b*, varies from one atomic species to another in the unit cell, and the cross section is therefore

$$\frac{d\sigma}{d\Omega} = \left| \sum_R b_R\, e^{iQ.R} \right|^2 \qquad (2.21)$$

$$= \left| \sum_t e^{iQ.t} \sum_p b_p\, e^{iQ.p} \right|^2 \qquad (2.22)$$

$$= \left| \sum_t e^{iQ.t} \right|^2 \times \left| \sum_p b_p e^{iQ.p} \right|^2 \qquad (2.23)$$

When the scattering vector, *Q*, is equal to zero, or to any reciprocal lattice vector, *g*, the sum over *t* adds up in phase and the right hand side is large. If we move away from a reciprocal lattice vector the terms rapidly come out of phase and the sum drops to a negligible value. The first part of equation (2.23) therefore becomes (W72),

$$\left| \sum_t e^{iQ.t} \right|^2 = \sum_g \delta\,(Q-g) \times constant \qquad (2.24)$$

The constant follows to be $N.(2\pi)^3/V_o$, where N is the number of unit cells and V_o is the unit cell volume (W72). Owing to instrumental resolution and mosaic spread in the crystal, the δ-function is spread out into a peak with a finite width.

Therefore, the cross section becomes

$$\frac{d\sigma}{d\Omega} = N_o \frac{(2\pi)^3}{V_o} \cdot |F_g|^2 \cdot \sum_i \delta\,(Q-g) \qquad (2.25)$$

where

$$F_g = \sum_p b_p e^{ig.p} \qquad (2.26)$$

is known as the structure factor.

The δ-function implies that the scattering occurs only when

$$Q = k - \acute{k} = g \qquad (2.27)$$

This expression is another way of writing Bragg's law. This equation can be best illustrated by a diagram in the reciprocal space. Fig(2.2) shows a reciprocal lattice with the origin at *O*. *OA* represents the wavevector of the incident neutrons, and *AB* that of the scattered neutrons. In general the point *B* does not coincide with a reciprocal lattice point, and there is no coherent scattering. But for special orientations of *Q* with respect to the crystal lattice, and for special scattering angles *θ*, *B* can coincide with a reciprocal lattice point. Coherent scattering then occurs. *OAB* is an isosceles triangle with *BO=g*.

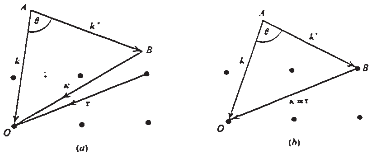

Fig(2.2) Bragg's law in reciprocal space (Ref S78).

Thus

$$g = 2k\sin\theta \qquad (2.28)$$

The vector *g* is perpendicular to a set of crystal planes. Its magnitude is

$$g = n\frac{2\pi}{d} \qquad (2.29)$$

where *d* is the spacing of the planes, and *n* is an integer. Also

$$k = \frac{2\pi}{\lambda} \qquad (2.30)$$

Substituting these relations in equation (2.28) gives

$$n\lambda = 2d\sin\theta \qquad (2.31)$$

which is the familiar form of the Bragg's law.

In order to observe a Bragg reflection, two conditions must be satisfied. First, the length of the scattering vector *Q* must satisfy the Bragg equation. This means that the detector must be set at the correct scattering angle 2*θ* giving *Q=g=2k sinθ*. Second, the direction of the normal to the reflecting planes must be parallel to the vector *Q*.

The simplest way to achieve this is to use a powder sample, which always contains few crystallites of the required orientation. In the classical neutron diffractometer, λ is fixed and the diffraction pattern is measured as a function of angle. The scattering, at a fixed *k*, comes out in cones called Debye-Scherrer cones, and these are successively crossed by the detector as the scattering angle increases, to give a sequence of Debye-Scherrer lines. An alternative procedure for recording the neutron powder pattern of a sample is to keep 2*θ* fixed and to satisfy the Bragg equation by varying *k*, or λ. This method is known as the time of flight, or simply TOF, method. It involves the measurement of the diffraction intensity as a function of λ. λ is readily determined from the flight-time for neutrons passing from the sample to the detector.

Once the diffraction pattern has been obtained, a great deal of information can be extracted. The size and the shape of the unit cell may be deduced from the values of the scattering angle, *θ*, at which Bragg reflections are observed. There are only seven distinct crystal systems to which a unit cell can belong. The seven crystal systems, each represented by a parallelepiped, are described by the relationship between the lengths of the three axes *a, b, c* and by the values of the three angles between the axes α, β, γ. The relationship between the interplanar spacings, *d*, and the lattice parameters is well known for each crystal system (W70). However, to fit the lattice parameters one must assign Miller indices to all observed reflections and this requires that one must make some intuitive guesses to which crystal system the material belongs.

The best choice of the unit cell is not necessarily a primitive one; sometimes a non-primitive cell has a more obvious connection to the point symmetry elements. Bravais has shown that there are only 14 distinct space lattices, of which seven are primitive and the other seven are nonprimitive.

A crystal structure is defined by its Bravais lattice and by the arrangement of the atoms in the unit cell. Information about the arrangement of atoms is obtained from the relative intensities of the Bragg peaks.

The structure factor, F_g, in equation (2.26) can be rewritten as

$$F_g = \sum_p b_p \, e^{2\pi i (hg_1 + kg_2 + lg_3) \, . \, (x.e_1 + y.e_2 + z.e_3)} \qquad (2.32)$$

where the indices *h,k,l* are the " Miller indices" of the reflecting planes in the crystal, and *x,y,z* are the fractional atomic coordinates of the atoms in the unit cell, and where the sum is extended to the atoms in the unit cell. Using the definition of the primitive unit cell vectors, g_1, g_2, g_3, this expression can be reduced to

$$F_{hkl} = \sum_p b_p \, e^{2\pi i (hx + ky + lz)} \qquad (2.33)$$

The Miller indices of the reflecting plane are used as a subscript instead of *g*. In the calculation of F_{hkl} it was assumed that the atoms in the crystal are tightly bound and not free to move. However, in reality the atoms are subject to thermal vibrations about their equilibrium positions and this motion has the effect of diminishing the amplitude of the coherent scattering. The structure factor then becomes

$$F_{hkl} = \sum_{j=1}^{n} b_j \, e^{2\pi i (hx_j + ky_j + lz_j)} \, . \, e^{(-B_j \sin^2\theta/\lambda^2)} \qquad (2.34)$$

where the summation is over the *j* atoms in the unit cell, and B_j is the temperature factor.

It would be possible to determine the positions of the atoms in the unit cell if the structure factors of a large number of reflections were known.

The great drawback of the powder method is that for samples of low symmetry, reflections at high angles suffer severe overlapping. Many symmetry-independent vectors, *g*, contribute to the observed intensity, and individual determinations of $| F_{hkl} |^2$ are possible only for the few reflections that are free from overlapping. The advent of the Rietveld method, section III of this chapter, revolutionized the powder diffraction technique. It made it possible to retrieve some of the information lost because of the peak overlapping.

II- Magnetic Neutron Scattering

One of the main applications of neutron diffraction comes from the fact that the neutron has a magnetic moment and can interact with atomic magnetic moments. In particular, when a crystal containing paramagnetic atoms becomes magnetically ordered (ferro-, ferri-, or antiferromagnetic), neutrons are sensitive to a double lattice: the lattice of the nuclei and the lattice of the magnetic moments. In this section, we first derive an expression for the scattering cross section due to the magnetic interaction of the neutron and the electron and then describe how this result could be used in determining the magnetic structure, *i.e.* the arrangement of the magnetic moments in the ordered state.

II.1 Cross section for the magnetic scattering:

In evaluating the total cross section we need to derive an expression for the potential due to the magnetic interaction between the neutron and the electron and then insert it in the master formula for the cross section. Although a rigorous treatment of the evaluation of the cross section is beyond the scope of this thesis, an expression for the magnetic cross section will be derived. A number of excellent books and reviews are in existence (S78), (R87) (P86) (S72) which provide a thorough discussion of the subject.

The operator corresponding to the magnetic dipole moment of the neutron is

$$\hat{\mu}_n = - \gamma \, \mu_N \, \sigma \qquad (2.35)$$

where

$$\mu_N = \frac{e\hbar}{2 m_p} \qquad (2.36)$$

is the nuclear magneton, m_p is the mass of the proton and *e* is its charge. γ is the gyromagnetic ratio of the neutron and its value is = 1.913 nuclear magnetons, and σ is the Pauli spin operator for the neutron (σ = 2s). The operator corresponding to the magnetic dipole moment of the electron is

$$\hat{\mu}_e = -2 \, \mu_B \, \hat{S} \qquad (2.37)$$

where

$$\mu_B = \frac{e\hbar}{2 m_e} \qquad (2.38)$$

is the Bohr magneton, m_e is the mass of the electron. *S* is the spin angular momentum operator for the electron in units of $\hbar$. The eigenvalues of its components are $\pm 1/2$.

We now consider the potential of the interaction of a neutron in spin state σ with a moving electron of momentum *P* and spin *S*

$$V_m(r) = - \mu_N . H \qquad (2.39)$$

The magnetic field, H, is due to the contribution of the magnetic dipole (spin part) and the momentum of the electrons that leads to a current (orbital part). This field for an electron moving with velocity v_e is (R87)

$$H = curl\left(\frac{\mu_e \times R}{|R|^3}\right) + \frac{-e}{c} \cdot \frac{\upsilon_e \times R}{|R|^3} \tag{2.40}$$

where R is the distance from the electron to the neutron.

Now this expression of the potential can be substituted in the master formula of the cross section

$$\frac{d\sigma}{d\Omega} = \left(\frac{m}{2\pi\hbar^2}\right)^2 |\langle k'\sigma' \mid V_m \mid k\sigma \rangle| \tag{2.41}$$

where k, the wave number and σ, the Pauli spin (= 2s, s is neutron spin) characterize the incident neutrons whereas the scattered neutrons are characterized by k' and σ'. This is a cross section for a process in which the neutron changes from the state k, σ to the state k', σ'. V_m is the potential between the neutron and all the electrons in the scattering system, equation (2.39). After integrating over the space coordinates r of the neutron we obtain the following expression for the potential

$$\langle k'\sigma' \mid V_m \mid k\sigma \rangle = 4\pi\, a_\perp(Q) \tag{2.42}$$

where $a_\perp$ is the interaction operator which can be expressed as (P86)

$$a_\perp(Q) = p.\sigma D_\perp = p.\sigma \sum_i e^{i(Q.r_i)}\left(\hat{Q} \times (\hat{S}_i \times \hat{Q}) + \frac{i}{(\hbar Q)}(\hat{P}_i \times \hat{Q})\right) \tag{2.43}$$

$D_\perp(Q)$ is the Fourier transform of the magnetic interaction vector and is composed of two parts, the first one containing S_i, the spin operator, and the second one

with P_i, the orbital angular momentum operator. For the constants we can write the relation (R87)

$$\left(\frac{m}{2\pi\hbar^2}\right) \cdot \gamma \cdot \mu_N \cdot \mu_B \cdot 4\pi = \frac{\gamma e^2}{2m_e c^2} = 0.2696\times10^{-12}\ cm$$

These constants define the magnitude of the interaction. The value 0.27×10^{-12} cm represents the scattering magnitude at $Q=0$ for a single magnetic moment of 1 μ_B. It has almost the same order of magnitude as the nuclear scattering length b, varying from about $0.2\text{-}1.2\times10^{-12}$ cm. Therefore the nuclear and magnetic scattering intensities are of comparable magnitudes.

In many cases of interest the total orbital angular momentum of the transition metal ions is either zero or quenched by the crystal field. Under these circumstances, $D_\perp(Q)$ could be approximated by the spin part of the total angular momentum. This leads to the expression

$$\sum_i e^{(iQ.r_i)} \cdot \left(\hat{Q} \times (\hat{S}_i \times \hat{Q})\right) = \hat{Q} \times \left(\sum_i 2s_i\, e^{iQ.r_i}\right) \times \hat{Q} \tag{2.44}$$

Thus this term is the magnetization component $M_\perp(Q)$ perpendicular to the scattering vector Q, and

$$D_\perp(Q) = p\sigma \,.\, M_\perp(Q) \tag{2.45}$$

The magnetic scattering operator is then related to the Fourier transform of the total magnetization component perpendicular to the scattering vector. This angular dependence

of the scattering amplitude gives the possibility of determining both the amplitude and the orientation of the magnetic moment. However, it is more useful to define a so-called magnetic form factor. Hence,

$$D_\perp(Q) = p\, f(Q)\, \mu_\perp \cdot \sigma \tag{2.46}$$

The term $f(Q)$ is the form factor of the magnetic ion, with $f(Q=0) = 1$. The form factor appears because the spatial distribution of magnetic electrons about the ion center is comparable to the interatomic spacing and thus to the neutron wavelength used in the scattering. Unlike the nuclear scattering length, b, however, the magnetic form factor can often be calculated quite accurately from the electronic wavefunctions.

However, when the polarization of the neutron beam is not taken into account, the cross section is the sum of the nuclear and magnetic part. The magnetic part of the cross section is given by

$$\frac{d\sigma_M}{d\Omega} = p^2 f^2(Q) \langle \mu_\perp^2 \rangle \tag{2.47}$$

where

$$\langle \mu_\perp \rangle = g^2 S(S+1) \tag{2.48}$$

This equation represents the magnetic scattering by a paramagnetic ion. In a paramagnetic material the directions of the magnetic moments vary randomly from atom to atom and there is no magnetic contribution to the Bragg diffraction peaks. The

magnetic scattering is distributed in the background of the diffraction pattern, falling off with increase of the angle θ because of the influence of the form factor $f(Q)$.

For materials whose magnetic moments are in fixed orientation, *i.e.* when the moments are ordered, for instance, parallel or antiparallel, the magnetic cross section is replaced by

$$\frac{d\sigma_M}{d\Omega} = p^2 q^2 \mu^2 f^2(Q) \tag{2.49}$$

where q is the magnetic interaction vector defined by

$$q = \hat{\varepsilon}\,(\hat{\varepsilon} \,.\, \hat{K}) - \hat{K} \tag{2.50}$$

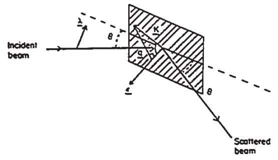

Fig(2.3) The relationship between the scattering unit vector and the magnetic unit vector (Ref B75).

where K is a unit vector in the direction of the atomic magnetic spin and ϵ is a unit vector in the direction perpendicular to the effective reflecting planes, *i.e.* the so-called scattering vector. From the definition of q, Fig(2.3) it follows that the q lies in the plane of ϵ and K and is perpendicular to ϵ and of magnitude $sin\alpha$. Thus

$$|q| = sin\alpha \tag{2.51}$$

It is worth emphasizing that K is the direction of the spins in the magnetic materials. The existence of defined orientations for the magnetic moments of the ions means that there is coherence between the neutrons scattered by the various atoms.

Let us consider a magnetically ordered lattice. We have to extend this expression to include a summation over ρ for the whole unit cell. The basic innovation is the introduction of the "magnetic unit cell structure factor" $F_M(Q)$, which is defined by

$$F_M(Q) = pq \sum_\rho \mu_j \cdot f_\rho(Q) \cdot e^{i(Q \cdot \rho)} \tag{2.52}$$

and the magnetic cross section in equation (2.49) can be written as

$$\frac{d\sigma_M}{d\Omega} = N\frac{(2\pi)^3}{V_0} \sum_g \sum_k \mid F_{M\perp}(Q) \mid^2 \delta(Q-k-g) \tag{2.53}$$

This will give superlattice reflections, each of these being located in the reciprocal point defined by the scattering vector Q=g+k.

The determination of magnetic structures tends to be very much a trial and error process. In practice, there are three essential steps required to solve a magnetic structure from powder data.

1- identification of the wave vector k.

2- the knowledge of the magnetic moment directions, and

3- the evaluation of the moment values.

The first step involves determining the propagation vector k which describes the periodicity of the magnetic lattice. This is done by determining the magnetic peak positions and then try to find a wave vector k that interprets these peak positions. This is usually done by inspection, which is very often a trivial task since the chemical cell is already known. However, in some cases it is not so easy and thus it can be the most difficult part of the magnetic structure determination (R87). The value of k can range from (0,0,0) as in the case when chemical and magnetic unit cells are identical, to some simple fractional value of a reciprocal lattice vector such as (½,½,0) in which case the magnetic cell is obtained by doubling the chemical cell along the a and b axes while the c axis is identical for both cells. In some cases the k vector is so complicated that it is best to represent the magnetic cell as incommensurate with the chemical cell.

The second and third steps involve fitting the observed intensity data to those calculated for various possible models, *i.e.* different possible spin orientations on a trial and error basis. The choice of these models is frequently made on an intuitive and rather arbitrary basis. However, it is possible to go about this more systematically in several

ways. The first of these involves microscopic methods, in which one makes some simple assumptions about the magnetic coupling between neighboring moments and tries to deduce which particular structures can occur. Microscopic methods have been used with varying degrees of success, but in general tend to suffer from the fact that where materials of moderate complexity are concerned it is very difficult to know which interactions can or can not be ignored.

Another approach which was developed by Bertaut (B67) is based on group theory. It involves the investigation of the transformation properties of the structure under the operations of the crystallographic group in the ordered state in order to find appropriate irreducible representations which are able to describe the magnetic structure and its transformation properties. For a detailed description of this method the reader is referred to Bertaut's original paper, ref (B68). Of course, if there are only one or two magnetic atoms in the unit cell, the magnetic structure can be solved without making use of the group theory. However, for a large number of magnetic atoms in the unit cell, group theory can be extremely useful in enumerating the possible magnetic structures compatible with the crystal symmetry. The third procedure involves the use of the magnetic space groups. For a more detailed discussion on this subject the interested reader is referred to a readable and lucid review by Cox (C72).

III- The Rietveld Method

As noted earlier, there are serious difficulties in obtaining reasonable structural information from powders. Most of these problems arise because of the fact that the three dimensional intensity data are mapped into one dimension in the powder experiment. This results in peak overlap, which is often severe. The traditional approach to the refinement of powder data, *i.e.* pre-1969, has been to reduce the pattern to a set of integrated intensities and then to $\Sigma|F_{hkl}|^2$ values, where Σ denotes a summation for overlapping reflections. For structures of low symmetry, the overlapping soon becomes severe and refinement by this method becomes impractical.

Rietveld (R67)(R69) introduced the profile refinement method which is capable of retrieving some of the lost information due to the overlapping. This method revolutionized powder diffraction as a tool for refinement of crystal structures and it has been widely used since.

The Rietveld method is now recognized to be uniquely valuable for structural analysis of nearly all crystalline materials not available as single crystals. It has played a crucial role in the elucidation of the new high temperature superconductor structures. Structural studies of heavy metal oxides and of zeolites, clays, minerals, and magnetic materials are representative of the thousands of important applications of the Rietveld method and attest to its vital importance to today's solid state science. A number of excellent reviews of the method are in existence (C77.2) (A82) (Y93). Ref(Y93) would serve as the most comprehensive reference for the technique and its applications to which the interested readers are referred.

In general, the Rietveld method fits the structural parameters to the overall profile of the powder pattern, assuming the pattern to be the sum of a number of Bragg reflections of well-defined peak shapes centered at their respective Bragg angle positions. The data are not artificially compressed as in the conventional method, and the actual point intensity counts are used as the least squares data input. This is a more natural representation of the available intensity data, and leads to a greater efficiency of information retrieval from the superposed reflections in the pattern.

The Rietveld program minimizes the quantity

$$M = \sum_i w_i \left[\, Y_i(obs) - Y_i(cal) \,\right]^2 \qquad (2.54)$$

where Y_i is the background-corrected intensity at a 2θ point i, w_i is a least squares weight based on the counting statistics and equal to:

$$w_i = \frac{1}{y_i} \qquad (2.55)$$

$Y_i(cal)$ is the calculated intensity which is obtained by evaluating equation (2.56)

$$Y_i(cal) = b(2\theta_i) + \sum_{k=k_1}^{k_2} I_k\, G(2\theta_i - 2\theta_k) \qquad (2.56)$$

where

$b(2\theta_i)$ is the background at point i, which is usually a relatively smooth function that varies much less rapidly with $2\theta_i$ than the diffraction pattern does.

I_k is the integrated intensity of the k^{th} Bragg reflection and is the product of many factors as in equation (2.57)

$$I = L_k \,.\, P_k \,.\, A \,.\, |F_k|^2 \qquad (2.57)$$

where

L_k contains the Lorentz, polarization when appropriate, and multiplicity factors.

P_k is the preferred orientation function. Preferred orientation arises when there is a stronger tendency for the crystallites in a specimen to be oriented more one way, or one set of ways, than all others. Because this produces systematic distortions of the reflection intensities, the distortions can be mathematically modelled with P_k. Rietveld implemented equation (2.58) as a preferred orientation function (R69),

$$P_k = e^{(-G_1 \alpha_k^2)} \qquad (2.58)$$

where G_1 is a variable parameter and α_k is the angle between d_k and the fibre axis direction.

A is an absorption factor. This is normally very small for neutron diffraction, and is usually neglected.

F_k is the structure factor for the k^{th} Bragg reflection which was defined in the previous sections

$$F_k = \sum_j N_j f_j\, e^{2\pi i(hx_j + ky_j + lz_j)} \,.\, e^{-B_j} \qquad (2.59)$$

where N_j is the site occupancy multiplier for the j^{th} atom site, f_j is the scattering factor for j^{th} atom. f_j is equal to b for the nuclear scattering, equation (2.5), and p for the magnetic scattering, equation (2.43). Since the contribution of nuclear and magnetic scattering to the Bragg reflection intensity is additive, the structure factor could be rewritten as

$$F_k = N_j \left[\sum_j b_j e^{2\pi i(hx_j + ky_j + lz_j)} + \sum_j q_j p_j e^{2\pi i(hx_j + ky_j + lz_j)} \right] . \, e^{-B_j} \qquad (2.60)$$

where B is the temperature factor of the j^{th} atom, and q was defined in equation (2.50).

$G(2\theta)$ is a peak shape function, normalized so that the sum over the range of a Bragg peak is one, and the sum is over all Bragg reflections that can contribute to point i.

Each of the different experimental techniques for collecting data has its own most appropriate peakshape (Y93). The peak shapes tend to be the convolution of multiple resolution functions due to different contributions. For a constant wavelength neutron diffractometer, the line shape is adequately represented by a Gaussian peak, equation (2.61).

$$G(2\theta) = \frac{\sqrt{c}}{H_k\sqrt{\pi}}\, e^{-\frac{c(2\theta_i - 2\theta_k)^2}{H_k^2}} \qquad (2.61)$$

So $Y_i(cal)$ is formed by summing the contributions from all Bragg reflections which overlap at point i, with these contributions dropping to zero when $(2\theta_i - 2\theta_k)$ is greater than 1.5 H_k. H_k is the full-width at half maximum, FWHM, of the Bragg reflection k being considered. As in equation (2.62), the variation of H_k^2 with angle can be represented by a three-term power series in $\tan\theta$ (C58)

$$H^2 = U \tan^2\theta_k + V \tan\theta_k + W \qquad (2.62)$$

Other complicated line shape functions were implemented in the case of the TOF method and X-ray diffraction, some of these functions are provided by Young in reference (Y93). One should notice that it is a crucial feature of the Rietveld method that no effort is made in advance to allocate observed intensity to a particular Bragg reflection nor to resolve overlapped reflections. Consequently *a reasonably good starting model is needed. It should be emphasized that the method is a structure refinement rather than a structure solution method.*

III.2- Criteria of Fit:

When a refinement has converged to a stable minimum, the crystallographer must then confront several questions (P91):

1- Is the current model an adequate fit to the data?

2- Is the model complete, or would additional parameters improve it?

3- Is the model, as refined, plausible in terms of physics and chemistry?

The first criterion for addressing the first question is a residual plot, a plot of the differences between observed and calculated intensities at each point. It should not contain any peaks that are not attributed to the phase being studied, and it should be reasonably free of oscillations in the tails of strong peaks that would indicate an inadequate peak shape function.

If the appearance of the residual plot is satisfactory, some statistical tests may be applied. Borrowing a page from the single crystal crystallographers and adapting it to their needs, the users of the Rietveld method have developed several R-values that are now commonly used, TABLE(2.1). From a purely mathematical point of view, R_{wp} is the most meaningful of these R's because the numerator is the residual being minimized.

The ultimate criterion of fit must always be the chemist's scientific judgement. The structure must make sense!. Bond distances and angles that deviate wildly from those that are commonly observed must always be viewed with suspicion, no matter what statistical tests may indicate. A low standard deviation for a parameter is necessary, but not sufficient condition for an accurate structure.

The most often cited indicator of precision in Rietveld refinement is the estimated standard deviation (e.s.d). It is important to note that the e.s.d is not the experimental probable error, it is the minimum possible probable error arising from random errors alone.

TABLE(2.1)
Some numerical criteria of fit

$$R_F = \frac{\sum |I_K(obs)^{1/2} - I_K(cal)^{1/2}|}{\sum |I_K(obs)^{1/2}|}$$

$$R_B = \frac{\sum |I_K(obs) - I_K(cal)|}{\sum I_K(obs)}$$

$$R_p = \frac{\sum |Y_i(obs) - Y_i(cal)|}{\sum Y_i(obs)}$$

$$R_{wp} = \left[\frac{\sum w_i\left(Y_i(obs) - Y_i(cal)\right)^2}{\sum w_i\left(Y_i(obs)\right)^2}\right]^2$$

$$R_{exp} = \left[\frac{(N-P)}{\sum w_i Y_i(obs)}\right]^{1/2}$$

Chapter 3

Experimental

In this chapter, the preparation of two classes of oxides, namely $CuSb_2O_6$ and $A^{2+}As_2O_6$, where A^{2+} is Co, Mn, Ni, or Fe, is described. The measurements of the magnetic susceptibility and the neutron diffraction are described as well.

I- Sample Preparations:

1.1- $CuSb_2O_6$:

Copper antimonate was prepared by the reaction of CuO (Johnson-Matthey) and Sb_2O_3 (Baker) in air at 1000° C in an alumina boat for 24 hours. In order to minimize volatilization of Sb_2O_3 the reactants were heated at a rate of 4° C/min. The yellow color of the product is consistent with the previous reports (S82).

$$Sb_2O_3 + CuO \xrightarrow{\qquad\qquad} CuSb_2O_6 \qquad (3.1)$$

The purity of the product was very dependent on the pressure used for the pelletization. Pressures higher than 2×10^4 psi resulted in the formation of another phase on the pellet surface which was identified as $Cu_4SbO_{4.5}$ (S82).

Based on differential thermal analysis, DTA, measurements, Fig(3.1), the formation of $CuSb_2O_6$ apparently involves three steps. The first step (380-500° C)

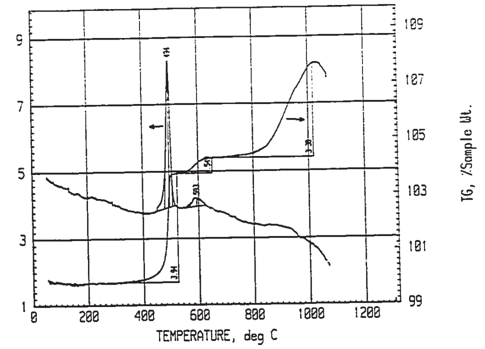

Fig(3.1) The DTA results of the reaction of CuO + Sb_2O_3.

represents the oxidation of Sb_2O_3 to Sb_2O_4. the second and third steps (500-1000° C) involve further oxidation of antimony to Sb^{5+} and the formation of $CuSb_2O_6$.

The completion of the reaction was verified by X-ray powder diffraction data which were collected on a Nicolet I2 diffractometer.

Neutron diffraction data were collected at room temperature on the General Purpose Powder Diffractometer (GPPD) at the Intense Pulsed Neutron Source (IPNS) at

Argonne National Laboratory[2]. A general discussion of the TOF, time of flight, method regarding operation principles, peak shape and background analysis methods, and specific information on the GPPD at IPNS has been published by McEwen *et al* (M83)

Data were collected from the $2\theta=148°$, 90°, and 60° detector banks, but only the data collected from ($2\theta = 148°$) were used in the refinement so as to achieve the highest possible resolution. Data preparation and least squares refinement were carried out using the programs of the IPNS Rietveld analysis package for TOF data from spallation or pulsed neutron sources.

Low temperature neutron data were collected on the Dualspec spectrometer at Chalk River Labs. Data sets were collected at temperatures of 5, 7, 10,and 12 K at wavelength 1.4999 Å.

Magnetic susceptibility data were collected on a Quantum Design SQUID magnetometer using a pressed polycrystalline pellet. Magnetic susceptibility was measured as a function of temperature and as a function of field. Description of the instrument and the data collection procedures will be dealt with later in the chapter.

Numerous attempts were directed at growing large single crystals. The flux method was the method of choice for this system due in part to its simplicity. It was reported that small single crystals of $CuSb_2O_6$ were grown from V_2O_5 flux (S85). These crystals were very small and have an irregular crystal habit. We succeeded in growing larger crystals by modifying the flux composition and the cooling rates. Small amounts of some additives were used. The additive with the most pronounced effect on both the crystal size and habit was boron oxide, B_2O_3. Of the various compositions attempted, the flux with the composition (V_2O_5 75% + B_2O_3 5% + $CuSb_2O_6$ 20%) provided the best results. A charge of 5 grams of this composition was loaded into a quartz tube, of the dimensions 10 mm × 12 mm and 1mm thickness. After evacuation to 10^{-3} torr, the tube was sealed off. This mixture was soaked for 20 hours at 1000° C, then cooled at a rate of 5° C/hr to 600° C. After the temperature of the furnace reached 600° C the furnace was cooled at a rate of 1° C/min. A large number of crystals with well developed faces were obtained, from which a crystal of the dimensions 3 mm × 2 mm × .5 mm weighing 2.71 mg with well developed faces was selected for use in the magnetic measurements. It was revealed from the elemental analysis that some V^{5+} was incorporated in these crystals. Based on the neutron activation analysis, the V^{5+} content was found to be 0.48(3)%. The crystal was oriented with the help of an optical goniometer. Magnetic susceptibility was measured as a function of field (0 - 5 Tesla), at temperatures below and above the T_c, *i.e.* 5 K and 15 K.

---

[2] The neutron diffraction data were collected by Dr. Yun, H.

1.2- $A^{2+}As_2O_6$:

The preparation of these oxides was much more difficult and tedious than that of $CuSb_2O_6$. Our efforts were directed at the synthesis of the arsenates of the transition metals Ni^{2+}, Co^{2+}, Mn^{2+}, and Fe^{2+}. Of these arsenates, only $NiAs_2O_6$ and $CoAs_2O_6$ were reported in the literature (M41) (T58). Previously reported preparations were carried out in air and at relatively low temperatures, 450 C, for 50 hours. These reactions, we believe, may not give a single phase product. In the course of the present preparations, the reactions were carried out in sealed quartz tubes and the reaction times were prolonged to a week and at higher temperatures.

An admixture of 1:1 molar ratios of the metal oxide, $M^{2+}O$, and the arsenic pentoxide, As_2O_5, were heated in sealed quartz tubes at 650-750° C for one week. The preparations are carried out according to the following reactions:

$NiO + As_2O_5 \longrightarrow NiAs_2O_6$ yellow (3.2)

$CoO + As_2O_5 \longrightarrow CoAs_2O_6$ purple (3.3)

$MnO + As_2O_5 \longrightarrow MnAs_2O_6$ pinkish white (3.4)

Due to its high toxicity and high hygroscopicity, the arsenic pentoxide was handled with the utmost care.

The moisture content of the pentoxide was determined by the use of thermogravimetric analysis, TGA, for every preparation. This was necessary in order to exactly determine the moisture content, which, typically, was found to be in the range 14-20 % wt. A typical TGA output is plotted in Fig(3.2).

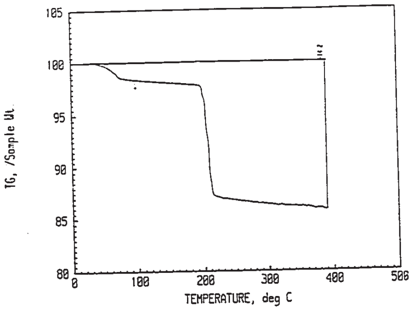

Fig(3.2) TGA results of the dehydration of As_2O_5.

A careful drying procedure was necessary for these preparations to be successful. It was necessary that all the weighing and mixing were to be done in the dry box, the mixture then was pressed into pellets and transferred as quickly as possible to a quartz tube which then dried under vacuum as follows: the mixture of MO and As_2O_5 was heated for 24 hours at 100° C and at 200° C for 30 to 40 hours depending on the moisture content. The dehydration of the pentoxide can be represented by the following chemical reaction (W84),

$$As_2O_5.4H_2O \xrightarrow{\qquad} As_2O_5.5/3\ H_2O\ (H_5As_3O_{10}) \xrightarrow{\qquad} As_2O_5 \quad (3.5)$$

The tube is then sealed under 1×10^{-5} torr and soaked for one week at 650 - 750° C. The quartz tubes were protected by a ceramic tube during the firing. In the course of these preparations, severe attack of the quartz tubes was observed. *It is important to re-emphasize the fact that if the drying was not done properly, the quartz tubes exploded.*

NiO (AESAR) and As_2O_5 (AESAR) were heated to 700° C for one week. The yellow color of the product was consistent with that reported by Taylor (T58). It was verified by the use of the powder X-ray diffraction that the product was single phase. The reaction of CoO (ALFA Inorganics) and As_2O_5 (AESAR) yielded a purple product which was analyzed to be a single phase and of the composition $CoAs_2O_6$. The reaction mixture was heated at 650° C for 4 days.

The cell parameters were determined by the use of the Guinier camera (IRDAB XDC700) with Cu $K\alpha1$ radiation and a Si standard. The Guinier films were read with a computer-controlled automated LS-20 type line scanner (KEJ Instruments, Töby, Sweden). Using the output of the scanner, the cell parameters were refined using the LSUDF least squares program. These cell parameters were then used in the Rietveld refinement method.

In an effort to extend the study to other phases not reported in the literature, we tried to prepare the isostructural phases $MnAs_2O_6$ and $FeAs_2O_6$. Identical procedures were used in the case of the manganese arsenate where a mixture of MnO (AESAR) and As_2O_5

(AESAR) were heated to 700° C for one week. A pinkish white product was obtained. The powder X-ray pattern was very similar to that of the cobalt and nickel counterparts. The cell parameters were obtained from the analysis of the data obtained from the Guinier film. The cell parameters were determined by least squares fit of the scanned data from the Guinier film as well, the cell parameters of $CoAs_2O_6$ were used as a starting values.

In the case of iron arsenate, since stoichiometric FeO does not exist, the preparation was carried out as in reaction (3.6). In this reaction a mixture of Fe powder (Alfa) and iron oxide Fe_2O_3 (Baker) are mixed thoroughly with As_2O_5 (AESAR), the drying and evacuation procedure were done as outlined above.

$$(Fe + Fe_2O_3) + 3As_2O_5 \xrightarrow{\qquad ? \qquad} 3FeAs_2O_6 \quad (3.6)$$

A pale white powder was obtained after the mixture at the left side of the above equation was heated at 750° C for a week. The X-ray powder pattern of this product was very different from that of the AAs_2O_6 phases but resembled that of the $Fe_2As_4O_{12}$ (Y74) in which Fe is trivalent and As has a mixed valency (+3 and +5).

Single crystals of this phase were obtained by the following procedure: 1 gram of $Fe_2As_4O_{12}$ powder was loaded in a quartz tube with the dimensions 10mm × 12mm × 1mm thickness. The sample tube was evacuated to 10^{-2} torr, ½ atm of Cl_2 gas was then introduced and the tube was sealed off. The tube was soaked at 900° C for 10 hours and slowly cooled at a rate of 5° C/hour to 400°C. The subsequent cooling to room

temperature was done at a much higher rate. Large aggregates of white transparent single crystals were obtained. Elemental analysis was done on one of these aggregates by using EDXA to rule out the presence of any chlorine in the sample. A small sample was used to measure the X-ray pattern in the Guinier camera. A similar pattern was observed as that of the $Fe_2As_4O_{12}$.

II- Data Collection:

II.1- Neutron Diffraction:

Most of the neutron data were collected on the powder diffractometer at the McMaster Nuclear Reactor, MNR, with 1.3919 Å neutrons. The diffractometer is equipped with a position sensitive detector, PSD. MNR has a neutron flux in the central core of 1×10^{13} n cm^{-2} s^{-1}. The maximum beam size at specimen monochromator is 2 cm wide x 5 cm high, and the monochromator used was Cu(200) with an adjustable take-off angle which is usually set at 60° (G90). A sketch showing the main components of the diffractometer is shown in Fig(3.3).

The PSD detector was described in detail in reference (T84), but a brief description of the detection principle and the detector is introduced here. This will follow very closely the description given in reference (T84). The PSD detector consists of a 3-counter array of linear position-sensitive detectors. These counters were made of stainless steel cylindrical tubes. The gas fill of the counters is 8 atm of ^3He for neutron detection.

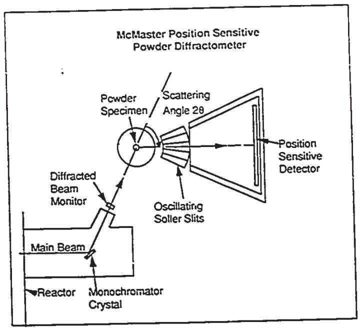

Fig(3.3) A sketch of the PSD diffractometer at MNR facilities (Ref G90).

detection principle is based on the nuclear reaction

$$^3He + {}^1n \longrightarrow {}^3H + {}^1p + .77\ MeV \qquad (3.7)$$

Another 4 atm of Argon gas are added for stopping reaction products (with 5% CO_2 gas for quenching). The anode wire is nickel chrome with a diameter of 0.015 mm, and an active detector length of 610 nm. The 3 counters are placed one above the other, so that the central counter has its axis in the horizontal plane of the spectrometer. The ends of each detector are connected to preamplifiers which are placed within a box mounted rigidly on the detector shielding. The power to these preamplifiers , a bias voltage (2150 V), and the output signals from each of the detectors are connected to the system electronic rack from this preamplifier box.

The position of a neutron capture event is determined by the charge division method. The charges at each end are amplified separately and compared digitally to determine the detection point along the length of the detector. The analog signal processing for each detector is provided by a single circuit board module which contains the main shaping amplifier and analog to digital converters (ADC) used for position encoding.

Data are collected in frames, each frame spans an angular range of 30°. A full data set usually composed of 5 frames covering a range of angles from about 10° to 120°. The required time of data acquisition was 6-8 hours each for the first three frames, and about 12 hours each for the last two frames. This set-up is equipped with a closed cycle cooling system and a temperature control which was capable of controlling the temperature of the sample in the range 7 - 300 (± 0.1) K.

The raw data collected on each frame are converted to an intensity pattern consisted of the total counts summed over all three detectors falling within 0.1° over the range of the scan. These intensity patterns are added together and normalized in the process of the addition, which then are merged together to form a single data set containing the whole range of the scan. The resulting data files were then used as the observed data files in the refinement programs.

The Rietveld refinement of the chemical structure was carried out on the DBWS refinement package (S91). This program was compiled on the MSF Fortran compiler which ran on DOS-PC. Those involving the magnetic structure refinement were handled by the RIETAN program which was developed by Dr. Izumi (I89). The program was compiled on a 6000 Fortran compiler in an IBM Unix network.

Data Collection:

Complete data sets, which consisted of 5 frames, were collected at room temperature for NiAs$_2$O$_6$, CoAs$_2$O$_6$, and MnAs$_2$O$_6$. A thin-walled vanadium can was used as a sample holder for room temperature data collection, whereas for the low temperature experiment an aluminum can was used instead. The sample holder for the low temperature experiment was sealed under a He gas atmosphere in a glove bag and an indium wire was used as a gasket.

Regarding the low temperature experiments, data frames were collected on the nickel arsenate sample at temperatures 8, 12, 15, 25, 30, and 35 K.

For the cobalt arsenate sample, the room temperature neutron diffraction pattern contained a few impurity peaks. In another preparation, the reaction was conducted at higher temperature and for a longer time. These impurity peaks disappeared. Low temperature data on the first batch were collected at 8, 12, 15, 17, 18, 19, and 19.5 K. Only two frames at 8 K were collected on the second batch.

For the MnAs$_2$O$_6$ sample, due to a malfunction in the cooling system at the MNR, low temperature neutron data were collected on the Dualspec spectrometer at the Chalk River nuclear reactor. Data were collected at 5, 7, 9, 12, and 15 K.

Low temperature neutron diffraction data were collected from the Fe$_2$As$_4$O$_{12}$ sample at 8, 15, 30, 40, 45, 50, and 57 K at MNR facilities.

II.2- Magnetic Susceptibility Measurements:

All magnetic susceptibility measurements were collected on a SQUID magnetometer. A SQUID is a magnetic flux measuring device that converts an unknown value of magnetic flux (or field) into a voltage that can be easily measured (K90.1). Physically, it is a loop of superconducting material that can range from few micrometers to a few millimeters in size. In the model used in this work, the coil configuration consists of three coils, connected in series, and wound in the ratio 1:2:1 turns. The central coil has 2N turns and is wound in the opposite direction to the outer coils. This configuration, known as the second derivative configuration, strongly rejects interferences from nearby magnetic sources. In measuring the magnetic moment, the sample is scanned through the coil (scanning length was set to 6 cm). During a scan, the sample is stopped 32 times, and at each stop, 10 measurements were collected. A voltage profile as a function of travel distance is obtained, from which the magnetic moment can be determined. The final result is the average of two such scans.

The magnetic moment calibration for the system is determined by measuring a Pd standard (3 mm diameter × 3 mm high) over a range of magnetic fields, and adjusting the system calibration factors to obtain the correct moment for the standard to an accuracy of about 0.1%.

The system is equipped with a temperature control module which is capable of providing an actively regulated, precision thermal environment over the entire range of operation, 2 - 400 K , and a superconducting magnetic field system which provides reversible field operation of ±5.5 Tesla. The SQUID detector system includes the model 2000 SQUID Amplifier control electronics, and a sensing pick up loop. The magnetometer also has a sample handling system which allows automatic sample measurements and position calibrations using a microstepping controller having a positioning resolution of 0.0003 cm.

In the course of the measurement, the magnetic moment of the sample is determined as a function of temperature in a fixed external field by what is known as the zero-field-cooled, ZFC, method. In this procedure, the sample is cooled in zero field to $T<T_c$, about 5 K, then the external field is applied, and the moment is measured as a function of temperature. The sequence of the measurements is programmed by the operator.

Chapter 4

$CuSb_2O_6$

I- Introduction:

Most of the transition metal antimonates of the composition ASb_2O_6 crystallize in the trirutile structure. The relative sizes of A^{2+}, Sb^{5+}, and O^{2-} must, of course, fit within the structure field appropriate to the rutile structure. For somewhat larger A^{2+} ions, other structure forms are adopted, for example, $MnSb_2O_6$ crystallizes in the Niobite structure (W84), and the $PbSb_2O_6$ structure is adopted if the radius of the A^{2+} ion is about 1Å or larger (W84). The trirutile structure is derived from the normal rutile structure by a tripling of the *c*-axis. The superlattice arises as a consequence of the ordering of the divalent and pentavalent cations where it seems that the difference of the three formal charge units is sufficient to cause the ionic ordering. The trirutile space group is the same as that for the normal rutile, $P4_2/mnm$, with Z=2. It has been reported that $CuSb_2O_6$ and $CrSb_2O_6$ crystallize in a distorted trirutile structure (B41). A diagram of the structure is shown in Fig(4.1).

$CuSb_2O_6$ crystallizes in a distorted monoclinic trirutile structure in the space group $P2_1/c$ or $P2_1/n$ which is a subgroup of the space group $P4_2/mmm$ (B41), but no detailed

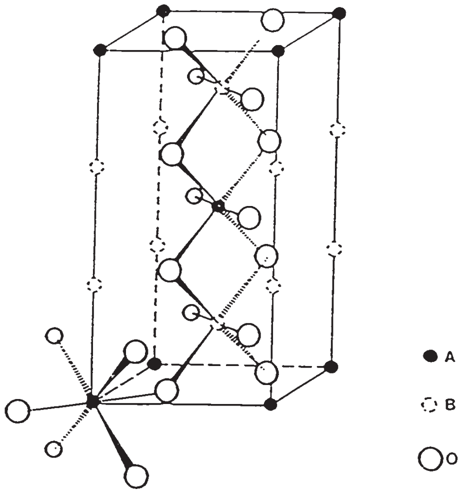

Fig(4.1) The triturile unit cell (Ref E84).

structure analysis has yet been reported.

The atomic positions were derived from the $ZnSb_2O_6$ tetragonal structure as in Table (4.1) in the space group $P2_1/n$, with the *b* axis being the unique axis

Table 4.1

The atomic coordinates of $CuSb_2O_6$ as derived from the $ZnSb_2O_6$ unit cell

Atom	Site	Coordinates			
Cu	*2a*	0	0	0	
Sb	*4e*	0	0	*z*	(*z*=1/3)
O1	*4e*	*x*	*x*	0	(*x*=.3)
O2	*4e*	*x*	*x*	*z*	(*x*=.3, *z*=1/3)
O3	*4e*	-*x*	-*x*	*z*	(*x*=.3, *z*=1/3)

II- Structure Data:

The structure of this compound was refined by the Rietveld refinement method using the time of flight, TOF, neutron diffraction data. The cell parameters and the atomic positions were taken from reference (B41) (*a*=4.62Å, *b*=4.62Å, *c*=9.28Å, *β*=88.5°). The final refinement in space group $P2_1/n$ included 2819 observations and 1442 independent reflections (0.53Å ≤d≥ 2.13Å). The 31 variables refined included a scale factor, cell parameters, positional parameters, isotropic thermal parameters, an

absorption parameter, and background and profile parameters. The final agreement indices are R_p = 5.0%, R_{wp} = 7.2%. The statistically expected weighted profile R_{exp} = 1.3%.

Details on the data collection and refinement results are listed in Table(4.2). The refined atomic parameters are given in Table(4.3) and selected bond lengths and angles are tabulated in Table (4.4). The refinement patterns of the four frames are plotted in Fig(4.2).

Both cations are octahedrally coordinated, each Cu^{2+} ion is coordinated by six oxygens in a distorted octahedral arrangement with two long axial bonds (Cu-O(3) 2.120(4) Å) and four shorter equatorial bonds (Cu-O(1) 2.004(4)Å, and Cu-O(2) 2.012(4)Å). This is a very common environment for Cu^{2+} ions in octahedral sites. This distortion is regarded as a consequence of the Jahn-Teller distortion which seems to be confined to d^9 configuration. This could explain why among all the trirutile compounds only $CuSb_2O_6$ and $CrSb_2O_6$ crystallize in the distorted monoclinic symmetry. The situation is analogous to that in CuF_2, where the normal rutile structure is monoclinically distorted (B57). The coordination around the Sb^{5+} ion is also somewhat distorted. All the bond lengths compare well with the sum of the ionic radii (S76).

The structure framework consists of a network of edge and corner sharing of CuO_6 and SbO_6 octahedra. As shown in Fig(4.3), the CuO_6 and SbO_6 octahedra share edges to form columns along the <001> direction and these columns connect through corners with each other to form the 3-dimensional structure.

Table 4.2

Summary of Intensity Collection and Rietveld Refinement Results from Neutron Data for $CuSb_2O_6$

a (Å)	4.6349(1)
b (Å)	4.6370(1)
c (Å)	9.2931(10)
β°	91.124(2)
V (Å^3)	199.69
Space Group	$P2_1/n$
T of data collection	298 K
Detector bank (2θ °)	148°
d-spacing, limiting (Å^{-1})	0.53-2.13
No. of observations	2819
No. of reflections	1442
No. of variables	31
R_p*	5.0%
R_{wp}*	7.2%
R_{exp}*	1.3%
R_B*	4.7%

* Weighted profile $R_{wp} = 100 \times \{[\Sigma w(Y_{obs} - Y_{cal})^2]/\Sigma w(Y_{obs})^2]\}^{1/2}$

profile $R_p = 100 \times \Sigma|Y_{obs} - Y_{cal}|/\Sigma Y_{obs}$; nuclear $R_n = 100 \times \Sigma|I_{obs} - I_{cal}|/\Sigma I_{obs}$;

expected $R_{exp} = 100 \times \{(N - P)/\Sigma w(Y_{obs})^2\}^{1/2}$

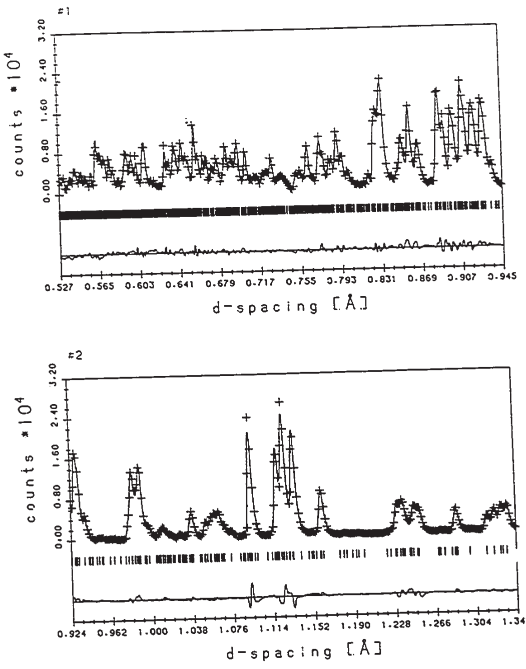

Fig(4.2) Neutron powder profile data fit for $CuSb_2O_6$. The crosses represent profile points, the solid line is the calculated profile, and the difference is plotted below. The bars underneath indicate the Bragg peak positions.

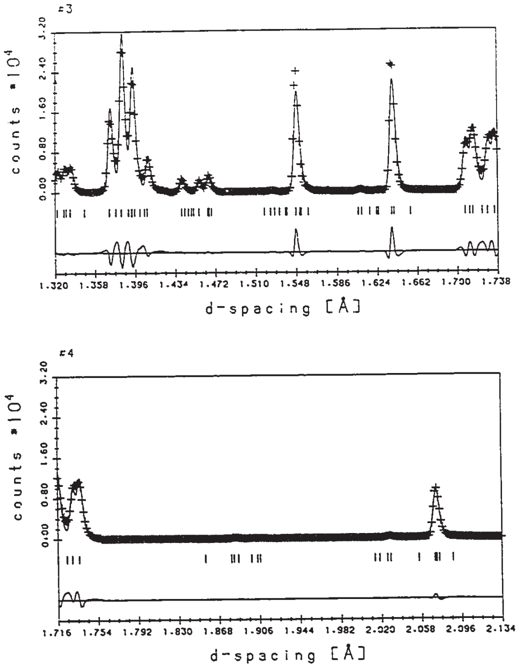

Continued.

The Cu^{2+} and Sb^{5+} cation positions are such that the magnetic ions are separated from each other by two sheets of diamagnetic ions. The Cu^{2+} ions are situated in the planes $z=0$ and $z=\frac{1}{2}$, whereas the planes at $z\approx 1/6$ and $z\approx \frac{1}{3}$ contain only Sb^{5+} ions. It is this aspect of the crystal structure which suggests that the magnetic properties of these materials can be understood in terms of two dimensional lattice. In fact, the magnetic sublattice is the same as that of the K_2NiF_4 structure, which is a canonical example of a square lattice two dimensional antiferromagnet.

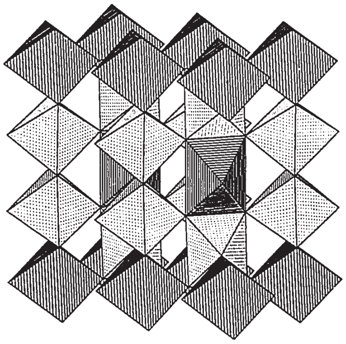

Fig(4.3) The crystal structure of $CuSb_2O_6$. The arrangement of the Cu atoms in layers is illustrated.

Table 4.3

Atomic Parameters for $CuSb_2O_6$

Atom	Site	x	y	z	B(Å^2)
Cu	*2a*	0.0	0.0	0.0	0.21(6)
Sb	*4e*	0.0011(9)	0.0080(10)	0.3338(6)	0.16(4)
O1	*4e*	0.3130(9)	0.2983(8)	0.0017(4)	0.13(5)
O2	*4e*	0.2991(8)	0.3176(7)	0.3291(4)	0.36(6)
O3	*4e*	-0.3012(8)	-0.2915(9)	0.3248(4)	0.63(7)

Table 4.4

Selected Bond Distances (Å) and angles (°) for $CuSb_2O_6$

Cu-2O(1)	2.004(4)	2O(1)-Cu-O(2)	92.27(15)
Cu-2O(2)	2.012(4)	2O(1)-Cu-O(3)	90.28(16)
Cu-2O(3)	2.120(4)	2O(2)-Cu-O(3)	102.31(15)
Sb-O(1)	2.013(7)	O(1)-Sb-O(1)	79.07(27)
Sb-O(1)	1.994(6)	O(1)-Sb-O(2)	90.36(25)
Sb-O(2)	1.993(6)	O(1)-Sb-O(2)	177.99(33)
Sb-O(2)	1.996(6)	O(1)-Sb-O(3)	91.67(25)
Sb-O(3)	1.973(6)	O(1)-Sb-O(3)	99.52(25)
Sb-O(3)	1.960(6)	O(1)-Sb-O(2)	94.52(25)
		O(1)-Sb-O(2)	99.55(25)
		O(1)-Sb-O(3)	89.15(25)
		O(1)-Sb-O(3)	177.39(33)
		O(2)-Sb-O(2)	88.28(21)
		O(2)-Sb-O(3)	176.09(36)
		O(2)-Sb-O(3)	87.68(25)
		O(2)-Sb-O(3)	89.77(25)
		O(2)-Sb-O(3)	81.91(26)
		O(3)-Sb-O(3)	88.69(21)

III- Magnetic Properties:

Magnetization and inverse susceptibility data for polycrystalline $CuSb_2O_6$ at an applied field of 200 Oe are shown in Fig(4.4). The magnetization data in Fig(4.4a) show a broad maximum at about 60 K which is indicative of the presence of a short range order and a sharp decrease at 9 K suggesting an onset of the long range order transition. These general features in the susceptibility were observed for all trirutile compounds of the composition AB_2O_6 that were studied to date.

Magnetic data from 120 to 340 K were fitted to a Curie-Weiss law after correction for the diamagnetism

$$\chi^{-1}_{corr} = \frac{(T-\Theta)}{C_m} \qquad (4.1)$$

giving $\mu_{eff} = 1.75\ \mu_B$ and $\Theta = -48$ K in fair agreement with those reported previously (D75). Below 100 K, the inverse susceptibility data, Fig(4.4b), deviates considerably from the Curie-Weiss law due to the presence of the short range order. The susceptibility attains a maximum value of 2.7×10^{-2} cm^3.mol^{-1} at 60 K, while the onset of 3-d ordering occurs at approximately 8 K.

It is possible to analyze the susceptibility data by the method suggested by Fisher (F62) to obtain an approximation to the magnetic specific heat. Fisher showed that the temperature variation of the specific heat of a simple antiferromagnet is essentially the

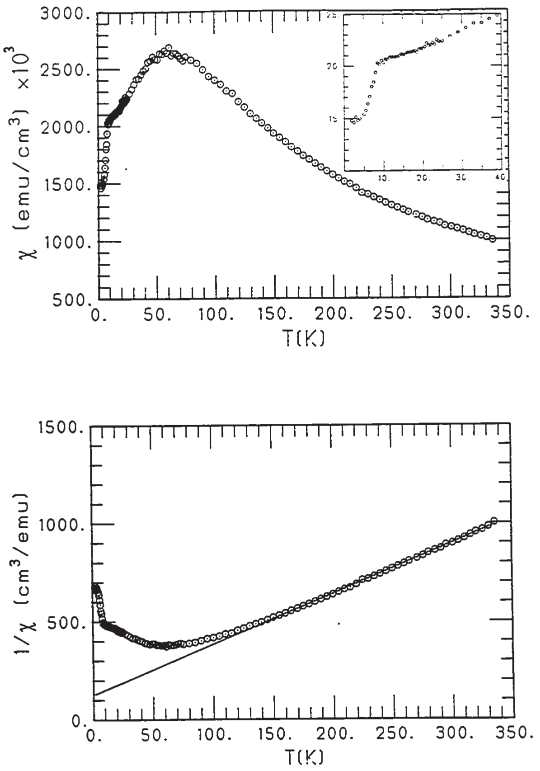

Fig(4.4) (a) The magnetic susceptibility versus temperature, inset shows an abrupt decrease at about 9 K, and (b) the inverse of the susceptibility versus temperature of $CuSb_2O_6$.

same as that of the temperature derivative of the susceptibility. More precisely he established the relation

$$C_M(T) \approx A\frac{\partial}{\partial T}(T\chi(T)) \qquad (4.2)$$

where A is a constant of proportionality slowly varying with T. This expression implies that any specific heat anomaly will be associated with a similar anomaly in $\partial(T\chi)/\partial T$. Thus the specific heat singularity, λ-type anomaly, normally observed at T_c is associated with a positively infinite gradient in the parallel susceptibility at T_c.

Fisher's specific heat can be used as an indicator for the presence of a phase transition as well as the presence of any short range ordering. Two features in $\partial(T\chi)/\partial T$ vs T plot, Fig(4.5), can be seen: a broad maximum at 60 K and a sharp spike at 9 K. The latter feature is more likely to be a transition to a long range ordered state.

Further evidence of this is found in Fig(4.6), where the magnetic moment was measured as a function of field at T = 2 K, and 11 K. Below T_c, at 2K, the curve shows two linear regimes, from H = 0 - 1 Tesla, and from H = 2 - 3 Tesla, with a transition region in between. This behavior is characteristic to a spin-flop transition in the polycrystalline samples. The 11K data on the other hand are linear throughout the entire field range which is typical of the paramagnetic state. Further measurements were done on the single crystal sample which clearly exhibit the spin flop transition.

Low temperature neutron diffraction provided the most reliable proof for the presence of the long range order in this material. The results of this experiment will be discussed later in the chapter.

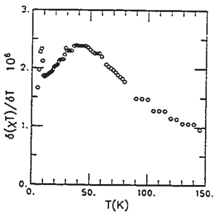

Fig(4.5) Fisher's specific heat of *$CuSb_2O_6$.*

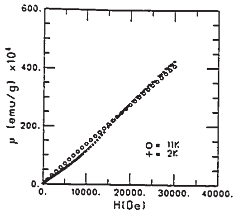

Fig(4.6) The magnetic moment variation as a function of the magnetic field of polycrystalline material of *$CuSb_2O_6$.*

III.1- Short Range Order:

As was noted earlier, the magnetic susceptibility data indicate a broad maximum which is a characteristic of the short range order. A more quantitative characterization of the short range order can be obtained through the fitting of the magnetic susceptibility data with the theoretical predictions of the relevant model systems.

In the process of analyzing the susceptibility data two parameters must be identified, namely, the spin dimensionality, *n*, and the lattice dimensionality, *d*. The single-ion magnetic properties of Cu^{2+} are fairly straight forward. Spin-orbit coupling is large, causing the g factor to lie in the range 2.0-2.3, and because Cu^{2+} has an electronic spin of ½, there are no zero-field splitting effects (C86). This makes it an excellent Heisenberg ion, with $n=3$, since isotropic interactions are required in order to apply the Heisenberg model system.

In order to determine the lattice dimensionality, *d*, the magnitude of the exchange interaction in various possible exchange pathways must be determined. The calculation of the magnitude of the superexchange for any given cation-ligand-cation configuration to a reasonable accuracy is a difficult task, but one can qualitatively estimate the relative strength of the different pathways.

By reference to Fig(4.1), the sublattice of the A^{2+} ions has *I4/mmm* symmetry or body-centered tetragonal, the same symmetry as that found in the K_2NiF_4. With respect

to the tirutile structure, it is apparent that the strongest coupling is expected to occur between the magnetic ions within the *ab* plane. The possible superexchange pathways for the nearest and next-nearest neighbor interactions are shown in Fig(4.7).

It is of interest to compare this situation with that of the better known K_2NiF_4-type compounds. The major difference is in the positions of the ligands. In the K_2NiF_4 the ligands are on edge bisectors, *i.e.* (½,0,0) etc., giving ideal 180° metal-oxide-metal superexchange pathways between nearest neighbors in the square planar array. In the $z=0$ plane in the trirutile structure the placement of the ligands gives the unusual superexchange linkages shown in Fig(4.7). Of the three exchange interactions indicated in Fig(4.7), J_2, is likely to be the strongest as all the interatomic distances are within bonding range and the bond angles are 180°. J_1 involves two unequal Cu-O bonds and an angle of 97° while J'_2 involves two long Cu-O distances of 3.36 Å and an angle of 166° and is likely to be the weakest (G92). Thus, the trirutile structure would seem to provide an example of a square planar lattice with dominant second neighbor interactions in contrast to the K_2NiF_4 structure where first neighbor interaction are dominant. However, the second neighbor interactions J_2 and J_2' are not equivalent, in fact $J_2 \gg J_2'$ is likely. Inspection of Fig(4.7) suggests the surprising possibility that a one dimensional antiferromagnetic chain model could be a fair approximation for the interplanar correlations. This situation is aided by a symmetry cancellation effect as each spin in a chain in the direction <110> has four neighboring spins in adjacent chains, two spin up and two spin down.

Realizing the chain model could be a viable choice in determining the lattice dimensionality of $CuSb_2O_6$, the susceptibility data were fitted to both models, the Heisenberg chain model and the Heisenberg quadratic model. The results of these fits are summarized below.

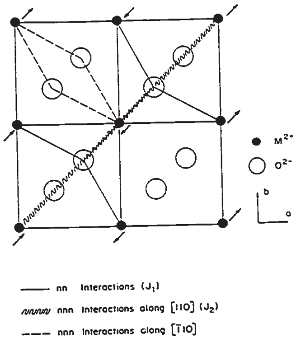

Fig(4.7) In-plane superexchange pathways in the trirutile structure (Ref G92).

1- The Chain Model:

The classical work on antiferromagnetic exchange coupled spin-½ chain compounds was done by Bonner and Fisher (B64). Hall (H81) fitted the numerical results of Bonner and Fisher for the magnetic susceptibility of the spin ½ uniform chain to the expression in equation (4.3)

$$\chi = \frac{Ng^2\mu_B^2}{kT}\cdot\frac{0.25 + 0.14995x + 0.30094x^2}{1 + 1.9862x + 0.68854x^2 + 6.0626x^3} \qquad (4.3)$$

where $x = |J|/kT$, and J is the exchange coupling constant between the neighboring spins in the chain. This closed-form expression is useful and has been used extensively. The exchange parameter J/k was estimated from the relation (J74)

$$\frac{kT(\chi_{max})}{|J|} = 1.282 \qquad (4.4)$$

Least squares fit which uses two adjustable parameters, g and J, provided a surprisingly good fit with an index factor R = 0.633% and $g = 2.16$ and $J/k = -46.94$ K. The fit is plotted in Fig(4.8).

2- The Quadratic Model

The 2-d Heisenberg model was studied in detail by Rushbrooke and Wood (R58), (R63), and Lines (L70). The magnetic susceptibility is expanded in inverse powers of the reduced temperature θ, given by kT/J as in equation (4.5) (L70),

$$\frac{1}{\bar{\chi}} = 3\theta + \sum_{n=0}^{6}\frac{(-1)^n C_n}{\theta^n} \qquad (4.5)$$

with

$$\bar{\chi} = \frac{J\chi}{Ng^2\mu_B^2} \qquad (4.6)$$

The coefficients, C_n, can be found in Ref(L70).

For this model the coupling constant was estimated from the relation (J74),

$$\frac{kT(\chi_{max})}{|J|\,S(S+1)} = 2.52 \qquad (4.7)$$

A least-squares fit based on this series expansion was attempted and the fit with the parameters g=2.25 and J/k= -30.43 K is clearly worse than that of the linear chain model as it is shown in Fig(4.8). This is reflected also in the index factor R = 3.25%.

Although the crystal structure indicates a nearly square planar Cu^{2+} lattice as in other trirutile compounds, a Cu-O-O-Cu superexchange pathway seems to be dominant.

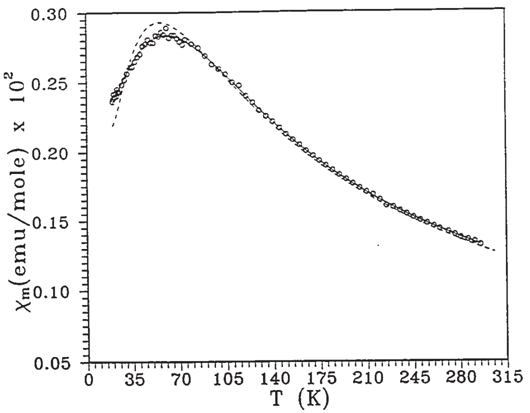

Fig(4.8) The magnetic susceptibility of $CuSb_2O_6$ compared with two $S = ½$ to Heisenberg models: linear chain (——) and quadratic lattice (——).

Thus, it can be concluded that the linear chain model, $d=1$, is a much better approximation to the short range order in $CuSb_2O_6$ than the square lattice, $d=2$. This is the first example in which the chain model prediction was realized in the trirutile systems.

It is certainly instructive to compare the results obtained in this study with those of the other members of the $M^{2+}Ta_2(Sb_2)O_6$. As in Table(4.5), $CuSb_2O_6$ stands out in two categories: largest $T(\chi_{max})/T_c$ ratio of 7.1 and largest dominant in-plane exchange constant J/k= -43 K. The $T(\chi_{max})/T_c$ could be taken as a crude measure of the relative importance of the short range versus long range order. This ratio serves as a crude measure due to the fact that the intrachain coupling constant, J', is proportional to $T(\chi_{max})$, while T_c is related to J', the interchain constant.

Table 4.5

Relevant Magnetic Data For $A^{2+}Ta_2(Sb_2)O_6$ Compounds

Phase	$T(\chi_{max})$ (K)	T_c(K)	$T(\chi_{max})/T_c$	J/k(K)	Ref
$FeTa_2O_6$	15	8.1	1.7	-16	E86
$CoTa_2O_6$	15.6	6.6	2.3	-16.8	K88.1
$CoSb_2O_6$	35	13.0	2.7	-	R89.1
$NiTa_2O_6$	25	10.3	2.4	-15	K88
$NiSb_2O_6$	36	-	-	-	R89.2
$CuSb_2O_6$	60	8.5	7.1	-43	N90

Oguchi (O64) developed a relationship, equation (4.8), that gives a reasonable estimate of J'/J based on the values of T_c and $|J|$.

$$\exp\left(\frac{2|J|}{kT_c}\right) = \frac{(4+z\eta)}{z\eta} \qquad (4.8)$$

where $\eta = |J|/|J'|$ and z is the number of neighbors in the *ab* plane. On this basis, $J'/J \approx 2\times10^{-3}$ for $CuSb_2O_6$, which is comparable to other Cu^{2+} compounds generally regarded as good examples of linear chain behavior such as $CuCl_2.\ 2NC_5H_5$ ($J'/J = 4\times10^{-3}$) and $CuSeO_4.\ 5H_2O$ ($J'/J = 1.3\times10^{-3}$) (J74).

The second feature is that, of all the known $M^{2+}Ta_2(Sb_2)O_6$ trirutile oxides, $CuSb_2O_6$ shows the clearest evidence yet for the dominance of one-dimensional correlations in the short range ordered regime.

It seems peculiar that among all the trirutile phases of the formula AB_2O_6 only $CuSb_2O_6$ gives the clearest evidence for a chain model. This could be due in part to the fact that the energy of the *3d* atomic orbitals of Cu and that of *2p* orbitals of O are comparable. This may enhance the degree of overlap between the *3d-2p* orbitals thus making the exchange coupling constant larger. This overlap would be most favorable in the case of 180° pathway, leading in turn to the dominance of the 1-d model. This could be more rigorously formulated mathematically by the expression in equation (4.9) (C92),

$$J = -2t^2\left[\frac{1}{U} + \frac{1}{E_{CT}}\right] \qquad (4.9)$$

where t is the hopping integral between the overlapping orbitals, 3d from the transition metal ion and 2p from the oxygen anions, U is the correlation energy, and E_{CT} is the

energy of the charge transfer. The dominant factor in this equation is the charge transfer term. The E_{CT} term is directly related to the energy gap between the *3d* orbitals of the metal and the *2p* orbitals of the ligands. The progressive decrease in the energy gap between these orbitals, *3d and 2p*, leads to a more covalent mixing between metal *d* orbitals and the oxygen *p* orbitals, and so a larger effective overlap via the common oxygen between the metal ions. For transition metal oxides, this charge transfer term would be smallest in the case of copper oxides and a larger degree of overlap between the *3d-2p* orbitals is expected. This could account, among other factors, for the fact that the exchange coupling, J/k, is largest for $CuSb_2O_6$ and that the spin interactions are strongest along the chains. It is this property of copper oxides that is believed to be responsible for much of the superconductivity in the high temperature superconductors.

This is an excellent example illustrating the sensitivity of the magnetic properties to very subtle differences between isostructural compounds such as the electron configuration of the metal ion or the energy of its *d*-orbitals.

III.2- Long Range Order:

One dimensional systems can not undergo a phase transition to a long range ordered state at any finite temperature. As all magnetic compounds exist in three space dimensions, interplanar exchange and out-of-plane forces will act to induce long range magnetic ordering at temperatures higher than 0 K (G92). It is the interplanar exchange, J', in $CuSb_2O_6$ which would be responsible for the long range order in this compound.

A useful relation relating T_c and J' has been given by Villain and Loveluck (V77) in which they assumed that the long range order is achieved when the thermal energy is comparable to the interaction energy between blocks of correlated spins of the z' neighboring chains. For Heisenberg chains it was shown that the T_c and the interplanar exchange, J', are related by the relation (4.10),

$$T_c \propto \sqrt{JJ'} \qquad (4.10)$$

In $CuSb_2O_6$, this crossover from one dimensional to three dimensional magnetic ordering was suggested by the abrupt decrease in the magnetic susceptibility data. We tried to verify this proposition by the use of low temperature neutron diffraction. Preliminary data sets were taken at 4.2 K at McMaster Nuclear Reactor, MNR. There was no sign of any magnetic superlattice reflections in the data collected at MNR, indicating that the copper magnetic moment may be less than one Bohr magneton.

Similar measurements were later collected on the Dualspec at Chalk River labs where the neutron flux is much higher than that of the MNR. Several data frames were collected at different temperatures varying from 5 K to 12 K. A very weak superlattice reflection was observed at 5 K, which vanished at 12 K as in Fig(4.9).

This superlattice reflection was modelled to a Gaussian peakshape in order to determine its position, 2θ angle. After correcting for the zero angle shift, the peak position was found to be 8.1°. This peak was indexed as (½, 0, ½) in the chemical cell.

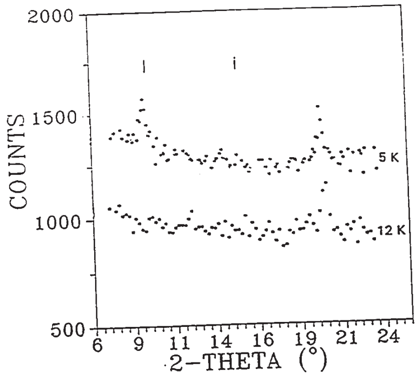

Fig(4.9) Low temperature neutron scattering of $CuSb_2O_6$.

The propagation vector $k = (½,0,½)$, *i.e.* $a_{mag} = 2a$, $b_{mag} = b$, $c_{mag} = 2c$, was then proposed. This proposition is in line with other trirutile oxides. In these oxides, there are basically two magnetic structures reported. The most commonly occurring magnetic structure is described by propagation vector $k = (½,0,½)$, which the oxides $CoSb_2O_6$ (R89.1), $NiSb_2O_6$ (R89.2) and $FeTa_2O_6$ were reported to adopt. Two magnetic models, which are indistinguishable from the powder data, were reported. The magnetic structures can be described in terms of two sublattices (origin and body-center) where the moments within one sublattice are antiparallel along <100> and <001> but parallel along <010>. All moments lie within the *ab* plane along <110> and $<1\bar{1}0>$. The structures differ in the angle of the moments between the two sublattices. A schematic illustrations of the magnetic unit cell are shown in Fig(4.10), the collinear model is shown on the left and the orthogonal model on the right.

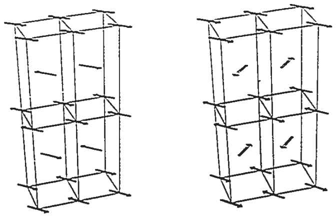

Fig(4.10) Schematic illustrations of the (2a,a,2c) magnetic cell of $CuSb_2O_6$. The collinear model is on the left and the orthogonal model on the right (Ref R89.1).

The other known propagation vector is $k = (¼,¼,¼)$ which is reported for the oxides $CoTa_2O_6$ (R89.1) (K88), and $NiTa_2O_6$ (R89.2) (K88).

Because of the weak intensity of the magnetic reflection in $CuSb_2O_6$, it is not possible to refine the magnetic structure using the Rietveld refinement. Instead, a simulation of the intensity of the peaks was attempted where the magnetic moment is varied between 0.5 to 1.0 μ_B.

This simulation, which is used to estimate the moment of Cu^{2+}, was handled by the **Rietan** program. After careful assessment of the simulated patterns, it was found that the magnetic moment is more likely to be 0.5 μ_B. For moment values as large as .7 μ_B, another magnetic reflection at 15.48° with the Miller indices (½,0,3/2) appears which vanishes when the moment was set at 0.5 μ_B. Similar result was reported for $La_{2-x}Sr_xCuO_4$ (C92) in which the magnetic moment of Cu^{2+} was as low as 0.5 μ_B. This could result from the fact that superexchange interactions partly delocalize the unpaired spin.

Looking closely to the proposed magnetic structures, the magnetic antiferromagnetically coupled chains are translated by ½<110> with respect to each other giving rise to frustrated interchain coupling. It is this frustration that may in part cause the weakness of the interactions in the plane and hence the interactions along these chains dominate.

Further evidence on the presence of the long range order could be drawn from the spin flop phase transition. The spin flop transition is most easily described by considering the magnetic field, H, versus temperature phase diagram as in Fig(11). When a field H is applied parallel to the preferred axis of spin alignment in an antiferromagnet, *i.e.* $T < T_c$, the moments flop perpendicular to the field as the field reaches a critical value. This is then the thermodynamically favored state. As the field reaches a high enough value, there is finally a transition from the spin flop to the paramagnetic state.

This spin flop behavior was registered for the $CuSb_2O_6$ single crystal as shown in Fig(4.12) where magnetic moment versus magnetic field data are plotted. The measurement was done while the crystal is oriented in such a way that the applied field

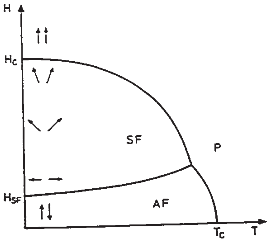

Fig(4.10) The phase diagram of materials exhibiting the spin flop transition.

was parallel to the easy axis. It shows clearly the presence of the spin flop transition at 2.8 Tesla. This transition is a further evidence of the presence of an antiferromagnetic ordered state.

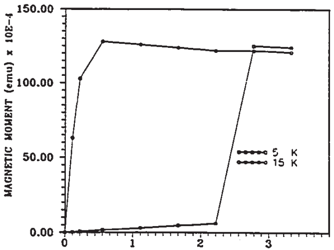

Fig(4.11) Spin flop transition in $CuSb_2O_6$.

Chapter 5

Transition Metal Arsenates

I- Introduction:

As a continuation to our research on the structural and magnetic properties of the oxides of the general formula AB_2O_6, we directed our efforts to investigate another class of AB_2O_6 transition metal oxides in which Sb^{5+} is replaced by As^{5+} as the cation B in the general formula AB_2O_6. These arsenates adopt the $PbSb_2O_6$ structure where the cations A and B are segregated into layers. The magnetic lattice in this structure is sharply different from that of the trirutile structure. Hence it was thought that the magnetic properties of this system would be markedly different as well.

Surprisingly, these compounds have received very little attention since they have been reported by Magneli (M41). Magneli synthesized and determined the cell parameters of cobalt arsenate along with some other alkaline earth arsenates.

Taylor *et al* (T58) then reported the synthesis of $CoAs_2O_6$ and $NiAs_2O_6$, the cell parameters were determined using X-ray powder diffraction. These cell parameters were in accordance with those reported previously by Magneli, as in Table(5.1). Kasper (K67) investigated the spectrophotometrical properties of $CoAs_2O_6$ and $NiAs_2O_6$ among other oxides of the general formula AB_2O_6.

Table 5.1
Cell Parameters of AAs_2O_6 Compounds

Phase	This Work		Taylor		Magneli	
	a(Å)	c(Å)	a(Å)	c(Å)	a(Å)	c(Å)
$NiAs_2O_6$	4.7585_7	4.4349_4	4.759_2	4.427_2	-	-
$CoAs_2O_6$	4.7768_{12}	4.4968_8	4.775_2	4.499_2	4.766	4.493
$MnAs_2O_6$	4.7956_9	4.6923_6	-	-	-	-

A detailed structural study of these compounds had not been reported. Magneli proposed that these arsenates adopted the lead antimonate structure with the A^{2+} and As^{5+} atoms assigned to special positions in the space group *P312*, and the oxygen atom coordinates were determined from crystal-chemical considerations. The unit cell of the structure is shown in Fig(5.1).

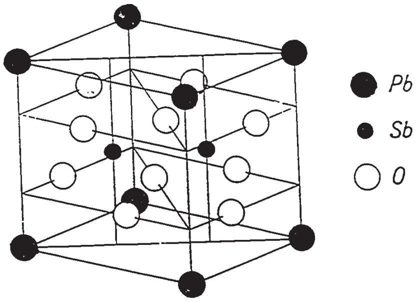

Fig(5.1) The unit cell of the $PbSb_2O_6$ structure (Ref M41).

II- Crystal Structures:

Since these arsenates could not be obtained in a single crystal form, the refinement of their crystal structures was done on neutron diffraction data obtained from polycrystalline samples. For crystal structure refinement from powder samples, the results obtained with neutron data tend to be more accurate than those obtained with X-rays, for several reasons:

1- the peak shape functions are generally simpler in CW neutron diffractometers. They can be modelled satisfactorily by a Gaussian peak shape where as TOF and X-ray peak shapes can only be approximated.

2- neutron scattering lengths have essentially no angular dependence in the range of interest, so that the scattering power of the atoms does not diminish as rapidly at high 2θ angles. This, in turn, means that meaningful data can be collected to much higher angles and the thermal parameters can be estimated much better.

3-the neutron scattering length of oxygen ($b=0.58\times10^{-12}$ cm) compares well with those of the cations A and B, *i.e.* As ($b = 0.65\times10^{-12}$ cm), Co ($b = 0.25\times10^{-12}$ cm), Ni ($b = 1.03\times10^{-12}$ cm), and Mn ($b = -0.39\times10^{-12}$ cm) allowing the oxygen parameters to be determined with relatively good accuracy.

In the course of the refinement of these arsenates, the structure was described, initially, in the space group *P312*, *i.e.* Magneli model, with A^{2+} ions at the origin and the As^{5+} ion distributed over two special positions, *1d (⅓, ⅔, ½)* and *1f (⅔, ⅓, ½)*, and the O atoms in the general position *6l* with the coordinates *(x, 0, z)*. The refinement results confirmed the general atomic arrangements proposed by Magneli but some problems were noticed such as the instability of the refinement, and negative temperature factors, also the lack of convergence when the O atom coordinates were released. This refinement instability added to the suspicions about the structural model that had arisen by the presence of two As sites and a zero value for the variable *y*-coordinate of O.

The failure of the refinement in this space group led to the trial of other possible space groups which would leave the atomic arrangements intact but provide a special position for As with a two-fold symmetry and a special position for the O with the coordinates *(x, 0, z)*. These requirements were met in the space group *P-31m* . A rapid convergence with a better fit was obtained with this space group. In this space group, A^{2+} occupies the site *(1a)* at the origin, As^{5+} occupies the site *(2d)* with the coordinates *(⅓, ⅔, ½)* which is doubly degenerate instead of splitting the As into two positions as in the *P312* space group, and the oxygen occupies the special position *(6k) (x, 0, z)*.

This confirms the prediction of Hill (H87) where he anticipated that the space group *P312* has an unnecessarily low symmetry for the AB_2O_6 arsenates.

A full matrix least squares refinement with 18 variable parameters was performed on the neutron diffraction data for each of the three phases. The refined variables included a scale factor, cell parameters, positional parameters, isotropic thermal parameters, asymmetry, preferred orientation, background and profile parameters. Reasonable fits were obtained for both $NiAs_2O_6$ and $CoAs_2O_6$.

For $NiAs_2O_6$, the Rietveld refinement fit is plotted in Fig(5.2) and the final results of the refinement are tabulated in Table(5.2) which includes the data collection conditions, the cell parameters, the atomic positions of the atoms in the unit cell, and a number of selected bond distances and angles. The NiO_6 octahedron is very symmetric with a Ni-O bond distance of 2.098(6) Å which is in accordance with the sum of the ionic radii of both ions(2.06 Å). Ni^{2+} appears to be situated in the center of the octahedron as indicated by the O-Ni-O bond angles. The As-O bond length is 1.827(2) Å which is close to the sum of the ionic radii of As^{5+} and O^{2-} (1.86 Å).

In the case of $CoAs_2O_6$, similar results were obtained. Table (5.3) summarizes the results of the refinement and Fig(5.3) plots the refinement pattern. The Co-O bond length

Table 5.2
The Rietveld Refinement Results of $NiAs_2O_6$

a (Å)	4.7585(7)
c (Å)	4.4349(4)
Volume ($Å^3$)	86.97
Space Group	*P -31m*
2*θ* range (°)	12 - 115
Step Size (°)	0.1
λ (Å)	1.392
No. of data points	1070
Independent reflections	93
No. parameters refined	18
R_{wp}	7.85%
R_p	6.07%
R_{exp}	2.5%

Atomic positions and Bond angles and distances:

Atom	Site	x	y	z	B($Å^2$)
Ni	*1a*	0.0	0.0	0.0	0.16(6)
As	*2d*	1/3	2/3	1/2	0.62(7)
O	*6k*	0.3595(6)	0.0	0.2739(5)	0.49(4)

$Ni-O_c$	2.098(2)	O_c-Ni-O_c	180.0
$Ni-O_a$	2.098(6)	O_c-Ni-O_a	89.84(5)
		O_c-Ni-O_d	90.16(5)
$As-O_c$	1.827(2)	O_a-As-O_f	82.52(6)
$As-O_c$	1.827(7)	O_a-As-O_a	92.77(11)
		O_a-As-O_c	173.23(12)

symmetry labels: a = (x, 0, z), b = (0, x, z), c = (-x, -x, z)
d = (-x, 0, -z), e = (0, -x, -z), f = (x, x, -z)

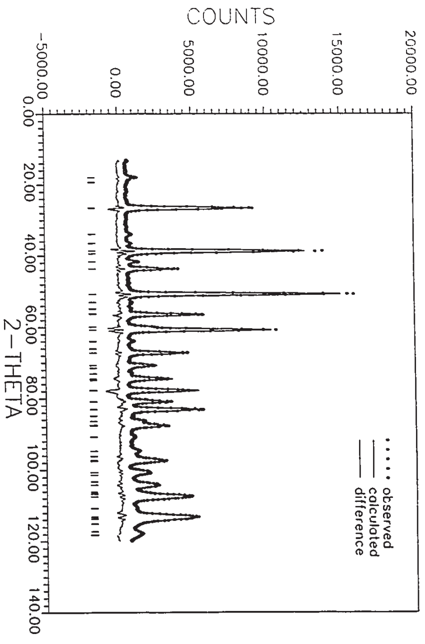

Fig(5.2) The Rietveld refinement pattern of neutron diffraction data for $NiAs_2O_6$. The circles is the observed profile and the solid line is the calculated profile, the difference is plotted below and the bars indicate the Bragg peaks positions.

was 2.131(2)Å which, although it is larger than the average Co-O bond length (2.111 Å) (sum of ionic radii = 2.115Å), it still falls within the range of the reported values for the Co-O bond lengths (1.959 - 2.517 Å) (W92). The As-O bond length of 1.830(3) Å was very similar to that reported in the $NiAs_2O_6$ compound. In a thorough study of the CoO_6 polyhedra in inorganic compounds, Wilder (W92) surprisingly found that Co^{2+} ions reside in low symmetry sites and that only 2% of the 112 $Co^{2+}O_6$ octahedra that were included in the study have the point symmetry *-3m*.

Regarding $MnAs_2O_6$, the cell parameters were obtained by analysis of the line positions obtained from the Guinier film. Later, similar procedures were followed in refining the structure. Table (5.4) summarizes the refinement results while the refinement pattern is plotted in Fig(5.4). The Mn-O bond distance obtained from the refinement was 2.214(3) Å which compares well with the sum of the ionic radii with Mn^{2+} having a high spin electronic configuration (2.18 Å).

The framework of this structure type is based on a hexagonal network of oxygen atoms filled with alternate layers of octahedral sites that are ⅔ filled by As^{5+} ions and ⅓ by the A^{2+} ions. This leads to sheets of edge sharing AsO_6 octahedra while the transition metal ions are located in isolated octahedral sites. This can be best seen in the (001) projection as in Fig(5.5). This structure is then can best be described as consisting of arsenic sheets that form honeycomblike rings of edge sharing AsO_6 octahedra with an

Table 5.3
The Rietveld Refinement Results of $CoAs_2O_6$

a (Å)	4.7768(12)
c (Å)	4.4968(8)
Volume ($Å^3$)	88.09
Space Group	*P -31m*
2*θ* range (°)	12 - 115
Step Size (°)	0.1
λ (Å)	1.392
No. of data points	1030
Independent reflections	86
No. parameters refined	18
R_{wp}	8.51%
R_p	6.59%
R_{exp}	2.59%

Atomic positions and Bond angles and distances:

Atom	Site	x	y	z	B($Å^2$)
Co	*1a*	0.0	0.0	0.0	0.48(10)
As	*2d*	1/3	2/3	1/2	0.30(7)
O	*6k*	0.3626(6)	0.0	0.2759(7)	0.53(8)

$Co-O_c$	2.131(2)	O_c-Co-O_c	180.0
$Co-O_a$	2.131(6)	O_c-Co-O_a	89.50(6)
		O_c-Co-O_d	90.50(6)
$As-O_c$	1.830(3)	O_a-As-O_f	82.18(8)
$As-O_c$	1.830(2)	O_a-As-O_a	92.58(10)
		O_a-As-O_c	173.41(12)

Table 5.4
The Rietveld Refinement Results of $MnAs_2O_6$

a (Å)	4.7956(9)
c (Å)	4.6923(6)
Volume (Å^3)	93.45
Space Group	P -$31m$
2θ range (°)	12 - 100
Step Size (°)	0.1
λ (Å)	1.392
No. of data points	980
Independent reflections	100
No. parameters refined	18
R_{wp}	8.13%
R_p	5.98%
R_{exp}	3.10%

Atomic positions and Bond angles and distances:

Atom	Site	x	y	z	B(Å^2)
Mn	*1a*	0.0	0.0	0.0	0.29(11)
As	*2d*	1/3	2/3	1/2	0.81(6)
O	*6k*	0.3704(3)	0.0	0.2835(5)	1.20(4)

Mn-O_c	2.214(3)	O_c-Mn-O_c	180.0
Mn-O_a	2.214(6)	O_c-Mn-O_a	89.84(5)
		O_c-Mn-O_d	90.16(5)
As-O_c	1.826(2)	O_a-As-O_f	81.39(6)
As-O_c	1.826(1)	O_a-As-O_a	92.07(5)
		O_a-As-O_c	170.33(6)

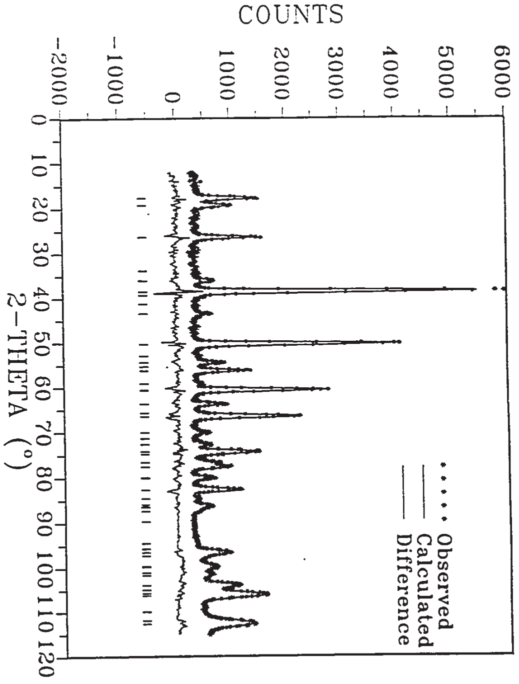

Fig(5.3) The Rietveld refinement pattern of neutron diffraction data for $CoAs_2O_6$. The circles is the observed profile and the solid line is the calculated profile, the difference is plotted below and the bars indicate the Bragg peaks positions.

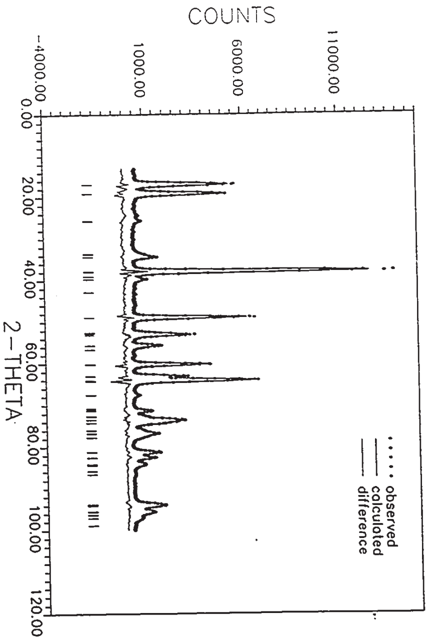

Fig(5.4) The Rietveld refinement pattern of neutron diffraction data for $MnAs_2O_6$. The circles is the observed profile and the solid line is the calculated profile, the difference is plotted below and the bars indicate the Bragg peaks positions.

As-O bond length of 1.823 Å. The transition metal ions are located in isolated octahedral sites with symmetry -$3m$ positioned above and below the vacant site, *i.e.* the centers of the rings in the arsenic layers.

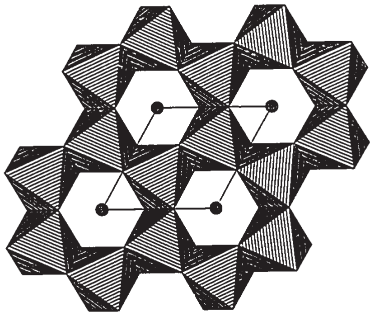

Fig(5.5) (001) projection of the AAs_2O_6 structure.

Often compounds of Co^{2+} (r = 0.745 Å) and Ni^{2+} (r = 0.690 Å) are isostructural (W92) while the larger Mn^{2+} (r = 0.830 Å) sometimes adopts different structure as in the case of the transition metal antimonates. This marks another difference between this structure type and the trirutile structure.

The segregation of the two types of cation into alternate octahedral layers of the AAs_2O_6 structures allows a wide range of A cations to be accommodated into the structure. Several arsenates have indeed been reported where the transition metal ions are replaced by larger cations such as Ca, Sr, Hg, Cd, and Pb which occupy the A position in the AAs_2O_6.

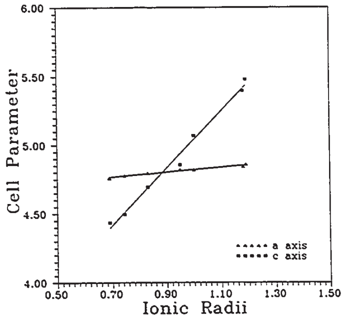

Fig(5.6) The variation of the unit cell parameters as a function of the cation size.

The variation in unit cell dimensions as a function of the ionic radius of the A cation for several arsenates adopting this structure is plotted in Fig(5.6) (data of the cell parameters were taken from ref M41, and this work). The *a*-axis for the series changes only slightly as a function of the A cation radius, in spite of the fact that the cation sizes differ by as much as 50%. On the other hand, the *c*-axis increases substantially along the series as the radius of the A cation increases.

The stability range of this structure is really dependent on the ratio of the ionic radii of A and B ions. As far as the arsenates are concerned, the upper and lower limits for the radius ratio (A^{2+}:As^{5+}) are 2.6 and 1.5 according to Hill (H87).

III- Magnetic Properties:

III.1- Magnetic Susceptibility:

Magnetic susceptibility data were measured on polycrystalline samples of each of the three compounds. Similar behavior was observed in all of the three phases. In a sharp contrast to the transition metal antimonates in the trirutile structure, there was no indication of the presence of any short range order in the magnetic susceptibilities of these arsenates. This observation was again apparent from the Curie-Weiss fits in which there were no deviations at lower temperatures from the predictions of the Curie-Weiss law. In general, the magnetic susceptibilities of these compounds resemble that of a simple antiferromagnet. All three compounds exhibited what appears to be a magnetic long range order transition.

Analysis of the magnetic susceptibility is outlined below, the long range order in these compounds was investigated further with low temperature neutron diffraction, a discussion of which will be delayed to the next section.

1- $CoAs_2O_6$:

Fig(5.7a) shows the magnetic susceptibility data as a function of temperature of $CoAs_2O_6$ at an applied field of 0.1 Tesla. The susceptibility attains a maximum of 3.63×10^{-2} emu/mole at T = 20 K and then drops sharply as the temperature was lowered. The data above the ordering temperatures, between 50 - 270 K, were fitted to

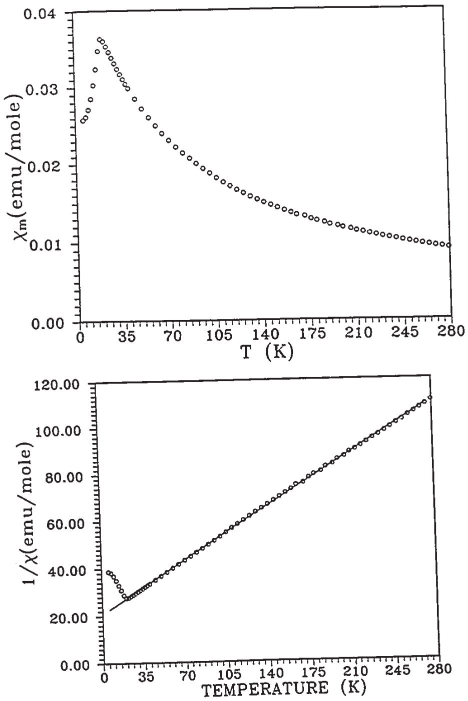

Fig(5.7) (a) Magnctic susceptibility of the $CoAs_2O_6$; (b) the inverse of the magnetic susceptibility versus temperature. Circles represent the observed data and solid line denotes the prediction of the Curie-Weiss fit.

a Curie-Weiss law after correcting for the diamagnetism. The inverse susceptibility is plotted in Fig(5.7b). The fit gives an effective moment of 4.98(1) μ_B and a Weiss constant, Θ, of -64.4(4) K. The effective magnetic moment of Co^{2+} in this compound falls within the acceptable range of the divalent cobalt ions which is 4.4 - 5.2 μ_B (M). Some deviations at the high temperatures were apparent, this is a result of the contributions of the T.I.P. or temperature independent paramagnetism. Such deviations are the result of the contributions of other excited states to the susceptibility in addition to that of the ground term. This contribution was found to be equal to 3.2×10^{-4} emu/mole. This could, at least qualitatively, be explained from the knowledge of the energy levels and the wavefunctions of the ion.

Abragam and Pryce (A51) gave an elegant account of the magnetic properties of Co^{2+} in octahedral and distorted octahedral sites. The ^4F term is split into two triplets and one singlet, an orbital triplet being lowest in energy. The addition of lower symmetry fields causes further splitting of the energy levels. A schematic energy-level diagram for Co^{2+} in a trigonal field is given by Jesson (J66), Fig(5.8). The $^4T_{1g}$ ground term is further split into six Kramers doublets. The separation of the lowest doublets are of the order of hundreds of cm^{-1} in which case more than one doublet has an appreciable population at room temperature. This is believed to be the cause for the T.I.P contribution to the susceptibility.

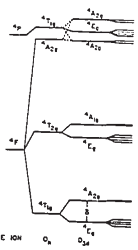

Fig(5.8) The energy diagram of Co^{2+} in a trigonally distorted octahedral environment. (Ref J66).

2- $NiAs_2O_6$:

Fig(5.9a) shows the plot of the magnetic susceptibility data measured at 0.1 T. The maximum in the susceptibility was 1.35×10^{-2} emu/mole and was observed at 30 K. Fig(5.9b) shows the plot of the Curie-Weiss fit. The effective magnetic moment was 3.27(7) μ_B and Θ was -66.2(8) K. Similar moment values were reported for Ni^{2+} ions as in $Ni(NH_3)_6Cl_2$ which has an effective moment of 3.2 μ_B (E68). Some T.I.P contribution was observed and estimated at 4.0×10^{-4} emu/mole which is an order of magnitude smaller than that of $CoAs_2O_6$. Similarly, the crystal field splits the free ion term of Ni^{2+} in such a way that an orbitally non-degenerate A_2 term lies lowest. Spin-orbit coupling introduces a small zero field splitting.

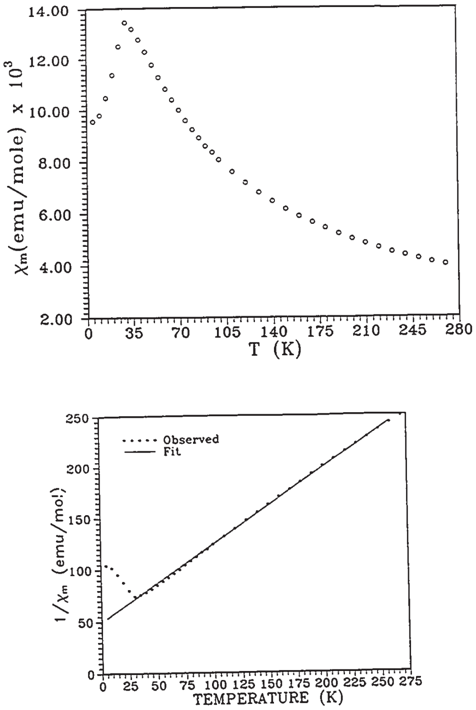

Fig(5.9) (a) Magnetic susceptibility versus temperature for $NiAs_2O_6$; (b) the inverse of the magnetic susceptibility versus temperature. Circles represent the observed data and solid line denotes the prediction of the Curie-Weiss fit.

Looking at Fig(5.9b), it can be seen that there are some deviations from the expected straight line of the Curie Weiss law beginning below about 30 K. These deviations seem to indicate the presence of short range correlations that are ferromagnetic in origin. This stands to be a unique feature for $NiAs_2O_6$ compounds that is not shared by the other two phases. Within the planes perpendicular to the *c* axis, neighboring Ni^{2+} atoms are linked through bonds to oxygen atoms at a bond angles of 90°. As the Goodenough-Kanamori rules predict ferromagnetic interactions for this arrangement, ferromagnetic short range order within the planes can be anticipated.

3- $MnAs_2O_6$:

The susceptibility data of $MnAs_2O_6$ is plotted in Fig(5.10a) and the maximum value of 1.19×10^{-1} emu/mole is reached at about 13 K. The susceptibility data in the range between 20 - 280 K were fitted to a Curie Weiss law the results of which are plotted in Fig(5.10b). The effective magnetic moment obtained from this fit was 5.90(2) μ_B and Θ was -20.7(1). The Curie-Weiss law predictions fit the observed data rather well. This is because the ground state level of Mn^{2+} is ^6S which is not split by the octahedral crystal field, but gives rise to a $^6A_1$ term. This term is an orbital singlet and consequently it has no orbital angular momentum associated with it. Thus spin-orbit coupling can not raise the degeneracy of this term, and furthermore because there are no excited terms with the same multiplicity as the ground term there can be no second-order mixing due to spin-orbit coupling nor can there be any second-order Zeeman effect. As

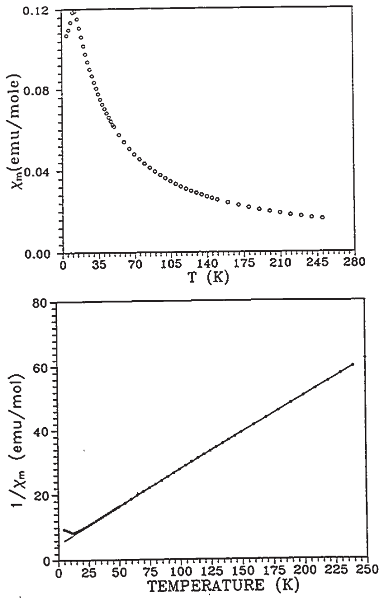

Fig(5.10) (a) Magnetic susceptibility versus temperature for $MnAs_2O_6$; (b) the inverse of the magnetic susceptibility versus temperature. Circles represent the observed data and solid line denotes the prediction of the Curie-Weiss fit.

a result, the magnetic properties are therefore simply due to the spin contribution and the theoretical magnetic moment is

$$\bar{\mu} = \sqrt{4S(S+1)}\,\mu_B = 5.92\ \mu_B \tag{5.1}$$

which compares very well with the experimental moment for $MnAs_2O_6$.

Table 5.5
Magnetic Susceptibility Parameters of the AAs_2O_6 Compounds

Phase	T_{max}(K)	$\mu_{eff}(\mu_B)$	θ(K)	TIP(cm³/mole)	R*
$NiAs_2O_6$	30 K	3.27(7)	-66.2(8)	4.0×10^{-4}	1.56%
$CoAs_2O_6$	20 K	4.98(6)	-64.4(4)	3.2×10^{-3}	4.18%
$MnAs_2O_6$	13 K	5.90(2)	-20.7(1)	0.0	1.23%

* $R(\%)=100\ \{\Sigma(\chi_{obs}-\chi_{cal})^2 / \Sigma\chi_{obs}^2\}^{1/2}$

Table (5.5) summarizes the experimental values of the susceptibility parameters for these arsenates.

One important feature that distinguishes these oxides from the trirutile compounds is the absence of any significant short range correlations in their magnetic susceptibility.

The absence of short range correlations could be traced to two structural features. Firstly, the *a* and *c* axes are almost identical in the hexagonal unit cell which, in turn, leads to intra-planar coupling interactions that are comparable in strength to the inter-planar interactions, or even larger as in these arsenates. Consequently, the onset of the long range order results before any appreciable short range order can be detected. Secondly, the symmetry cancellation effect which was crucial for the presence of the short range order in the trirutile and K_2NiF_4 structures is not relevant to this structure. In addition, this structure imposes restrictions on the distances and bond angles which connect the magnetic ions and hence dictate the potential exchange pathways that can give rise to magnetic correlations. The possible exchange pathways in this structure type are shown in Fig(5.11) in which the (100) projection is depicted. Remarkably, the (100) projection resembles very closely the (001) projection of the trirutile structure in Fig(4.7) except for the relative positions of the ligands. The nearest neighbor interaction J_1 involves the path A-O-A with two unequal A-O bonds of 2.0 Å and 3.3 Å and an angle of 90° and the next-nearest neighbor interaction J_4 involves the path A-O-O-A where the angle A-O-O is 160° with an A-O bond distance of 2.0 Å and O-O bond distance of 2.4Å.

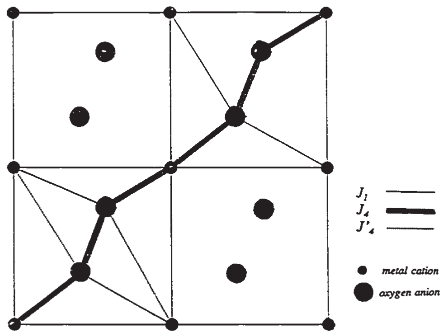

Fig(5.11) The possible superexchange pathways in the AAs_2O_6 compounds.

III.2- Long Range Order:

Magnetic ordering in the triangular lattice is a well studied problem. Antiferromagnetic ordering on a single triangular lattice is frustrated because at least one antiferromagnetic bond on each triangular must be broken. however, when triangular lattices are stacked along the third dimension and inter-planar interactions are non-zero, then long-range ordering can occur. This ordering is very dependent on the way magnetic ions are stacked with respect to each other. In these oxides, the magnetic ions form layers perpendicular to the *c* axis. These layers are stacked in such a way that the sites of the magnetic ions are directly above and below each other with no offset in the <100> or <010> directions which results in what is known as ...AAA... stacking. Reimers *et al* (R92.2) studied the ordering in the triangular spin systems with various stacking arrangements using the mean field theory formalism. They studied the effect of the relative strength of the in-plane and inter-plane interactions in stabilizing a particular ordered state. The spin Hamiltonian in equation (5.2) was considered:

$$H = -\frac{1}{2}\sum_{r,r'} J(r-r')\, S_r . S_{r'} \qquad (5.2)$$

where *J(r-r')* now represents an exchange mediated interaction and S_r is a spin with *n* components.

In order to see the effects of further neighbor interactions on the ordered state, the phase diagrams were calculated in the space of various nearest and next-nearest interactions, *i.e.* $J_2/|J_1|$ and $J_3/|J_1|$, and $J_4/|J_1|$ and $J_3/|J_1|$, these interactions are labelled in Fig(5.12a). The results of the calculations are shown in the form of phase diagrams. For systems with small inter-planar spacings the bond distance spanned by J_2 may be longer than the J_4 bond distance. J_4 may also be important for other systems since there are twelve J_4 and only six J_2 bonds. The phase diagram in the space $J_4/|J_1|$ and $J_3/|J_1|$ is shown in Fig(5.12b). The phase diagram is divided into regions characterized by the wavevectors *(⅓, ⅓, 0)* which represents a three sublattice order with each

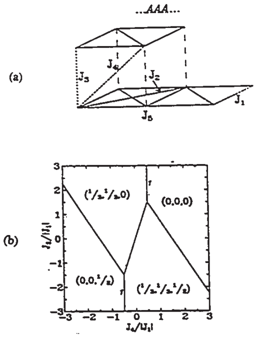

Fig(5.12) The mean field predictions of the possible ordered states in the triangular lattice with the AAA stacking: (a) illustrating the possible interactions in this lattice type, (b) the calculated phase diagram in the interactions $|J_3|/|J_1|$ and $|J_4|/|J_1|$ (Ref R92).

sublattice making a 120° angle with each other, and *(0, 0, ½)* meaning that the sign of J will alternate from one plane to the next.

To further investigate the magnetically ordered state, low temperature neutron diffraction data were collected for all of the three compounds. All of the compounds exhibit additional superlattice reflections that disappeared above their respective T_c's, suggesting that these additional peaks are magnetic in nature. Analysis of these data will be discussed below for each phase separately.

1- The Magnetic Structure of $NiAs_2O_6$:

Neutron diffraction data were collected at 10, 20, 25, 28, 30, 35 and 40 K in the 2θ range 6°- 35°. The results can be summarized by considering the data at five temperatures as shown in Fig(5.13) in which two superlattice refections at 2θ angles of 8.88° and at 21.48° can observed that gradually decease in intensity until they disappear at about 30 K indicating that they are magnetic in origin. These magnetic peaks can be indexed on a magnetic cell of a_c and $2c_c$ (a_c *and* c_c are the chemical cell constants), *i.e.* a magnetic propagation vector **k** = *(00½)*, so that these peaks can be indexed as (00½) and (003/2) on the chemical cell or as (001) and (003) on the magnetic cell.

The 10 K data were analyzed with the Rietveld profile refinement program **Rietan** written by Izumi (I89). This program is capable of modelling neutron scattering from magnetic structures with collinear spin arrangements. The magnetic moment of each magnetic site and the angle between the spin direction and the unique axis of the lattice, ϕ, can be refined using the equations given by Shirane (S59). The magnetic form factor for the Ni^{2+} was obtained from ref (W61). The refinement was carried out in the space group *P-31m* but with $c_m = 2c_c$, and the two Ni sites were allowed to have different orientations. Fig(5.14) shows a good fit of this model to the observed data with R_{wp} = 6.08, R_p = 4.50 and R_{exp} = 4.10. The details of the Rietveld refinement are tabulated in Table(5.6). The atomic positions and the cell parameters were fixed during the

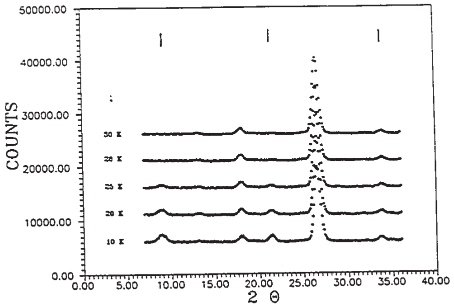

Fig(5.13) Low temperature neutron scattering data for $NiAs_2O_6$ collected at various temperatures. The magnetic peaks are indicated by bars.

refinement. The scale, background, full width at half maximum parameters (*U, V, W*), an overall temperature factor, asymmetry parameter, preferred orientation, and the magnetic moment and the angle ϕ, were refined. The magnetic moment of Ni^{2+} obtained was 2.11(3) μ_B which compares well with the magnetic moments reported in the literature such as the magnetic moment of Ni^{2+} in $KNiF_3$ with μ = 2.2 μ_B (S61) and in K_2NiF_4 with μ = 1.9 μ_B (B70). The angle ϕ was refined to 61(6)°, the large standard deviation in the angle ϕ would make it not very reliable. Fixing the angle at 90° would give a worse R factors, R_{wp} = 8.2.

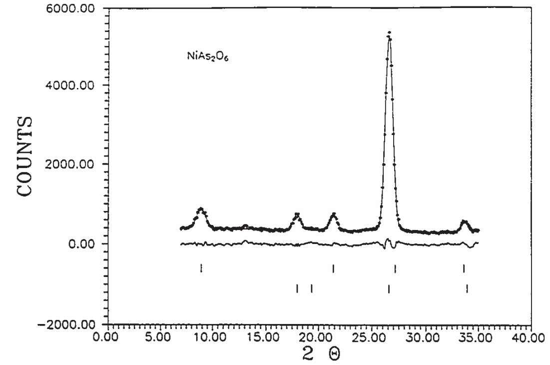

Fig(5.14) The Rietveld refinement fit of the magnetic scattering data for $NiAs_2O_6$. The upper set of bars indicates the magnetic Bragg peaks and the lower set corresponds to the nuclear Bragg peaks.

Based on the above model of the magnetic structure, the spin arrangements in this compound can be described as consists of an alternating sequence of ferromagnetic (001) layers resulting from in-plane interactions that are ferromagnetic and antiferromagnetic inter-plane couplings as can be depicted in Fig(5.15).

In principle, this compound can undergo a metamagnetic behavior, *i.e.* a field-induced transition from the antiferromagnetic state directly to the saturated paramagnetic phase. To check the possibility of the presence of this transition, magnetic susceptibility was measured as a function of temperature at various magnetic fields. These results are

Table 5.6
Rietveld Refinement of 9 K Neutron
Diffraction Data for $NiAs_2O_6$

space group			P-31m	
Z			2	
a(Å)			4.7474	
c(Å)			8.8395	
Temperature (K)			9.00(1)	
2θ range (°)			6 - 35	
overall B ($Å^2$)			0.24	
μ (μ_B)			2.11(3)	
ϕ (°)			61(6)	
Atom	Site	x	y	z
Ni1	1a	0.0	0.0	0.0
Ni2	1b	0.0	0.0	1/2
As	4h	1/3	2/3	1/4
O1	6k	0.3595	0.0	0.1361
O2	6k	0.3595	0.0	0.6368
R_{wp}			6.07%	
R_p			4.50%	
R_{exp}			4.23%	
No. of data points			281	
No. reflections			8	
No. of parameters refined			15	

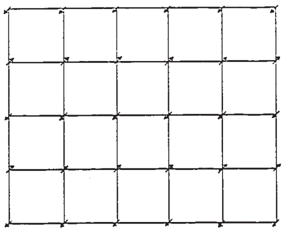

Fig(5.15) The magnetic spin arrangements in $NiAs_2O_6$ as can be seen in the (100) projection.

summarized in Fig(5.16) in which the antiferromagnetic transition persists even at 5 Tesla which rules out the presence of the metamagnetic transition. This is not surprising knowing that the inter-planar antiferromagnetic coupling is anticipated to be much larger than the intra-planar ferromagnetic correlations.

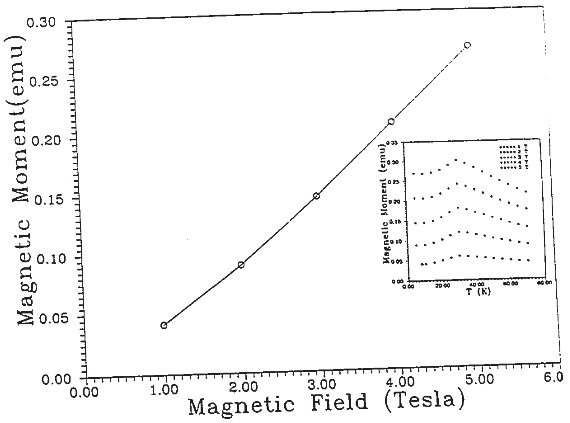

Fig(5.16) Variation of the magnetic moment as a function of field for $NiAs_2O_6$. Inset graph contains the magnetic moment versus temperature at various magnetic fields.

__The Magnetic structure of $CoAs_2O_6$:__

Similar measurements at low temperatures as those performed on the $NiAs_2O_6$ were done on this sample. Low temperature neutron diffraction data were collected at temperatures 9, 12, 17, 18, 19, and 19.5 K. A number of superlattice reflections were observed at the 2θ angles of 8.75°, 21.27°, and 35.10° which they disappeared above

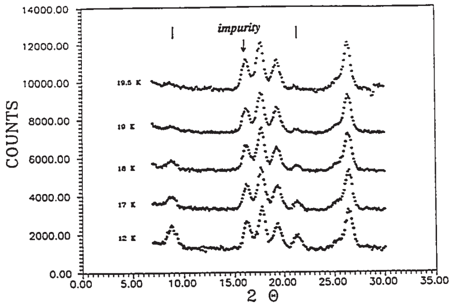

Fig(5.17) Low temperature neutron scattering data for $CoAs_2O_6$ at various temperatures.

about 20 K. This temperature corresponds to the ordering temperature as indicated in the magnetic susceptibility data, suggesting that these superlattice reflections are magnetic in origin. The results of the neutron diffraction data are summarized in Fig(5.17) in which the intensity of the superlattice reflections decreases as the temperature is increased and finally vanishes at about 19.5 K. The intensity of these reflections is larger than that of $NiAs_2O_6$ because of the larger moment of Co^{2+}, d^7. As in the case of $NiAs_2O_6$, these superlattice reflections can be represented by a propagation vector **k** = *(00½)* and were indexed on a magnetic cell of a_c and $2c_c$ (*a_c and c_c* are the chemical cell constants). Likewise, the Miller indices of these magnetic reflections are (001), (003), and (111), respectively.

The 10 K data were analyzed with the Rietveld profile refinement method using the **Rietan** program. The magnetic form factor for the Co^{2+} was obtained from ref (W61). The refinement was carried out in the space group *P-31m* with $c_m = 2c_c$ while *a* and *b* are identical to the chemical cell. The atomic positions and the cell parameters were fixed during the refinement. The magnetic moment of each magnetic site and the angle between the spin direction and the unique axis of the lattice, ϕ, were refined. A reasonable fit was obtained with the R-factors R_{wp} = 7.86, R_p = 5.85, and R_{exp} = 4.13. The profile pattern of the fit is plotted in Fig(5.18). The refined magnetic moment of Co^{2+} ion was 2.66(30) μ_B which is somewhat smaller that the other magnetic moments of Co^{2+} found in the literature, for example, $RbCoF_3$ with μ of 3.0 μ_B (A71) and CoO with μ of 3.5 μ_B (K70). The angle between the spin direction and the *c*-axis, ϕ, is 66(16)°. The standard deviation of ϕ in this case is even larger than that in the $NiAs_2O_6$. Although such a large standard deviation would make this value unreliable, the quality of the fit improved by refining this parameter. If the refinement was carried out and the parameter ϕ was fixed at 90°, the R_{wp} would be as high as 9.30. The details of the Rietveld refinement are tabulated in Table(5.6).

Since the intensity of the magnetic scattering at zero field is proportional to the square of the spontaneous magnetization, the temperature dependence of the intensity of the magnetic peaks yields the behavior of the magnetization and thus the critical exponent β. It was possible to estimate the critical exponent β and the critical temperature T_c by using the intensity of the magnetic reflection (001) obtained from the neutron diffraction data between 9 K and 19.5 K. The values for T_c and β were determined from a least squares refinement of the relationship

Table 5.7
Rietveld Refinement of 9 K Neutron
Diffraction Data for $CoAs_2O_6$

space group	P-31m
Z	2
a(Å)	4.7534
c(Å)	8.9620
overall B (Å²)	0.25
μ (μ_B)	2.66(3)
ϕ (°)	66(16)

Atom	Site	x	y	z
Co1	1a	0.0	0.0	0.0
Co2	1b	0.0	0.0	1/2
As	4h	1/3	2/3	1/4
O1	6k	0.3626	0.0	0.1373
O2	6k	0.3626	0.0	0.6373

R_{wp}	7.86%
R_p	5.85%
R_{exp}	4.13%
No. of data points	478
No. reflections	27
No. of parameters refined	15

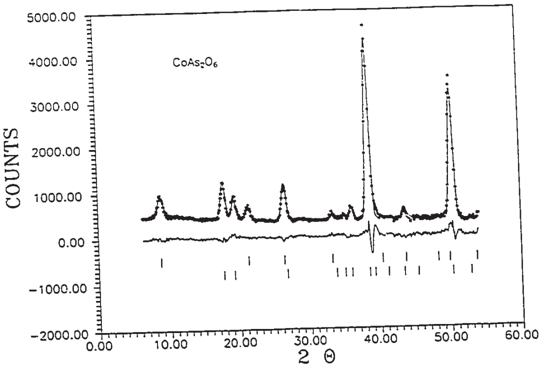

Fig(5.18) The Rietveld refinement fit of the magnetic scattering data for $CoAs_2O_6$. The upper set of bars indicates the magnetic Bragg peaks and the lower set corresponds to the nuclear Bragg peaks.

$$M \propto \left(\frac{T - T_c}{T_c}\right)^{\beta} \qquad (5.3)$$

where M is the spontaneous magnetization and β is the magnetization critical exponent. A log-log plot, Fig(5.19), of the spontaneous magnetization versus reduced temperature, t, gives $T_c = 19.1(2)$ and $\beta = 0.27(5)$. The value of β is closest to that of the 3-D Ising system which would have a β value of 0.3125 (F77).

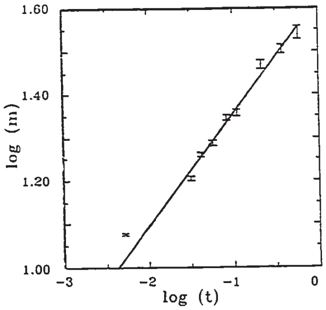

Fig(5.19) *log-log plot of the magnetization of the magnetic reflection (001) versus the reduced temperature for* $CoAs_2O_6$.

Similar measurements were collected from this compound where the magnetic susceptibility was measured as a function of the magnetic field. As in $NiAs_2O_6$, the metamagnetic transition was not present as illustrated in Fig(5.20). The long range order transition presisted at magnetic fields upto 5.0 T.

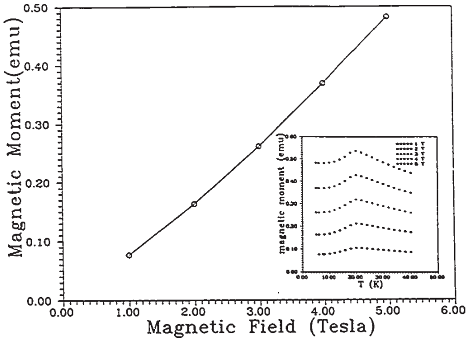

Fig(5.20) *Variation of the magnetic moment as a function of field for* $CoAs_2O_6$. *Inset graph contains the magnetic moment versus temperature at various magnetic fields.*

3- Magnetic Scattering of $MnAs_2O_6$*:*

Low temperature neutron diffraction data for this material were collected on the Dualspec diffractometer with a high flux of neutrons with a wavelength of 1.4999 Å. The resolution of this diffractometer is much higher than that of the PSD diffractometer which was used to collect data on both of the other materials. A difference plot of the 5 K and the room temperature data is shown in Fig(5.21) in which a number of superlattice reflections were observed that disappeared at about 12 K.

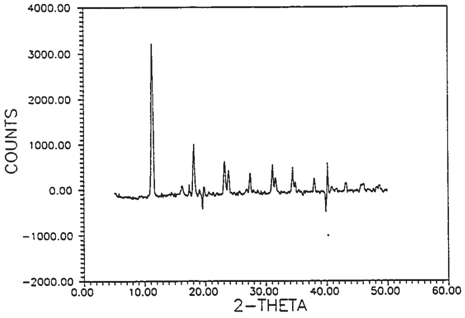

Fig(5.21) *The difference plot of the 5 K neutron scattering data set and 15 K data set for* $MnAs_2O_6$.

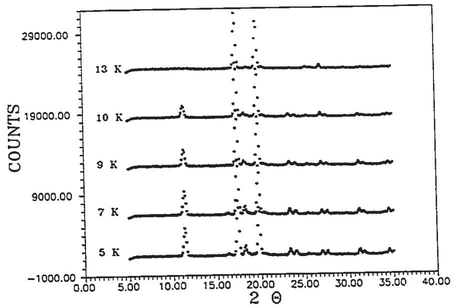

Fig(5.22) *The variation of the intensity of the magnetic as a function of temperature for* $MnAs_2O_6$.

The vanishing of these superlattice reflections is clearly shown in Fig(5.22) in which the intensity of the magnetic peaks was traced as the temperature was increased. It was obvious that these superlattice reflections can not be indexed by the simple **k** vector *(00½)*. An exhaustive list of various superlattices were used to index these reflections but without success. Superlattices such as (2a,2a,2c), (2a,a,2c), (3a,3a,2c), (3a,3a,c), (√3a,√3a,2c), (2√3a,2√3a,2c). Nevertheless, we were able to index the high angle portion of the pattern in the cell (4a, 2b, 4c). The magnetic structure could be represented more easily in terms of an incommensurate unit cell. We are attempting in the mean time to index the superlattice reflections in an incommensurate unit cell.

Incommensurate magnetic order was predicted by the mean field theory only if further in-plane interactions were included as illustrated in Fig(5.23). Regions of incommensurate order are denoted by *(q,q)* which indicate the direction (110) in q-space of the ordering wavevector. An incommensurate magnetic order was reported for $RbMnBr_3$ (G73) which have a magnetic lattice with ...AAA... stacking.

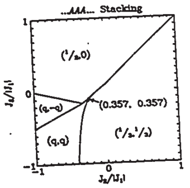

Fig(5.23) MFT predictions for incommensurate magnetic order in triangular lattice.

Chapter 6

Iron Arsenate

I- Introduction:

In the course of the preparation of other members of the transition metal arsenates with the lead antimonate structure, the preparation of iron arsenate, $FeAs_2O_6$, was attempted. This was thought to be possible because the ionic radius ratio of Fe^{2+}/As^{5+} falls within the limits of the field of stability of the lead antimonate structure.

As was described in chapter 3, reaction (3.6) yielded a white product which has a powder diffraction pattern that is strikingly different from that observed for the AAs_2O_6 arsenates. As can be seen in Fig(6.1), the diffraction pattern of this product resembles to a large extent the pattern of an iron arsenate phase with the composition $Fe_2As_4O_{12}$. This was found to be the correct composition after further analysis of the X-ray diffraction data obtained from the Guinier camera.

Although the nominal chemical formula of this compound can be written as $FeAs_2O_6$, it could be more precisely rewritten as $Fe^{3+}{}_2[As^{3+}(As^{5+}O_4)_3]$ where Fe is in the trivalent state and As is in oxidation states +3 and +5. Thus it seems that Fe^{2+} and As^{5+} are thermodynamically incompatible with oxide material of this structure type. This argument is supported by the fact that all of the iron arsenates reported in the JCPDS data base were found to contain iron in the trivalent state only.

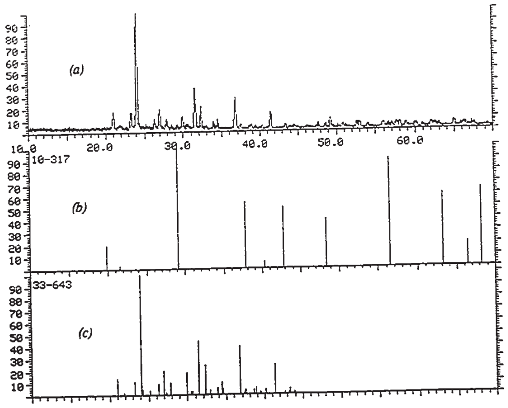

Fig(6.1) Powder X-ray diffraction for $Fe_2As_4O_{12}$: (a) observed intensity data for the product of reaction (3.6) ; (b) diffraction pattern for $CoAs_2O_6$; (c) diffraction pattern for $Fe_2As_4O_{12}$. (b) and (c) were obtained from JPDS cards.

$Fe_2As_4O_{12}$ crystallizes in a hexagonal space group $P6_3$ and the unit cell dimensions were $a = 14.743(7)$, and $c = 7.638(1)$, with Z = 6, which are in good agreement with those reported by d'Yvoire (Y74).

d'Yvoire *et al* (Y79) solved the crystal structure of this compound using the single crystal X-ray diffraction.

Therefore, our objective in the present study was primarily to study the magnetic properties of this compound and ultimately to correlate, if possible, our findings with the crystal structure. A thorough investigation of the magnetically ordered state will be attempted by the use of low temperature neutron diffraction.

Before pursuing the discussion of the magnetic properties, it is essential to describe in some detail the crystal structure of this material and carefully examine the structural features which would be expected to influence the magnetic behavior of this compound. $Fe_2As_4O_{12}$ has a very complicated and remarkable 3-dimensional framework as illustrated by the basal plane projection in Fig(6.2) and in Fig(6.3). In the (001) projection, As^{3+} is coordinated to three oxygen atoms forming a central pyramid $As^{3+}O_3$ which is bonded to three tetrahedral groups $As^{5+}O_4$ via the O atoms.

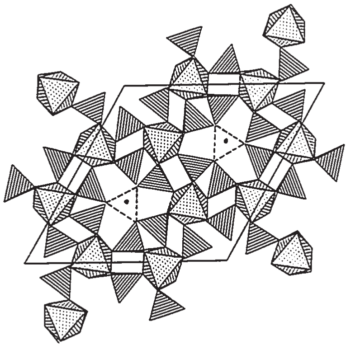

Fig(6.2) (001) projection of $Fe_2As_4O_{12}$.

The most interesting feature of this structure is a discrete face-sharing Fe_2O_9 dimers which can better be viewed in Fig(6.3). The Fe ion is in octahedral coordination, the Fe-O inside the octahedron has an average distance of 2.012 Å. The Fe-O-Fe angles are very close to 90°, and the Fe–Fe separation is about 3.03 Å. This structure, therefore, presents the possibility of both dimer-confined and three dimensional magnetic exchange interactions.

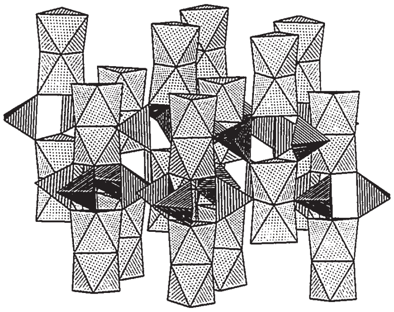

Fig(6.3) The structural framework of $Fe_2As_4O_{12}$.

II- Magnetic Susceptibility:

The magnetic susceptibility was measured on a polycrystalline sample in the temperature range of 5-300K. The susceptibility attains a maximum of 7.65 × 10^{-2} emu/mol at approximately 50 K below which a sharp decrease was observed suggesting a transition to a long range order as can be seen in Fig(6.4a).

The data in the range 80 - 300 K can be fitted to a Curie-Weiss law, with an effective magnetic moment of 5.75 μ_B and the Weiss constant was equal to -94.9 K. A plot of the inverse susceptibility data and the predictions of the Curie-Weiss law is shown in Fig(6.4b). Remarkably, there is no noticeable deviation from the Curie-Weiss law which would be expected if significant short range correlations were to be expected.

It was expected that the magnetic susceptibility would be dominated by the antiferromagnetic exchange within the Fe_2O_9 dimer units. Hence we attempted to fit the magnetic susceptibility data in terms of a dimer model using equation (6.1) (O82).

$$\chi = C\,\frac{2e^{2x}+10\,e^{6x}+28\,e^{12x}+60\,e^{20x}+110\,e^{30x}}{1+3\,e^{2x}+5\,e^{6x}+7\,e^{12x}+9\,e^{20x}+11\,e^{30x}} \qquad (6.1)$$

where $C = Ng^2\mu^2_B/kT$, and $x = J/kT$.

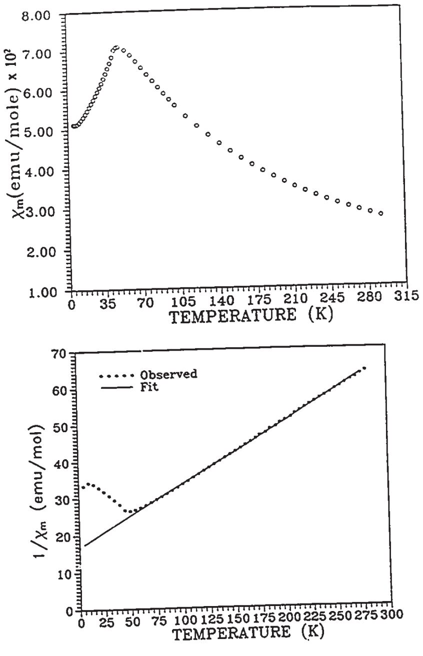

Fig(6.4) Magnetic susceptibility of $Fe_2As_4O_{12}$: (a) magnetic susceptibility versus temperature ; (b) the inverse of the magnetic susceptibility versus temperature. Circles represent the observed data and solid line denotes the prediction of the Curie-Weiss fit.

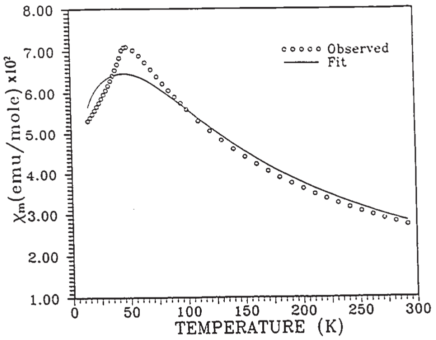

Fig(6.5) The fit of the magnetic susceptibility of $Fe_2As_4O_{12}$ to the predictions of the S = 5/2 - 5/2 dimer model.

Surprisingly enough, the fit was very inadequate as can be seen in Fig(6.5) which would indicate that the interdimer interactions were also appreciable in this material which lead to the onset of the long range order directly. This seems to be in line with the absence of any deviations in the Curie-Weiss fit in the lower portion of the data set.

The absence of any significant short range correlations in the susceptibility data is likely to be due to two reasons. Firstly, the angle Fe-O-Fe is sharply different from 180° which will cause the magnitude of the interaction constant to be very small, and thus will result in a weaker interdimer interaction.

The correlation between the exchange constant and the angle M-O-M has been observed in many systems. The classical example is the dihydroxy-bridged copper(II) dimers in which the exchange constant decreases as the Cu-O-Cu angle deviates from 180° until the bond angle reaches 97.6° after which the ferromagnetic coupling dominates over the antiferromagnetic coupling. In fact, there is a linear relationship between J and θ in a series of dihydroxy-bridged copper(II) dimers. Magnetism in oxo-bridged diiron dimers has been reviewed by Kutz (K90.2) and Holzelman *et al.* (H92.2). Contrary to the Cu-based dimers, there was a general lack of linear relationships between J values and structural parameters which was attributed to a relatively complex interplay of competing orbital pathways for spin coupling and a sensitivity to multiple structural variables *e.g.* bond length, bond angle and spin distribution. What is clear is that the antiferromagnetic coupling diminishes as the Fe-O-Fe angle becomes more acute, for instance, the exchange constant in $[Fe(salen)(OH)]_2$ is 14.4 K (10 cm^{-1}) with Fe-O-Fe angle 102° (B84) and 144 K for $Fe(salen)_2O.py$ with Fe-O-Fe is about 160° (G68) (salen = N,N'-ethylenebis(salicylamide)). The spin coupling in high-spin d^5 Fe^{3+} dimers is almost invariably antiferromagnetic in nature. Those dimers included in the study have Fe-O-Fe angles vary between 180° and 110°. For more acute angles abnormal behavior has been reported for a number of dimers. It was reported by Mikuriya *et al.* (M91) that the coupling in an Fe^{3+} dimer, N-salicylidene-2-hydroxy-5-chlorobenzylamine, with an Fe-O-Fe angle of 92.5° is ferromagnetic. In the system at hand, it is most likely that the intra-dimer interaction is antiferromagnetic, but how strong is this exchange can not be determined based on the susceptibility data.

Another factor that comes into play is that other superexchange pathways become important. In addition, these interdimer interactions are larger in number with respect to the intradimer exchange interactions and hence their total contribution become significant.

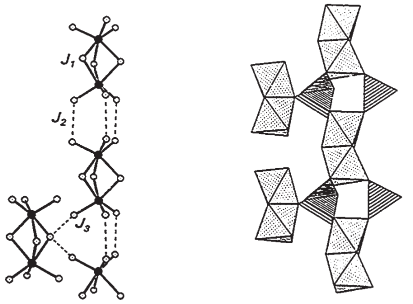

Fig(6.6) The possible exchange pathways in the $Fe_2As_4O_{12}$ structure.

The possible exchange pathways in this compound are listed in Table(6.1) and are illustrated pictorially in Fig(6.6) as well in which the Fe_2O_9 dimer is connected to two dimers along the <001> direction via three AsO_4 tetrahedra which would lead to a possible exchange pathway which is mediated by two oxygen atoms Fe-O-O-Fe. Likewise, the same Fe_2O_9 dimer is connected to another three dimers in the basal plane.

Table 6.1
Description of the various exchange pathways in $Fe_2As_4O_{12}$

Pathway	Distance/ bond angle		Exchange type
J_1	3.84 Å	90°	direct/superexchange
J_2	6.65 Å	120°	superexchange
J_3	6.65 Å	124° Fe1	superexchange
	6.70 Å	112° Fe2	

III- Long Range Order:

The sharp decrease in the magnetic susceptibility data below 50 K suggested the presence of a magnetic long range order in this system. To investigate this further low temperature neutron scattering data were collected on the powder sample at various temperatures. The scattering pattern of $Fe_2As_4O_{12}$ at 9 K contains a number of very intense superlattice reflections.

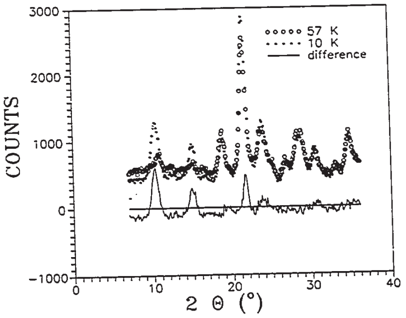

Fig(6.7) The difference plot of the neutron diffraction profiles of 10 K and 57 K of $Fe_2As_4O_{12}$. Magnetic reflections can be clearly seen.

These reflections could be more clearly identified in the difference plot as in Fig(6.7) in which the most intense of the superlattice reflections have 2θ values of 10.30°, 15.02°, and 21.5°. Fig(6.8) summarizes the intensity of the superlattice reflections as a function of the temperature where the intensity of these reflections decreases rapidly as the temperature is increased to about 50 K which would indicate that these superlattice reflections are magnetic in origin. These superlattice reflections were indexed on the same chemical cell leading to a propagation vector of *k=(0,0,0)*.

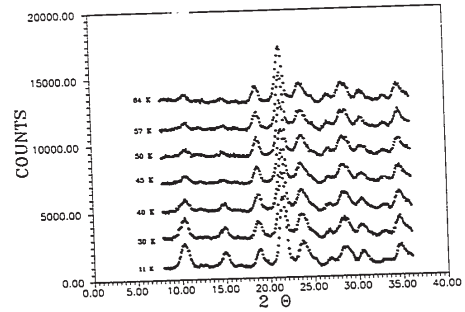

Fig(6.8) *The variation of the intensity of the magnetic superlattice reflections for* $Fe_2As_4O_{12}$ *as a function of temperature.*

In solving for the magnetic structure in this material, the initial fitting of the intensity data was attempted on the simple model of spin up spin down in the dimer while keeping the multiplicity of each site at six as in the chemical space group. This model was found not to be adequate in representing the observed intensity data. The refinement was then carried out using the space group *P3*, a subgroup of the *$P6_3$*. In this space group each Fe site was split into two different sites. The refinement in this space group resulted in an excellent fit to the intensity data with reasonable fit indices, R_{wp} = 8.12, R_p = 6.51, and R_{exp} = 3.28. The refined magnetic moment was 5.1(4) μ_B which is larger that the theoretical moment of 5.0 μ_B but the error is also large. It should be noted that the atomic positions of all the atoms were kept constant and that an overall temperature factor was refined. This is done because of the large number of the atoms in the asymmetric unit cell which they total to 108 atoms. The results of the Rietveld refinement are plotted in Fig(6.9).

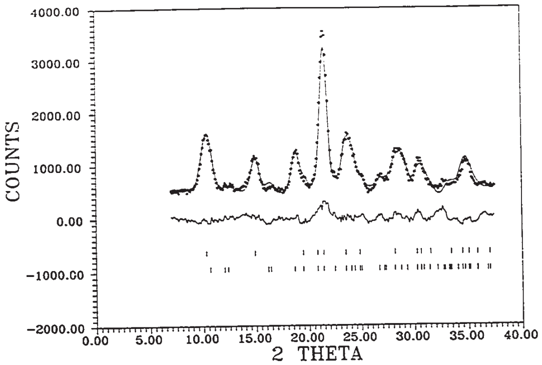

Fig(6.9) *The Rietveld refinement pattern of the low temperature neutron diffraction data for* $Fe_2As_4O_{12}$. *The upper set of bars indicates the magnetic Bragg peaks and the lower set corresponds to the nuclear Bragg peaks.*

The magnetic structure of this material is best represented as in Fig(6.10) which show the main interactions between the moments where it is clear that the nearest and next-nearest interactions are antiferromagnetic as was inferred from the susceptibility data.

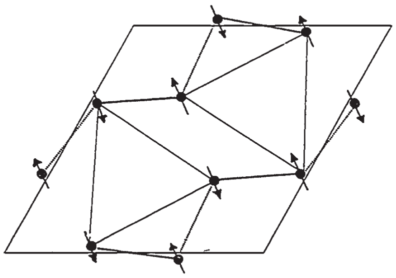

Fig(6.10) *Spin arrangement in the magnetic sublattice for* $Fe_2As_4O_{12}$. *Each spin represents a dimer in which both spins couple antiferromagnetically.*

Chapter 7

Conclusion

In this thesis, the structural and magnetic properties of oxides of the general formula AB_2O_6 where A is Mn, Fe, Co, Ni, Cu, and B is Sb or As, were investigated.

$CuSb_2O_6$ adopts a monoclinically distorted trirutile structure. It crystallizes in the space group $P2_1/n$. Atomic positions were determined by profile refinement of neutron powder diffraction data in the unit cell, $a = 4.6349(1)$, $b = 4.6360(1)$, $c = 9.2931(1)$, $\beta = 91.124(2)$. Magnetic susceptibility data exhibit a broad maximum at about 60 K and an abrupt transition at 8.5 K. The high temperature data can be fitted to a Curie-Weiss law giving $\mu_{eff} = 1.758$ and $\Theta = -48$ K. Although the crystal structure indicates a nearly square planar Cu^{2+} lattice as in other rutiles, a Cu-O-O-Cu superexchange pathway seems to be dominant, giving rise to short range correlations which are approximately one dimensional. The high temperature susceptibility is explained well by the 1-d Heisenberg model with $J/k = -46.94$ K. Analysis by Oguchi's method gives a ratio of interchain coupling to intrachain coupling constants of about 2×10^{-3} which compares well with other one dimensional Heisenber systems.

When compared with other trirutile phases, $CuSb_2O_6$ stood out in two categories, largest $T(\chi_{max})/T_c$ ratio of 7.1 and largest dominant in-plane exchange constant J/k. The former could be regarded as an indicator for the importance of the short range versus long range correlations. Of all the known trirutile phases, $CuSb_2O_6$ shows the clearest evidence for the dominance of 1-d correlations.

Low temperature neutron data confirmed the presence of the long range order. A superlattice refection was indexed with the wavevector $k = (½,0,½)$. This is identical to that of $CoSb_2O_6$. The extremely weak intensity of the magnetic reflection prevented the analysis of the neutron data with the Rietveld refinement using the **Rietan** program. Instead the magnetic moment was obtained by simulating the diffraction pattern while varying the magnetic moment of Cu^{2+}. An estimate of the moment was found to be 0.5 μ_B.

Another class of AB_2O_6 oxides was investigated, namely, the transition metal arsenates. Research on these oxides has been very scanty as of now. Very little has been known about their crystal structures and nothing has been reported on their magnetic properties. In the course of our study, the crystal structures of $NiAs_2O_6$, $CoAs_2O_6$, and $MnAs_2O_6$ were refined in space group *P-31m* by the Rietveld refinement analysis of neutron powder diffraction data that were obtained from PSD diffractometer in MNR. It was found that the crystal structure of these compounds can better be described in the space group *P-31m* than in the space group *P312* which was assigned by Magneli (M41).

It would be very preferable to refine these structures using single crystal X-ray

diffraction data since the R-factors obtained from the polycrystalline refinements are somewhat large, though reasonable. One must add that the standard deviations of the atomic positions and the bond angles and distances are very reasonable.

In a sharp contrast to the trirutile phases, the magnetic susceptibility data of these compounds were typical to that of a simple antiferromagnet.

The high temperature data were fitted to Curie-Weiss law. For the $NiAs_2O_6$, the effective magnetic moment was calculated to be 3.27(7) μ_B and Θ was -66.2(8) K. In the case of $CoAs_2O_6$, the effective moment was -4.98(6) and Θ was -64.4(4) K, while the magnetic moment was 5.90 μ_B and Θ was -20.7(1) for $MnAs_2O_6$.

The magnetic long range order was further investigated by low temperature neutron diffraction. The transition temperatures observed in the magnetic susceptibility were confirmed by low temperature neutron diffraction.

The superlattice reflections in the $NiAs_2O_6$ and $CoAs_2O_6$ were indexed in a hexagonal cell with the axes *a* and *b* being identical to the chemical cell and the *c* axis double that of the chemical cell. The wavevector would be $k = (00½)$. The magnetically ordered state in these oxides consists of alternating ferromagnetic (001) layers resulting from ferromagnetic in-plane interactions and antiferromagnetic inter-plane coupling. Low temperature neutron data were analyzed by the Rietveld refinement method using the **Rietan** program. It was found that the magnetic moment for Ni^{2+} was 2.11(3) μ_B and the angle ϕ was found to be 61(6)°. In the refinement of $CoAs_2O_6$, the magnetic moment was found to be 2.66(30) and the angle ϕ was 66(16)°.

Neutron diffraction data for $MnAs_2O_6$ were collected on the high resolution Dualspec diffractometer at a wavelength of 1.4999Å. The diffraction pattern did not fit the expected pattern with the wavevector $k = (00½)$. An exhaustive list of other wavevectors were not adequate to index all of the magnetic peaks. Further analysis is needed to index these peaks. The magnetic structure could well be handled as an incommensurate superstructure.

We did not succeed in preparing $FeAs_2O_6$ where Fe is in the divalent state. Instead, an iron arsenate phase of the composition $Fe_2As_4O_{12}$ was obtained the crystal structure of which was solved by d'Yvoire (Y79) using single crystal diffraction. Our investigation centered on the study of the magnetic properties and the possible correlation between the structure and magnetic properties. The main feature of the structure was the presence of discrete face-shared dimers. Remarkably, the magnetic susceptibility was not dominated by the dimer interactions. Attempts to fit the susceptibility data to an $S = 5/2$ dimer model were not successful. It appears that the long range order is more important and dominates the susceptibility.

The long range order was further studied by neutron diffraction. A number of intense superlattice reflections were observed and indexed with a wavevector $k = (000)$, *i.e.* the magnetic and nuclear cells are identical. The magnetic structure was found to consist of antiferromagnetic ordering between the dimer atoms. The multiplicity of each site was reduced to 3 instead of 6 and the space group of the magnetic lattice is *P3* instead of the nuclear crystal lattice of *P6/m*.

In summary, the magnetic and structural properties are highly correlated. This study illustrates this aspect rather clearly. Both classes of compounds have different crystal structures with various features to which the magnetic behavior is very sensitive. Furthermore, a clear contrast was observed even among the same class of compounds as in $CuSb_2O_6$ which seemed to exhibit different magnetic behavior from the other trirutile compounds in the short range order regime, and in $MnAs_2O_6$ which adopts a different ordered state from the other two arsenates.

REFERENCES

A50 Anderson P., *Phys Rev*, **79**, (1950)350

A51 Abragam A., Pryce M., *Proc. R. Soc.*, **A 205**, (1951)135.

A63 Anderson P., *in Magnetism vol. I*, eds Rado G, Suhl W, Academic Press, NY, 1963, Chap. 2.

A71 Allain Y., *J. Phys*, **32**, (1971)C611.

A82 Albitani A., Willis B., *J. Appl. Crystallog*, **15**, (1982)361.

B41 Bystrom A., Hok B., and Mason B., *Ark. Kemi. Mineral Geol.*, **150**, (1941)1.

B57-1 Belov N., Neronova N., Smirnova T., *Sov. Phys - Crystallog*, **2**, (1957)311.

B57-2 Billy C., Haendler H., *J. Amer. Chem Soc*, **79**, (1957)1049.

B64 Bonner J., Fisher M., *Phys Rev*, **133**, (1964)768.

B66 Bacon G., *X-ray and Neutron Diffraction*, p.71, Pergamon Press, 1966.

B68 Bertaut E., *Acta Crystallog.*, **A24**, (1968)217.

B70 Brigeneau R., Guggenham H, Shirane G., *Phys Rev*, **B1**, (1970)2211.

B75 Bacon G., *Neutron Diffraction*, 3rd Ed., Oxford Press (Clarendon), London 1975.

B79 Blote H., *J. Appl. Phys*, **50**, (1979)1825.

B80 Borovik-Romanov A., Kreines N., Laiho R., Levola T., Zhotikov V., *J. Phys. C*, **13**, (1980)9.

B84 Borer L., Thalken L., Ceccarelli C., Glick M., Zhang H., Reiff W., *Inorg. Chem.*, **23**, (1984)3398.

B90 Bencini A., Gatteschi D., *EPR of Exchange Coupled Systems*, Springer-Verlag, p.1, 1990.

C58 Caglioti G., Paoletti A., Ricci F., *Nucl. Instrum. Methods*, **35**, (1958)223.

C72 Cox D., *IEEE Transactions on Magnetics*, **May 8**,(1972)161.

C77.1 Carlin R., *Magnetic Properties of Transition Metal Compounds*, Springer-Verlag 1977.

C77.2 Cheetam A., Taylor K., *J. Sol. State Chem.*, **21**, (1977)253.

C78 Coppens P., *in Neutron Diffraction* ed Dachs H., Springlar-Verglar, p.72, 1978.

C85 Carlin R., in *Magneto-structural Correlations in Exchange Coupled systems* eds Willett R.,*et al.*, p.127, D.Reidel Publishing Company, 1985.

C86 Carlin R., *Magnetochemistry*, Springlar-Verglar, 1986.

C92 Cox P., *Transition Metal Oxides*, Clarendon Press, 1992.

C93 Coronado E., Drillon M., Georges R., in *Research Frontiers in Magnetochemistry*, ed O'Connor, p.27, World Scientific, 1993.

D58 Donnay G., Donnay J., Elliott N., Hastings J., *J. Phys. Rev*, **112**, (1958)1917.

D75 Donaldson J., Kjekshus A., Nicholson D., Rakke T., *Acta Chem Scand ser A*, **29**, (1975)803.

E68 Earnshaw A., *Introduction to Magnetism*, Academic Press, 1968.

E80 Engelfriet D., Groeneveld W., *Z. Naturforsh*(C86.p.183)

E84 Eicher S., *Ph.D. dissertation*, McMaster University, 1984.

E86 Eicher S., Greedan J., Lushington K., *J. Sol. State Chem*, **62**, (1986)220.

F62 Fisher M., *Phil. Mag.*, **17**, (1962)1731.

F63 Fisher M., *J. Math. Phys.*, **4**, (1963)124.

F66 Figgis, *Introduction to Ligand Fields*, Wiley N.Y.,(1966).

F77 Fava F., Danot M., Dinh N., Daoudi A., LeFlem G., *Solid State Commun.*, **22**, 1977(733).

G55 Goodenough J., *Phys Rev*, **100**, (1955)564.

G58 Goodenough J., *J. Phys Chem Solids*, **6**, (1958)287.

G68 Gerloch M., Lewis J., Mabbs F., Richards A., *J. Chem. Soc. A*, (1968)112.

G73 Glinka C., Minkiewicz V., Cox D., Kjatak C., *Magnetism and Magnetic Materials* (**AIP Conf. Proc. No. 10**), Part 1, ed. Graham C. Jr., Rhyne J., NY, p.659, 1972.

G90 *Introduction to Neutron Diffraction Facilities at Canadian Research Reactors*, eds B. Gaulin and B. Powell, p.10, 1990.

G92 Greedan J., *Landolt-Börnstein New Series III/27g*, p.87. 1992.

H74 Hone D., Richards P., *Ann Rev. Material Sci*, **4**, (1974)337.

H81 Hall J., *Ph.D Dissertation*, University of N. Carolina at Chapel Hill (1977), Hatfield W., *J. Applied Phys*, **52**, (1981)1985.

H85 Hatfield W., *in Magneto-structural Correlations in Exchange Coupled Systems*, eds Willett R. *et al.*, D.Reidel Publishing Company, 1985.

H87 Hill R., *J. Sol. State Chem.*, **71**, (1987)12.

H92.1 Hirakawwa H., Ikeda H., *in Magnetic Properties of Layered Transition Metal Compounds* ed. de Jongh L., p.231, Kluwer Academic Publishers, 1992.

H92.2 Hotzelmann R., Wieghardt K., Florke U., Haupt H., Weatherburn D., Bonvoisin J., Blondin G., Girerd J., *J. Amr. Chem. Soc.*, **114**, (1992)1681.

H93 Hatfield W., *in Research Frontiers in Magnetochemistry* ed. O'Conner, p.1, World Scientific, 1993.

I89 Izumi F., *Rietan-Rietveld Analysis Systems*, National Institute for Research in Inorganic Materials, Ibaraki. *Nippon Kessho Gakkai Shi*, **27**, (1985)23.

J66 Jesson J., *J. Chem Phys.*, 45, (1966)1049.

J74 de Jongh L., Miedema, *Adv. Phys.*, **23**, (1974)1.

J81 de Jongh L., *in Recent Developments in Condensed Matter Physics*, eds Devreese J., p. 343, Plenum Press, 1981.

J85 de Jongh L., *in Magneto-structural Correlations in Exchange Coupled Systems*, ed Willett R. *et. al.*, p.1, D.Reidel Publishing Company, 1985.

J92 de Jongh L., *in Magnetic Properties of Layered Transition Metal Compounds* ed. de Jongh L., p.1, Kluwer Academic Publishers, 1992.

K34 Kramers H., *Physica*, **1**, (1934)182.

K59 Kanamori, *J. Phys Chem Solids*, **10**, (1959)87.

K66 Keffer F., *Encyclopedia of Physics*, **XVIII/2**, (1966)1.

K67 Kasper H., *Mh. Chem.*, **98**, (1967)2107.

K70 Khan D., Erickson R., *Phys Rev*, **B1**, (1970)2243.

K88.1 Kramers R., Greedan J., *J. Solid State Chem.*, **73**, (1988)579.

K88.2 Kramers R., Greedan J., Gmelin E., Dai W., White M., Eicher S, Lushington K., *J. Phys (Paris) Colloq.*, **49**, Supplement C-8,(1988)1495.

K90.1 Koch R., *Sol. State Tech*, May, (1990)255.

K90.2 Kurtz D. Jr., *Chem Rev.*, **90**, (1990)585.

L62 Legrand E., Plumier R., *Phys State Sol*, **2**, (1962)317.

L70 Lines M., *J. Phys Chem Solids*, **31**, (1970)101.

M41 Magneli A., *Arkiv Kemi Mineral. Geol.*, **15B**, (1941)1.

M66 Mulay L., *Magnetic Susceptibility*, Interscience Publishers, 1966.

M68 Martin R., *in New Pathways in Inorganic Chemistry*, eds. Ebsworth E., Maddock A., Sharpe A., Cambridge University Press, New York, Chap.9, 1968.

M72 Mériel M., *Ann. Phys.*, **7**, (1972)255.

M73 Mabbs F., Machin D., *Magnetism and Transition Metal Complexes*, London, Chapman and Hall, 1973.

M78 Mitra S., *Progress in Inorganic Chemistry*, **22**, (1978)310.

M83 McEwan S., Faber J., Turner A., *Acta Metall*, **31**, (1983)657.

M91 Mikuriya M., Kakuta Y., Kawano K., Tokii T., *Chem Lett. (Japan)*, (1991)2031.

N00 NBS Report No. 9086, JCPDS - Card No. 17-284.

N32 Néel , *Ann. Phys*, **18**, (1932)5; *Compt. rend.*, **203**, (1963)304.

N90 Nakua A., Hun H., Greedan J., Riemers J., Stager C., *J. Sol. State Chem*, **91**, (1990)105.

O44 Onsager L., *Phys Rev*, **65**, (1944)117.

O64 Oguchi , *Phys Rev. A*, **133**, (1964)1098.

O82 O'Conner C., *Progress in Inorganic Chemistry*, ed. Lippard S., **29**, (1982)203.

O93 O'Conner C., *in Research Frontiers in Magnetochemistry*, ed O'Conner P., World Scientific, 1993

P86 Prices D., Sköld K., *in Methods of Experimental Physics Vol. 23- Part A*, eds. Sköld K. and Prices D., p.1, Academic Press, 1986.

P91 Prince , *Workshop on the Rietveld Method*, Chalk River, 1991.

R58 Rushbrooke G., Wood P., *Mol. Phys.*, **1**, (1958)257.

R63 Rushbrooke G., Wood P., *Mol. Phys.*, **6**, (1963)409.

R67 Rietveld H., *Acta Crystallog*, **22**, (1967)151.

R69 Rietveld H., *J. Appl. Crystallog*, **2**, (1969)65.

R79 Reinen D., Friebel C., *Structure and Bonding*, **37**, (1979)1.

R87 Rossat-Mignad J., *in Methods in Experimental Physics, Vol.23- Part C*, eds. Sköld K., Prices D., p.69, 1987, Academic Press.

R89.1 Reimers J., Greedan J., Stager C., Kremer R., *J. Sol. State Chem*, **83**, (1989)20.

R89.2 Reimers J., Greedan J., unpublished results.

R92.1 Regnault L., Rossat-Migrad, *in Magnetic Properties of Layered Transition Metal Compounds* ed de Jongh L., p. 271, Kluwer Academic Publishers.

R92.2 Reimers J., Dahn J., *J. Appl Conds Matter*, **4**, (1992)8105.

S59 Shirane G., *Acta Cryst.*, **12**, (1959)282.

S61 Scatturin V., Corliss L., Elliott N., and Hastings J., *Acta Crystallog.*, **14**, (1961)19.

S72 Scherm R., *Ann. Phys*, **7**, (1972)349.

S73 Samuelsen , *Phys Rev Lett*, **31**, (1973)936.

S76 Shannon P., *Acta Crystallog.*, **A32**, (1976)751.

S78 Squires G., *Thermal Neutron Scattering*, Cambridge University Press, London, 1978.

S82 Shimada S., MacKenzie K., *Thermochim Acta*, **56**, (1982)73.

S85 Shimada S., Kodaira K., Matsushita T., *J. Crys Growth*, **72**, (1985)753.

S91 Sakthivel A., Young R., *User's Guide to programs DBWS-9006 and DBWS-9006PC*, 1991.

T58 Taylor J, Hyding R., *Can. J. Chem*, **36**, (1958)597.

T84 Tomson C., Mildner D., Mehregany M., Sudol J., Berliner R., Yelon W., *J. Appl Cryst.*, **17**, (1984)385.

V77 Villain J., Loveluck J., *J. de Phys Lett*, **38**, (1977)L77.

W07 Weiss P., *J. Phys*, **6**, (1907)667.

W70 Woolfson M.; *An Introduction to X-ray Crystallography*, Cambridge Univeristy Press, 1970.

W72 Will G., *Ann Phys*, **7**, (1972)371.

W74 Witteveen H., Reedijk J., *J. Sol State Chem*, **10**, (1974)151.

W84 Wells A., *Structural Inorganic Chemistry*, 5th edition, Oxford Science Publications, p.905, 1984.

W92 Wildner M., *Z. Kristallog*, **202**, (1992)51.

Y74 d'Yvoire F., *Bull Soc. Chim Fr.*, (1974)1215.

Y79 d'Yvoire F., Huy Nguyen D., *Acta Crystallog*, **B35**, (1979)1751.

Y93 Young R., *The Rietveld Method*, ed. Young R., p.1, Oxford University Press, 1993.